

2019

PHYSICAL PROPERTIES OF NANOMATERIALS: WITH APPLICATIONS TO PENTAGONAL SYSTEMS

BRAVO CASTILLO, SERGIO JAVIER

<https://hdl.handle.net/11673/45775>

Repositorio Digital USM, UNIVERSIDAD TECNICA FEDERICO SANTA MARIA

Universidad Técnica Federico Santa María



Physical properties of nanomaterials: with applications to pentagonal systems

Sergio Bravo Castillo

December, 2018.

Tutor: PhD. Mónica Pacheco D.

Tutor: PhD. Leonor Chico G.

Outline

In this thesis we theoretically study a set of novel systems, known as *pentagonal materials*. Physical properties of interest such as electronic structure, optical response, electronic transport properties and the existence of topological phases are analyzed. We have employed well-established techniques as well as innovative approaches in order to get a detailed picture of all the mentioned features. The structure of the work is described next.

In Part I we present the theoretical concepts that are used throughout the entire thesis. Such topics are symmetry basics, with group theory generalities, first-principles methods, the tight-binding approximation, optical response in the tight-binding approximation, electronic transport in the ballistic regime and topological properties of materials. The exposition is brief, highlighting only the needed concepts for the subsequent parts.

Part II concerns with the electronic, optical and transport properties of penta-graphene (PG) and its nanostructures. We show how penta-graphene responds to an electromagnetic field perturbation analyzed within the tight-binding approach. We also compute features of the electronic structure of penta-graphene and its nanostructures by means of first-principles and tight-binding methods. We obtain good accordance between these two approaches in electronic and optical response. Also, a promising thermoelectric transport performance is found for a particular device configuration.

Part III includes the theoretical study and numerical calculation of symmetry-enforced and topological properties of pentagonal materials. We use several examples of PG-derived systems by doping or adsorption. This allows us to design different phases such as trivial metallic phases with nodal lines, Dirac nodes in presence of spin-orbit coupling and time-reversal symmetry breaking phases with a non-trivial Chern insulator character. Identification of additional phases like Weyl nodes, weak and crystalline topological phases is also feasible. Topological properties were studied by the calculation of topological invariants with the Wannier charge center evolution method and also by a recent theoretical framework called topological quantum chemistry.

Considering all the results obtained in this work, we can assert that pentagonal materials represent a promising family of low dimensional systems with many interesting physical properties that deserve to be studied in more detail in upcoming years.

Contents

| | |
|--------------------------------------------------------------------------|-----------|
| Contents | 4 |
| List of Figures | 6 |
| List of Tables | 8 |
| | |
| I Theoretical fundamentals | 9 |
| 1 Introduction | 10 |
| 2 Symmetry tools: group theory basics | 13 |
| 3 First-principles methods: Density Functional Theory | 18 |
| 4 Tight-binding method | 22 |
| 4.1 Slater-Koster parameterization | 23 |
| 5 Optical response in the tight-binding approximation | 26 |
| 6 Electronic transport | 29 |
| 6.1 Thermoelectric transport | 31 |
| 7 Topological phases | 33 |
| 7.1 Introduction | 33 |
| 7.2 General description of topological phases | 35 |
| 7.2.1 Topological insulators | 35 |
| 7.2.2 Topological (semi)-metals | 36 |
| 8 Theoretical tools to characterize a topological phase | 40 |
| 8.1 Topological Quantum Chemistry | 40 |
| 8.2 Other methods to classify topological phases | 46 |
| 8.2.1 Ten-fold way (K-theory) | 46 |
| 8.2.2 Band filling constraints and symmetry indicators | 49 |
| 8.3 Calculating topological invariants: Wannier charge centers | 50 |

| | |
|--------------------------------------------------------------------------|------------|
| II Electronic, optical and transport properties of penta-graphene | 52 |
| 9 Results | 53 |
| 9.1 Penta-graphene lattice geometry | 53 |
| 9.2 First-principles calculations | 55 |
| 9.3 Tight-binding model | 55 |
| 9.4 Electronic properties of PG | 57 |
| 9.5 Optical properties of monolayer PG | 58 |
| 9.6 Additional parameterizations | 59 |
| 9.7 Penta-graphene nanoribbons | 61 |
| 9.7.1 Band structure of PGNRs | 63 |
| 9.7.2 Optical absorption of PGNRs | 63 |
| 9.8 Thermoelectric properties of penta-graphene | 65 |
| | |
| III Topological properties of penta-materials | 70 |
| 10 Results | 71 |
| 10.1 Symmetry analysis | 71 |
| 10.2 Topological analysis | 75 |
| 10.3 Examples of penta-materials | 78 |
| 10.3.1 Symmetry-protected metallic phases | 79 |
| 10.3.2 Topological phase: breaking TRS | 83 |
| 11 Conclusions | 93 |
| | |
| IV Appendices | 95 |
| 12 Part II appendices | 96 |
| 12.1 Appendix: Tight-binding code description | 96 |
| 12.2 Appendix: Recursive Green's function method | 98 |
| 13 Part III appendices | 101 |
| 13.1 Appendix: Chern number and Berry phase | 101 |
| 13.2 Appendix: Character tables | 102 |
| 13.3 Appendix: Wannier90 input | 104 |
| 13.4 Appendix: WannierTools input | 107 |
| | |
| Bibliography | 112 |

List of Figures

| | | |
|-----|------------------------------------------------------------------------------------------------------------------------------------------------------------------------------------------------------------------------------------------------------------------------------------------------------------------------------------------------|----|
| 3.1 | DFT flow diagram for electron density self-consistent calculation. . | 21 |
| 6.1 | Schematic representation of a transport device. | 29 |
| 7.1 | Scheme for the evolution of topological non-trivial phases up to TIs. | 36 |
| 7.2 | Point-like nodal phases. (a) Dirac node, (b) Weyl nodes pair with specified chirality. | 38 |
| 8.1 | Topological quantum chemistry workflow diagram. The starting point is the ab initio calculation at the top. | 47 |
| 9.1 | a) Top and (b) side views of the PG lattice. The unit cell comprising 6 carbon atoms is enclosed in a black square. Atoms with coordination number 4 are labeled as C1, those with coordination number 3 are labeled C2. | 54 |
| 9.2 | Left panel: PG energy band structures near the Fermi level calculated with DFT (black dotted lines) and tight-binding (red solid lines). Right panel: DFT-calculated penta-graphene total DOS (black solid line), and its decomposition in s -orbital (green), p_x/p_y -orbitals (blue) and p_z orbital (orange) projected DOS | 58 |
| 9.3 | PG energy band structure near the Fermi level calculated with DFT (black dotted lines), and the two TB parameters sets, TB1 (blue lines) and TB2 (magenta lines). | 61 |
| 9.4 | Optical absorption for PG calculated with DFT (black dotted lines) and with the two tight-binding parameterizations TB1 (blue lines) and TB2 (magenta lines). | 62 |
| 9.5 | 11-PG NR lattice structure. The translational unit cell is marked between two black lines. The labeling based in longitudinal chains is herein illustrated. | 62 |
| 9.6 | Energy band structures for 17-PG NR and 23-PG NR. Top panels (black lines) are computed with SIESTA; bottom panels (red lines) are the TB results. | 64 |
| 9.7 | Optical absorption for 17- to 23-PG NRs calculated with (a) TB; and (b) DFT (SIESTA). For the sake of clarity each curve is shifted a fixed amount. | 65 |

| | | |
|-------|----------------------------------------------------------------------------------------------------------------------------------------------------------|----|
| 9.8 | Band structure for bilayer penta-graphene in tight binding and DFT. | 67 |
| 9.9 | Transmission function for monolayer PGNR and a bilayer-PGNR with 6-slices in the central region. | 68 |
| 9.10 | Thermoelectric coefficients for a 6-slice bilayer PGNR. | 69 |
| 10.1 | a) 2D projection of Wyckoff positions and b) 2D Brillouin zone for space group no. 113 | 74 |
| 10.2 | Scheme of the energy ordering of bands (irreps) to some particular sequence at HSP and HSL. | 78 |
| 10.3 | Li-PG relaxed lattice. | 80 |
| 10.4 | Li-PG and Na-PG band structure. | 81 |
| 10.5 | Band structures for doped PG penta-materials. | 82 |
| 10.6 | BZ cuts for the band structure of penta-NC ₂ | 82 |
| 10.7 | Band structure for penta-PC ₂ with SOC. | 83 |
| 10.8 | DFT band structure calculation for Mn-PG. | 84 |
| 10.9 | Mn-PG bands from the Wannier90 code. | 85 |
| 10.10 | Top: WCC evolution. Bottom: sum of WCC for the x direction. | 87 |
| 10.11 | Top: WCC evolution. Bottom: sum of WCC for the x direction. | 88 |
| 10.12 | (100) band structure for a 10-slab along $X\Gamma X$ BZ path. Color scale indicates surface weight, with +1 for right edge and -1 for left edge. | 89 |
| 10.13 | (010) band structure for a 10-slab along $X\Gamma X$ BZ path. Color scale indicates surface weight, with +1 for right edge and -1 for left edge. | 90 |
| 10.14 | (110) band structure for a 10-slab along $X\Gamma X$ BZ path. Color scale indicates surface weight, with +1 for right edge and -1 for left edge. | 91 |
| 12.1 | Layer decomposition of a transport system. | 98 |

List of Tables

| | | |
|------|----------------------------------------------------------------------------------------------------------------------------------------------------------------------------------------------|----|
| 8.1 | Periodic table for strong topological insulators and topological superconductors. Adapted from [1]. | 48 |
| 8.2 | Periodic table for topological semimetals. $p = d - d_{FS}$ is the Fermi surface codimension where d_{FS} is the FS dimension. FS1 takes p at HSP and FS2 is for p out of HSP. | 49 |
| 9.1 | Slater-Koster tight-binding parameters (in eV) for PG. | 57 |
| 9.2 | Set TB1 of Slater-Koster tight-binding parameters (in eV) for PG. | 60 |
| 9.3 | Set TB2 of Slater-Koster tight-binding parameters (in eV) for PG. | 60 |
| 10.1 | Character table for point group isomorphic to space group no. 113 | 71 |
| 10.2 | Character table for group G_M | 72 |
| 10.3 | Character table for group G_Y . $\omega = e^{i\mathbf{k}_Y \cdot \mathbf{t}}$ | 72 |
| 10.4 | Character table for the 4e WP site-symmetry group. | 75 |
| 10.5 | Band representation for 4e WP with TR and no SOC. | 76 |
| 10.6 | Band representation for 4e WP, with SOC and TR. | 76 |
| 10.7 | Band representation for 4e WP with SOC and no TR | 76 |
| 10.8 | Topological phases | 77 |

Part I

Theoretical fundamentals

Chapter 1

Introduction

Condensed matter physics is nowadays a very active research field with an immense range of applications both theoretical and applied. The main aspect that concerns to this branch of physics is the collective behavior of microscopic constituents of material systems as well as the physical phenomena that arise from the associated particle interactions. One of the milestones of condensed matter systems is that they are composed of a huge amount of particles. This implies that it has to deal with many-body systems and as such, emergent phenomena are preponderant, meaning that physical properties of systems arise due to interaction effects and a free-particle description is not adequate in general.

In addition to this particle number issue, another aspect is of remarkable importance. Namely, the dimension of the system under study. Here we understand by dimension as the degrees of freedom which are not confined under a spatial reduction of the system. Thus, we can have as possible configurations the well-known three-dimensional solids and also two-dimensional layered structures, one-dimensional ribbons or chain systems and zero-dimensional dot structures. From two dimensions down to zero dimension the spatially confined dimension is on the nanometer regime and thus these cases are denoted generally as *nanostructures*. These low-dimensional systems are the focus of intense research at the present time because of their great potential to achieve new physical phenomena due to the preponderance that quantum mechanical effects acquire in this reduced-dimension regime.

Another topic that had has a tremendous impact in recent years is the consideration of the global features of solids that are universal to a particular class of systems. Systems with properties that are robust to some degree against symmetry-conserving perturbations are of high importance for future applications in quantum-based technologies. These materials are called topological quantum materials, and comprise diverse kinds of systems such as insulators, metal, semi-metals, superconductors among others.

Following these trends, this thesis aims to be a contribution to the study of nanostructured systems and their related physical properties. We explore

phenomena concerning to electronic, optical, transport and topological properties of a recently proposed family of materials called *pentagonal materials*, where the atomic distribution in the lattice structure resembles the Cairo tiling with an additional buckled character. The general lattice structure for these materials is presented in fig. 9.1. These systems are composed of a wide range of elements and many stable and metastable configurations have been found recently [2, 3, 4].

The most studied example up to now is penta-graphene (PG), a new 2D carbon allotrope, that could be obtained from T12-carbon by breaking the covalent bonds between layers [4]. Although PG is a *metastable* carbon allotrope compared to graphene, it is energetically more favorable than the icosahedral fullerene C_{20} or the smallest nanotube, which have been synthesized. So despite some claims regarding its instability [5, 6], it is reasonable to expect that PG might be experimentally viable. Analogously to graphene, PG could be encapsulated by hexagonal boron nitride (hBN); this could help to achieve stability, besides providing insulation from chemical agents [7].

Penta-graphene has been predicted to possess several unique characteristics. It is not completely planar, and it does not have a hexagonal lattice; its 2D projection resembles the Cairo tiling, being composed of fused pentagons. From the electronic viewpoint, it is a semiconductor with a quasi-direct band gap [4], being attractive for opto-electronic applications. For instance, it has been found that PG has a reduced thermal conductivity compared to graphene [8, 9, 10] and it is an auxetic material, i.e., it has a negative Poisson's ratio [4, 11]. It has been proposed for applications such as an anode material in alkaline batteries [12], as a metal-free catalyst for CO oxidation [13] and for use in hydrogen storage systems [2].

As in other 2D systems, the properties of nanostructures with lower dimensions based in PG have been also explored. For example, PG nanoribbons [4, 6, 14] multilayer PG [6, 15] and PG nanotubes [4, 6, 14], which might be even more stable than monolayer PG. Most of these works employ a first-principles approach; recently, a tight-binding (TB) model has been put forward, allowing for the obtention of the electronic bands and an analytical expression for the optical absorption [16]. In fact, Zhang *et al.* also provided a minimal tight-binding parameterization in their work, but with a limited agreement to the ab-initio bands [4].

Other pentagonal materials have received less attention than PG. There have been studies in new materials based on PG with substitutional doping or atomic adsorption that can form new pentagonal materials with different electronic properties compared to PG [3, 17, 2]. Other non-carbon-based pentagonal materials have been also studied among which can be named penta-BN₂, penta-silicene and penta-germanene among others [18, 19].

This considerable amount of pentagonal materials presents a great range of interesting properties, from high performance in thermoelectric phenomena, such as thermal conductivity in PG, to topological phases, presenting novel symmetry-protected non-trivial behavior.

All pentagonal materials considered in this thesis are based in penta-graphene,

which is the main system studied in this work. We doped penta-graphene with metallic and non metallic elements in order to design some new phases based on band filling constraints.

However, we give a detailed analysis of the general pentagonal lattice and its associated symmetry properties to show how the general properties in the behavior of energy bands in momentum space, such as connectivity and degeneracies, are equally valid for all pentagonal materials.

Chapter 2

Symmetry tools: group theory basics

It is difficult to find a topic more omnipresent in science than symmetry in all its facets. We encounter it from such diverse systems as atoms and molecules to complex living and nonliving organisms, encompassing a huge range of length scales [20, 21].

In passing across this wide plethora of examples, we find that symmetry plays a crucial role in the understanding of inorganic crystalline structures, where many manifestations of symmetry lie behind the general behavior of electrons and ions in a periodic crystal [22]. In this context, symmetry allows to predict deep results about how crystal quasiparticles will act inside the material microscopic landscape.

These results come from a fundamental relation; symmetry in quantum mechanics is directly linked to degeneracies in the spectrum of quantum mechanical operators [23]. As such, finding a degeneracy permits us to foretell if the system we are studying is invariant under the action of a symmetry operation and *vice versa*.¹

Inquiring further about the former assertion, we find that symmetries can be in general, represented by unitary or antiunitary operators [25]. Thus, if we describe our system by a Hamiltonian operator in Hilbert space, the action of a symmetry operator U , will be given formally by

$$UHU^{-1} = H. \tag{2.1}$$

From this expression we can see straightforwardly that a symmetry operation is linked to a operator commuting with the Hamiltonian of the system. The well-known consequences of this commuting situation, are that U and H will share the same eigenvalues and will be diagonal with respect to the same basis [26].

¹An exception to this general rule is associated to the presence of *accidental degeneracies*, which in principle are not rooted in any evident symmetry [24].

In general, physical systems stay invariant under the action of more than one symmetry operator, and therefore we can define a set G of operations that commutes with the Hamiltonian. When this happens, we are able to endow this operator set with a precise structure having the following rules

- There exists a multiplication rule \star within this set as $A\star B$, where $A \in G$ and $B \in G$.
- The identity operator E acting as $E\star H = E$ is part of the set.
- For every symmetry operation A there exists another operator $A^{-1} \in G$ such that $A\star A^{-1} = E$.
- The set G is closed under multiplication. That is, if we have $A \in G$ and $B \in G$ then $A\star B = C \in G$.
- Multiplication rule \star holds the following property for elements $A, B, C \in G$.

$$(A\star B)\star C = A\star(B\star C) \quad (2.2)$$

A set fulfilling these formal rules is called a *group* [25]. The set of symmetry operations for a physical system forms a group structure, and it is called the *symmetry group* of the system. Equipped with this last result, we can apply all the group theoretical machinery to extract conclusions related to symmetry.

To begin with, we can see that the multiplication rule is the source of connection among group elements. This implies that we can build some table, a *multiplication table*, that summarizes all the possible relations under this operation within a group. For example, for an abstract group G composed of $\{E, A, B, C, D, F\}$ we can have the following multiplication table.

| | | | | | | |
|---|---|---|---|---|---|---|
| | E | A | B | C | D | F |
| E | E | A | B | C | D | F |
| A | A | E | D | F | B | C |
| B | B | F | E | D | C | A |
| C | C | D | F | E | A | B |
| D | D | C | A | B | F | E |
| F | F | B | C | A | E | D |

Multiplication tables condense all the information of the group combination rule and serves to classify the operations in the symmetry group.

As the amount of elements in a group grows considerably, it is necessary to find other ways to express the essential information of the group. To accomplish that, we have to define some important concepts. First, a new form of classification can be based on [27]

Definition (conjugated elements). Two elements of a group, A and B are said to be conjugate if there exists an arbitrary element $X \in G$ such that $B = XAX^{-1}$.

From this, a new classification arise using the following

Definition (conjugation classes). A *class* is the totality of elements which can be obtained from a given group by conjugation.

For example, from the above multiplication table, the associated group can be divided in three conjugation classes; $\{(E); (A, B, C); (D, F)\}$. In loose manner we can say that classes are subset of symmetry elements that are closed under conjugation. These elements shares some geometrical and analytical properties as we will see soon.

The other key definition is related to how we can give an operational use to this group structure. This arises from the following [27]

Definition (representation). A representation of a group is a substitution group (in general a matrix group) such that this new group is homomorphic or isomorphic to the abstract group. To every group element A of G , a matrix $D(A)$ is assigned, such that $D(AB) = D(A)D(B)$.

This last operation has to be understood as matrix multiplication.

Representations are in general not unique, but are related by canonical transformations [26]. The dimension of a representation is equal to the dimension of each of its matrices (square matrices). The ambiguity of the representation definition can be reduced by [27]

Definition (irreducible representation). If by one and the same canonical transformation, all the matrices in the representation of a group can be made to acquire the same block form, then the representation is said to be *reducible*, otherwise it is *irreducible*. Thus, an irreducible representation cannot be expressed in terms of representations of lower dimension.

Therefore, irreducible representations (irreps) are the basic building blocks for all representations of a group. If Γ_R is a reducible representation then it can always be expressed as a direct sum of irreducible representations Γ_i such that

$$\Gamma_R = \sum_i \alpha_i \Gamma_i, \quad (2.3)$$

where α_i represents multiplicity of the i-th irrep in the above sum.

An illustration of an irreducible representation for the example group presented before is given by

$$\Gamma_E = \begin{pmatrix} 1 & 0 \\ 0 & 1 \end{pmatrix}, \Gamma_A = \begin{pmatrix} -1 & 0 \\ 0 & 1 \end{pmatrix}, \Gamma_B = \begin{pmatrix} \frac{1}{2} & -\frac{\sqrt{3}}{2} \\ -\frac{\sqrt{3}}{2} & -\frac{1}{2} \end{pmatrix}, \quad (2.4)$$

$$\Gamma_C = \begin{pmatrix} \frac{1}{2} & \frac{\sqrt{3}}{2} \\ \frac{\sqrt{3}}{2} & -\frac{1}{2} \end{pmatrix}, \Gamma_D = \begin{pmatrix} -\frac{1}{2} & \frac{\sqrt{3}}{2} \\ -\frac{\sqrt{3}}{2} & -\frac{1}{2} \end{pmatrix}, \Gamma_F = \begin{pmatrix} -\frac{1}{2} & -\frac{\sqrt{3}}{2} \\ \frac{\sqrt{3}}{2} & -\frac{1}{2} \end{pmatrix}.$$

As can be seen, it is a two-dimensional irreducible representation.

Now, an important consequence is that for the groups we are interested in (groups with a finite number of elements), there is a finite number of irreducible representations [26]. These irreps represent subspaces of the system for which the eigenvectors transform in a closed way. Thus, they will have the same eigenvalue, or equivalently, they comprise a degeneracy of the system. In this way, it is possible to partition the Hamiltonian of the system in a block form, where each block results from a unique irrep. If the system is under a perturbation that changes the symmetry group, some irreps can be mapped to reducible representation in the new group [25]. Group theory allows to clearly elucidate how this degeneracy transition occurs, although no quantitative information about the magnitude of the actual eigenvalues can be extracted.

For a complete characterization of the degeneracy features of a system, we need information about how the elements in the group behave within each irrep. It is not necessary to deal with all elements of the group but only with conjugation classes, since all share same practical interpretation in terms of symmetry. Thus, we need a means to describe a whole class with respect to a given irrep. For this we need a *class invariant quantity*. The most commonly used entity for this purpose is the *character of a matrix representation* which can be defined as [27]

Definition (Character). The *character* $\chi^{\Gamma_j}(R)$ of the matrix representation $\Gamma_j(R)$ for a symmetry operator R , is the trace (sum over diagonal) of the matrix associated with R in $\Gamma_j(R)$. That is

$$\chi^{\Gamma_j}(R) = \sum_{\mu=1}^{l_j} D^{(\Gamma_j)}(R)_{\mu\mu}. \quad (2.5)$$

Where l_j is the irrep dimension and j is the irrep index.

From this definition, and taking into account that a similarity transformation leaves the trace invariant, we obtain that the character is invariant across the entire class.

We are in possession of a relation between conjugation classes and irreps through characters χ . This allows to condensate the behavior of the symmetry elements for all the irreps of a given group, which is done in the so-called *character tables*. These tables are constructed with the row index running along irreps and the column index going over conjugation classes. Entries for the table are the character corresponding to a class for a particular irrep. As an example, we give here the character table for the group of the previous examples

| | | | |
|-------------|-------|--------|--------|
| | C_1 | $3C_2$ | $2C_3$ |
| Γ_1 | 1 | 1 | 1 |
| Γ'_1 | 1 | -1 | 1 |
| Γ_2 | 2 | 0 | -1 |

where $C_1 = \{E\}$, $C_2 = \{A, B, C\}$ and $C_3 = \{D, F\}$.

Some comments are in order. Clearly, the identity class has characters (first column) which are related to the dimension of each irrep. Also we see that one-dimensional representations are actually represented by its characters, and the trivial representation, with all characters equal to one, is always present in a character table [27].

Character tables for all the groups of interest in crystalline solids are tabulated in several places [25, 28]. Thus, we refer to this sources when the information for the symmetry group is required.

With the information of a character table we can decompose every representation of a group in terms of its irreps. This is a very powerful result, since it gives the maximal number of degeneracies that can be present in a given system.

Also, character tables contain information about how a given operator transforms under the symmetry group [27]. In more detail, perturbations or internal properties of the system are represented in general by some n -rank tensor quantity [23]. This tensor will transform in a definite way under the symmetry operations of the group. Analyzing the action of the operations, it allows us to identify under which irrep(s) the tensor transforms. This decomposition gives valuable information about the possible outcomes for the perturbation.

□In summary, the use of group theory on practical grounds is used to characterize the degeneracy landscape for the eigenvalue spectra of some operators, the most interesting being energy spectra from the Hamiltonian. Degeneracies are related to the dimension of the irreps which compose the most fundamental representation for a given group. Additionally we can decompose any tensorial product operator acting on the system in terms of these irreps, in order to find how the associated spectrum separates in disjoint classes. We will be using these group theoretical tools intensively along this thesis, and accordingly, more details of the actual application of these methods will be given later.□

Chapter 3

First-principles methods: Density Functional Theory

We have seen in the previous section that symmetry plays a central role in the qualitative description of a condensed matter system. However, group theoretical tools alone are not sufficient for a successful study; we have to obtain quantitative information about the energy spectrum and related properties.

For this study the focus is to obtain the energy eigenstates of the system. This is accomplished by solving the associated wave equation. In the cases of interest we start by solving the Schrödinger equation [22]¹

$$i\hbar\partial_t |\psi_j(t)\rangle = \hat{H} |\psi_j(t)\rangle, \quad (3.1)$$

where i is the imaginary unit, \hbar is the reduced Planck's constant, \hat{H} is the Hamiltonian operator and $|\psi_j(t)\rangle$ is the time-dependent eigenstate of the system, labeled by some set j of quantum numbers.

Temporal dependence can be expressed in the usual way as $|\psi_j(t)\rangle = e^{-i\frac{E_j t}{\hbar}} |\psi_j\rangle$, where $|\psi_j\rangle$ is an eigenstate of the time-independent Schrödinger equation

$$\hat{H} |\psi_j\rangle = E_n |\psi_j\rangle. \quad (3.2)$$

Here E_j represents the energy eigenvalues for the Hamiltonian \hat{H} .

Now in the systems of interest, we will be dealing with a many-body problem, since a prodigious number of electrons and ions is present composing the crystal structure (about the order of $\sim 10^{26}$ particles) [27]. In this context the eigenstate $|\psi_j\rangle$ is called a *many-body wavefunction* and the Hamiltonian \hat{H} is an interacting operator expressed in general terms by [30]

$$\hat{H} = \hat{T} + \hat{V}_{ee} + \hat{V}_{ext}, \quad (3.3)$$

where \hat{T} is the kinetic energy operator, \hat{V}_{ee} is the interaction potential and \hat{V}_{ext} is an external potential applied to the system.

¹It is possible that also a relativistic wave equation arises related to effective models [29]. Nevertheless, the fundamental description continues being the Schrödinger equation.

The Schrödinger equation for a many-body system is not currently solvable in analytical closed form [31]. Even having a solution, useful information could not be extracted directly from it, due to the intricacies that a wavefunction with this character might contain [32]. Because of this, decades ago general methods to find energy eigenvalues for many-body systems were developed [33, 34].

In fact, a group of the most powerful electronic structure calculation methods is based on two theorems due to Hohenberg and Kohn [33], which assert the following

Theorem For a given many body system with external potential \hat{V}_{ext} , the associated electron density $n(\mathbf{r})$ is uniquely defined, being this mapping one to one and with an inverse.

Theorem If there exists a density function $n(\mathbf{r})$ for which the total energy of the system is a minimum, then this density is the *ground state density*.

It is not our intention to prove this two theorems here, since they are extensively revised in literature (see [35, 36] for example). Instead, we will apply them to the formulation of the method we use to calculate electronic structure, namely, *density functional theory*.

From the above results, one can deduce that all the electronic properties of the system in its ground state will depend on the density function $n(\mathbf{r})$ [37]. Then we can formulate an energy function that depends on density, which in turn is also a function. Thereby energy becomes an *energy functional* $E[n(\mathbf{r})]$ defined by [30]

$$E[n(\mathbf{r})] = T[n(\mathbf{r})] + V_{ee}[n(\mathbf{r})] + \int v_{ext}(\mathbf{r})n(\mathbf{r})d\mathbf{r}, \quad (3.4)$$

where $V_{ext} = \int v_{ext}(\mathbf{r})\delta(\mathbf{r}-\mathbf{r}')d\mathbf{r}$.

It can be noted that we have a universal functional $F[n(\mathbf{r})] = T[n(\mathbf{r})] + V_{ee}[n(\mathbf{r})]$ which is system-independent (the explicit form of F is until now unknown [31]). Minimization of this functional with respect to $n(\mathbf{r})$ will in principle yield the ground state solution [35].

Albeit powerful and far-reaching, the above theorems are only existence results, giving no algorithmic procedure to actually obtain the ground state electron density. However, they gave the starting point for a computational procedure, such that soon afterwards, a practical way to calculate $n(\mathbf{r})$ was put forward by Kohn and Sham [34].

This procedure is based on a simple idea, namely, to map the original interacting electron system into a non-interacting fictitious system, which shares the same energy electron density [37]. The advantage is that in this non-interacting system the electron density can be expressed as

$$n(\mathbf{r}) = \sum_i \phi_i^*(\mathbf{r})\phi_i(\mathbf{r}), \quad (3.5)$$

where $\{\phi_i(\mathbf{r})\}$ are orthonormal orbitals, called Kohn-Sham (K-S) eigenfunctions [30]. These eigenfunctions are solutions of a non-interacting Schrödinger equation $H_{NI} \phi_i(\mathbf{r}) = \epsilon_i \phi_i(\mathbf{r})$, where ϵ_i are the so-called Kohn-Sham energies.

To obtain the explicit form for the target non-interacting Hamiltonian, we first rewrite the energy functional as

$$E[n] = T_0[n] + V_H[n] + \int v_{ext}(\mathbf{r})n(\mathbf{r})d\mathbf{r} + E_{xc}[n], \quad (3.6)$$

where T_0 is the non-interacting part of the kinetic energy, $V_H[n]$ is the Hartree potential given by

$$V_H[n] = \frac{1}{2} \int n(\mathbf{r}) \frac{e^2 n(\mathbf{r}') d\mathbf{r} d\mathbf{r}'}{|\mathbf{r} - \mathbf{r}'|} \quad (3.7)$$

and $E_{xc}[n]$ is defined as the exchange-correlation functional defined as

$$E_{xc}[n] = T[n] - T_0[n] + V_{ee}[n] - V_H[n]. \quad (3.8)$$

Expressing the energy functional in the Kohn-Sham basis we obtain

$$E[n] = \sum_i \langle \phi_i | -\frac{\hbar^2 \nabla^2}{2m} + v_{ext} | \phi_i \rangle + \frac{1}{2} \sum_{ij} \langle \phi_i \phi_j | \frac{e^2}{r_{12}} | \phi_i \phi_j \rangle + E_{xc}[n]. \quad (3.9)$$

Searching for a variational solution for this functional, that is, varying with respect to K-S orbitals $\{\phi_i(\mathbf{r})\}$, an effective wave equation is encountered such that

$$\left[-\frac{\hbar^2 \nabla^2}{2m} + v_{ext} + V_H + V_{xc} \right] \phi_i = \epsilon_i \phi_i, \quad (3.10)$$

where $V_{xc} = \frac{\delta E_{xc}}{\delta n(\mathbf{r})}$ is the exchange-correlation potential [37].

Equations (3.10) are the so-called *Kohn-Sham equations*. They have to be solved for the ϕ_i to calculate the electron density associated to a given external potential v_{ext} .

In order to solve the equations, a previous explicit form of the exchange-correlation functional must be fixed. This is where approximations enter in the process. The most used exchange-correlation functionals and the implied approximations are described in the literature [36, 35].

It has to be pointed out that the calculation of ϕ_i orbitals depends on the electron density itself. Thus, the K-S equations must be solved under a self-consistent procedure. This means that one must [31]

- Define an initial, trial electron density, $n(\mathbf{r})$.
- Solve the Kohn-Sham equations defined using the trial electron density and find the orbitals ϕ_i .
- Calculate the electron density defined by eq. (3.5).

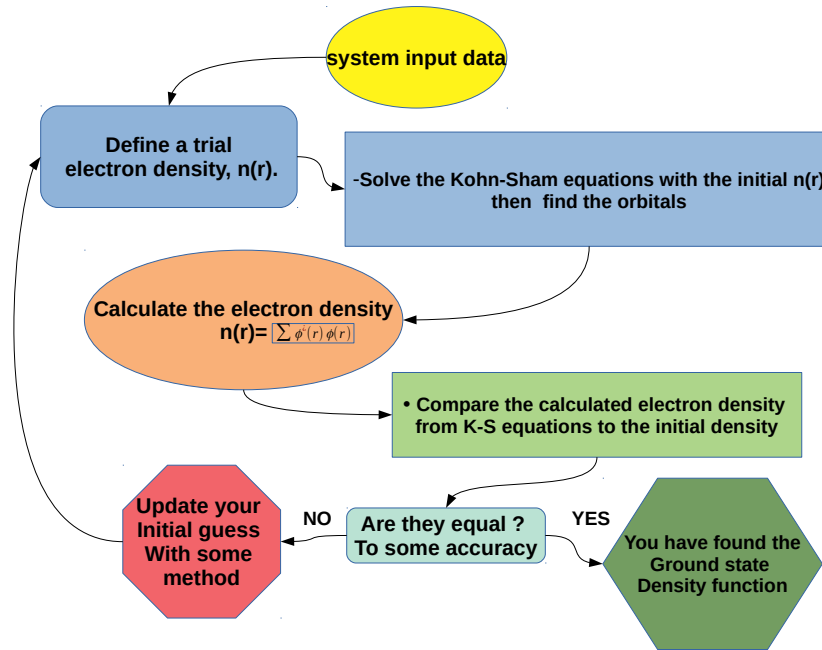


Figure 3.1: DFT flow diagram for electron density self-consistent calculation.

- Compare the calculated electron density from K-S equations to the initial density. If both are the same to some defined accuracy, this can be chosen as the ground state density. If they are different beyond the required precision, the trial electron density must be updated in some way. Once this is done, the process restarts.

This algorithm is depicted in a diagrammatic way in fig.3.1.

On the practical side, we must mention that there are very powerful computational codes implementing the K-S procedure to find total energies and other related properties of crystals [38, 39]. These packages resort to an approximate solution of this self-consistent set of equations, with a minimum input from the user. This is mostly related to the range for when self-consistency is reached, and criteria for the electron density mixing at restarting the loop [35, 31]. Additional technical details are also important to achieve successful, accurate calculations that correspond to experiments. These intricacies will be discussed accordingly as we move forward in this work.

Chapter 4

Tight-binding method

First-principles methods presented in the last section, are based in very general results combined with some approximations that group all the unknown information of the system, exchange-correlation in particular, and treats it in a numerical fashion, hiding direct physical meaning of the process until an output is obtained [40]. Although very powerful in their results, it is always desirable to have some physical intuition of what is happening in a phenomenological sense from the microscopic viewpoint of the system. This vision was present before first-principles methods entered the scene, and is based on the appealing result that microscopic constituents of solids, that is atoms, are the best initial basis set to describe an extended condensed matter system [22]. This approach, based on the combination of atomic orbitals is known widely as the *tight-binding method* [30].

The basic idea to implement a tight-binding approach is that we can solve time-independent Schrödinger equation (3.2) expanding the states using an atomic basis. This basis is formed by localized orbitals coming from atomic physics, we denote them as $\varphi_\alpha(\mathbf{r} - \mathbf{t})$, where α is an index for the orbital type (s, p, d, f) and \mathbf{t} is the center position of the orbital. If we apply Bloch's theorem for the periodic crystal structure [22], we can construct an extended state over the entire lattice as

$$\chi_{\mathbf{k}\alpha l}(\mathbf{r}) = \frac{1}{\sqrt{N}} \sum_{\mathbf{R}} e^{i\mathbf{k}\cdot\mathbf{R}} \varphi_\alpha(\mathbf{r} - \mathbf{t}_l - \mathbf{R}), \quad (4.1)$$

where l is an index for atoms, \mathbf{R} is the position vector connecting to other atoms, N is the number of unit cells in the system and \mathbf{k} is the reciprocal lattice vector.

With this Bloch basis it is possible to expand the eigenstates of the system as a linear combination given by

$$|\psi_{\mathbf{k}}(\mathbf{r})\rangle = \sum_{\alpha, l} C_{\mathbf{k}\alpha l} \chi_{\mathbf{k}\alpha l}(\mathbf{r}), \quad (4.2)$$

where the $C_{\mathbf{k}\alpha l}$ are the expansion coefficients.

Now using the projected Schrödinger equation

$$\langle \psi'_{\mathbf{k}}(\mathbf{r}) | H | \psi_{\mathbf{k}}(\mathbf{r}) \rangle = \langle \psi'_{\mathbf{k}}(\mathbf{r}) | E | \psi_{\mathbf{k}}(\mathbf{r}) \rangle,$$

with the previous expansion in eq. (4.2) we get

$$\sum_{\alpha, \beta, l, j} [\langle \chi_{\mathbf{k}\alpha l}(\mathbf{r}) | H | \chi_{\mathbf{k}\beta j}(\mathbf{r}) \rangle - E_{\mathbf{k}} \langle \chi_{\mathbf{k}\alpha l}(\mathbf{r}) | \chi_{\mathbf{k}\beta j}(\mathbf{r}) \rangle] C_{\mathbf{k}\alpha l} C_{\mathbf{k}\beta j} = 0. \quad (4.3)$$

This is the most general form of the wave equation in a tight-binding basis. It implies a general sum over all atoms in the lattice and in principle could contain an arbitrary number of orbitals as N grows. In order to make the method practical, approximations have to be implemented. The most widely used, also chosen herein, is the Slater-Koster parameterization [41].

4.1 Slater-Koster parameterization

Solving the secular equation for tight-binding method requires the computation of two matrices

- $\langle \chi_{\mathbf{k}\alpha l}(\mathbf{r}) | \chi_{\mathbf{k}\beta j}(\mathbf{r}) \rangle$: the overlap matrix,
- $\langle \chi_{\mathbf{k}\alpha l}(\mathbf{r}) | H | \chi_{\mathbf{k}\beta j}(\mathbf{r}) \rangle$: Hamiltonian matrix in the TB basis.

To make practical use of the method, both matrices have to be constrained in some sense; this set of constraints is called the Slater-Koster (S-K) parameterization [41]. But before that, the first important approximation is to restrict us only to a finite number of orbitals for the basis, where in general just most representative s , p , d and f orbitals for each atom are picked [40]. With this finite basis, both matrices above become finite-dimensional.

There exist two forms to treat the overlap matrix. In the most direct way we consider that atomic orbitals are non-orthogonal to each other and then matrix elements are considered as unknown parameters of the system. As it is foreseeable, this is the *non-orthogonal S-K* parameterization [30]. In the opposite case, we consider that the atomic orbitals are orthonormal to each other or that the overlap between them can be neglected altogether, such that

$$\langle \varphi_{\alpha}(\mathbf{r} - \mathbf{t}_i) | \varphi_{\beta}(\mathbf{r} - \mathbf{t}_j - \mathbf{R}) \rangle = \delta_{\alpha\beta} \delta_{ij}. \quad (4.4)$$

In this case we have the *orthogonal S-K* parameterization [30], which reduces the number of free parameters in the process.

Next, we analyze the Hamiltonian matrix. We make patent one of the central approximations of the procedure. Note that, in principle, the sum over \mathbf{R} is defined over all atoms in the crystal. This is factually impracticable, thus an educated restriction over this sum must be put forward. In general terms, truncation of this sum must be settled by some geometrical judgment. The most used criterion is to restrict it only to a finite and very small number of nearest neighbors for each atom in the primitive unit cell [40]. This cutoff is

very convenient and is justified by the localized character of the orbital basis we are using [22].

Another issue to consider arises relative to the explicit form for the Hamiltonian matrix, which is

$$\langle \chi_{k\alpha i}(\mathbf{r}) | H | \chi_{k\beta j}(\mathbf{r}) \rangle = \sum_{\langle \mathbf{R} \rangle} e^{i\mathbf{k} \cdot \mathbf{R}} \langle \varphi_{\alpha}(\mathbf{r} - \mathbf{t}_i) | H | \varphi_{\beta}(\mathbf{r} - \mathbf{t}_j - \mathbf{R}) \rangle,$$

where now $\langle \mathbf{R} \rangle$ denotes the sum restricted to nearest neighbors. In this expression the matrix elements in the orbital basis $\langle \varphi_{\alpha}(\mathbf{r} - \mathbf{t}_i) | H | \varphi_{\beta}(\mathbf{r} - \mathbf{t}_j - \mathbf{R}) \rangle$ have to be explicitly calculated. This computation is hardly feasible due to technical limitations [40]. The central theme in S-K approach is how to approximate these integrals.

For this end, we take the Hamiltonian operator to be of the form [30]

$$H = -\frac{1}{2}\nabla^2 + \sum_{k,l,j} V^k[\mathbf{r} - (\mathbf{t}_l + \mathbf{R}_j)]. \quad (4.5)$$

In calculating the matrix elements for this operator we encounter three possible cases for the integrals involved depending on the location of the orbitals in the basis and the crystalline potential V . We describe them as [41]

- *1-center integrals*: In this case the integral between the Hamiltonian and orbitals have both, orbitals and potential V , located at the same spatial place.
- *2-center integrals*: In these integrals, either both orbitals are located at the same place and the potential is at a different location, or one orbital and the potential V coincide in location, while the other orbital is in a distinct position.
- *3-center integral*: In this situation all the factors, both orbitals and potential V are located at different positions in space.

What Slater and Koster showed was that 2-center integrals are the most important contribution for a wide range of systems, and 3-center integrals can be safely neglected in many cases [40]. This type of integrals requires only one free parameter per case, reducing the amount of unknowns in the system.

Therefore, integrals $\langle \varphi_{\alpha}(\mathbf{r} - \mathbf{t}_i) | H | \varphi_{\beta}(\mathbf{r} - \mathbf{t}_j - \mathbf{R}) \rangle$, difficult to compute directly, are defined now as *adjustable parameters* of the model, such that we must assign them a reduced label $K_{\alpha\beta,ij}$ implying that

$$\langle \chi_{k\alpha i}(\mathbf{r}) | H | \chi_{k\beta j}(\mathbf{r}) \rangle = \sum_{\langle \mathbf{R} \rangle} e^{i\mathbf{k} \cdot \mathbf{R}} K_{\alpha\beta,ij}. \quad (4.6)$$

This is the S-K form for the TB Hamiltonian [42]. Slater and Koster, using 2-center integrals give a more explicit form for these integrals in terms of the orientability in real space related to the \mathbf{R} vector, which is expressed as

$K_{\alpha\beta,ij} = K_{\alpha\beta}(\mathbf{R}_{ij})$, where $\mathbf{R}_{ij} = (R_x, R_y, R_z) = d(l, m, n)$. Here d is the distance modulus between two neighbors and l, m and n are the direction cosines for the \mathbf{R} vector [22]. Starting with this prescription, along with an explicit form for orbitals in terms of spherical harmonics, S-K obtained a general form for the orbital integrals [41]. An adapted table for the most used expressions is given here

| |
|-------------------------------------------------|
| $K_{ss} = V_{ss\sigma}$ |
| $K_{sx} = lV_{sp\sigma}$ |
| $K_{sy} = mV_{sp\sigma}$ |
| $K_{sz} = nV_{sp\sigma}$ |
| $K_{xx} = l^2V_{pp\sigma} + (1 - l^2)V_{pp\pi}$ |
| $K_{yy} = m^2V_{pp\sigma} + (1 - m^2)V_{pp\pi}$ |
| $K_{zz} = n^2V_{pp\sigma} + (1 - n^2)V_{pp\pi}$ |
| $K_{xy} = lm(V_{pp\sigma} - V_{pp\pi})$ |
| $K_{xz} = ln(V_{pp\sigma} - V_{pp\pi})$ |
| $K_{yz} = mn(V_{pp\sigma} - V_{pp\pi})$ |

In this table the expressions $V_{\alpha\beta\zeta}$ are the well known S-K tight-binding parameters. These are the free parameters to be adjusted in modeling the electronic band structure of a particular material.

□In summary, we set a microscopic model for the system we are interested in by picking the most important orbital contribution for each atom in the lattice structure. We then build an atomic basis for the entire primitive unit cell and fix the dimension of the Hamiltonian to a ($\#atoms \times \#orbitals$) by ($\#atoms \times \#orbitals$) matrix. Based on geometrical or localization criteria we restrict the \mathbf{R} sum up to some amount of nearest neighbors. With this we formulate the Hamiltonian matrix in terms of S-K parameters.

The free parameters of the system must be fixed by some referential band structure obtained from experimental results (ARPES measurements for example) or by some first-principles computation [37]. This process fits the energy bands in the best possible way with respect to the finite set of S-K parameters over the entire Brillouin zone. Once this procedure is completed, the TB model for the chosen range of energy is successfully implemented. This model could be used to calculate additional physical properties of the system, such as the optical and transport responses, as we will show in following sections.□

Chapter 5

Optical response in the tight-binding approximation

One of the most direct forms to study the internal properties of a system, being a bulk material or a case of reduced dimension is by means of external perturbations. These external perturbations induce some excitation in the system, which later cause a relaxation response with a definite change of the associated physical property. In particular, one of the preponderant perturbations in any experimental study is the interaction of the system with an external electromagnetic (EM) field.

Within this setting, optical response is a very important branch and the linear regime of the optical spectrum of materials is a very interesting piece of data to design new technologies and applications [43].

Linear optical response is related to the study of electronic quantum transitions induced by an external EM field. In a perturbative regime, using Fermi's golden rule, band to band transitions from an initial state $|i\rangle$ to a final state $|f\rangle$ has a probability per unit time given by [44]

$$\wp_{i \rightarrow f} = \frac{2\pi}{\hbar} |\langle f | H_{ext} | i \rangle|^2 \delta(E_f - E_i \pm \hbar\omega), \quad (5.1)$$

where H_{ext} is the external perturbation Hamiltonian, ω is the external perturbation characteristic frequency and $E_{f/i}$ is the energy of the final/initial state. The matrix element $\langle f | H_{ext} | i \rangle$ is called the transition matrix element and will be denoted by $P_{cv}(\mathbf{k})$.

In order to obtain the number of transitions per unit time per unit volume W , induced by some external frequency ω , we have to sum all probabilities over reciprocal space, spin and conduction and valence band indices. This gives us [30]

$$W(\omega) = \frac{2\pi}{\hbar} \sum_{c,v,\mathbf{k}} |P_{cv}(\mathbf{k})|^2 \delta(E_c(\mathbf{k}) - E_v(\mathbf{k}) - \hbar\omega). \quad (5.2)$$

Where E_c and E_v correspond to the energy of the valence and conduction band, respectively.

Now we define the absorption coefficient $\alpha(\omega)$ as the energy absorbed in the unit time and the unit volume per energy flux $\xi(c/n)$, where ξ is the energy density, which is given by [44]

$$\xi = \frac{n^2 E_0^2 \omega^2}{2\pi c^2}. \quad (5.3)$$

Here, n is the refraction index, c is the speed of light and E_0 is the amplitude of the electric field magnitude. Thus

$$\alpha(\omega) = \frac{\hbar\omega W(\omega)}{\xi(c/n)}, \quad (5.4)$$

and using the former definitions, the optical absorption takes the form

$$\alpha(\omega) = \frac{4\pi^2}{nc\omega E_0^2} \sum_{c,v,\mathbf{k}} |P_{cv}(\mathbf{k})|^2 \delta(E_c(\mathbf{k}) - E_v(\mathbf{k}) - \hbar\omega) \quad (5.5)$$

In particular, the transition matrix element P_{cv} depends on the perturbation Hamiltonian H_{ext} . In the dipolar approximation we can write this Hamiltonian as [30]

$$H_{ext} = H_{dip} = -\frac{e}{m} \mathbf{E} \cdot \mathbf{r}, \quad (5.6)$$

where \mathbf{r} is the position vector. From this we can express P_{cv} in the form

$$P_{cv} = -\frac{eE_0}{m} \langle c, k | \mathbf{u} \cdot \mathbf{r} | v, k \rangle = -\frac{eE_0}{m} \mathbf{u} \cdot \langle c, k | \mathbf{r} | v, k \rangle \quad (5.7)$$

where $\mathbf{E} = E_0 \mathbf{u}$ and \mathbf{u} is the polarization vector of the electric field. In this form P_{cv} is called the *dipolar matrix element* [45].

Next, we manipulate the position operator matrix element a bit. First, note a related identity [46]

$$\langle c, k | \mathbf{p} | v, k \rangle = \frac{m}{\hbar} \langle c, k | [\mathbf{r}, H] | v, k \rangle. \quad (5.8)$$

Then we use another relation given by

$$\langle c, k | \mathbf{p} | v, k \rangle = \frac{m}{i\hbar} (E_{vk} - E_{ck}) \langle c, k | \mathbf{r} | v, k \rangle. \quad (5.9)$$

Combining these two expressions we obtain

$$\langle c, k | \mathbf{r} | v, k \rangle = \frac{i}{E_{ck} - E_{vk}} \langle c, k | [H, \mathbf{r}] | v, k \rangle \quad (5.10)$$

Focusing on the band states $|n, k\rangle$, we can expand them in terms of a tight-binding basis as

$$|n, k\rangle = \sum_a C_n(a) |a, k\rangle, \quad (5.11)$$

where a is the basis index that includes orbital and atom indices.

Using the above expansion along with equation (5.7) we can rewrite the dipolar matrix element in the form

$$P_{cv} = -\frac{eE_0}{m} \mathbf{u} \cdot \left[\sum_{a,b} \frac{C_c^*(a) C_v(b) [H, \mathbf{r}]_{a,b}(\mathbf{R}_{ab})}{E_{ck} - E_{vk}} \right], \quad (5.12)$$

where $\nabla H_{a,b}$ is the gradient of the Hamiltonian matrix element between states a and b .

Returning to the optical absorption expression, we insert this dipolar matrix element and obtain

$$\alpha(\omega) = \frac{4\pi^2 e^2}{n c m^2 \omega} \sum_{c,v,\mathbf{k}} \left| \mathbf{u} \cdot \left[\sum_{a,b} \frac{C_c^*(a) C_v(b) [H, \mathbf{r}]_{ab}(\mathbf{R}_{ab})}{E_{ck} - E_{vk}} \right] \right|^2 \delta(E_{cv}(\mathbf{k}) - \hbar\omega), \quad (5.13)$$

where $E_{cv}(\mathbf{k}) = E_c(\mathbf{k}) - E_v(\mathbf{k})$.

The only missing issue is to find $[H, \mathbf{r}]_{ab}(\mathbf{R}_{ab})$. We use here the explicit form of the Hamiltonian in a tight-binding basis such that [47]

$$H_{ab}(\mathbf{R}_{ab}) = \sum_{\mathbf{R}_{ab}} e^{i\mathbf{k} \cdot \mathbf{R}_{ab}} t_{ab}(\mathbf{R}_{ab}), \quad (5.14)$$

where \mathbf{R}_{ab} are real lattice vectors and t_{ab} represent the Slater-Koster tight-binding parameters. Finally, calculating the commutator we obtain

$$[H, \mathbf{r}]_{a,b}(\mathbf{R}_{ab}) = i \sum_{\mathbf{R}_{ab}} \mathbf{R}_{ab} e^{i\mathbf{k} \cdot \mathbf{R}_{ab}} t_{ab}. \quad (5.15)$$

Inserting this expression in equation (5.13) we obtain the final form for the optical absorption that is used in numerical calculations.

This expression can be coded to calculate the optical response using a TB parameterization obtained before. Also, and as we will comment in following sections, this expression can be used to constraint the TB parameterization with the aim to obtain fitting results that give a good description not only of the electronic band structure but for the optical spectra as well.

Chapter 6

Electronic transport

Another form of physical response which takes place when an external EM field is applied, is the electron transport through a sample [22]. In this case, a flux of electrons is carried from one side of the system to the other due to a electronic potential gradient, producing a net electronic current I , which is a measurable quantity [48].

Electronic transport implies that the system is out of equilibrium. Still one can study the most simple cases assuming that the gradient producing the current generates only a low bias situation [49]. We will present the formalism for this regime, taking as an additional restriction a low temperature regime.

To start with, we define the general form of the device that will be used from now on. The device could be divided in three zones. Two lateral regions, denoted as the electrodes (left and right electrodes) and a central zone, the

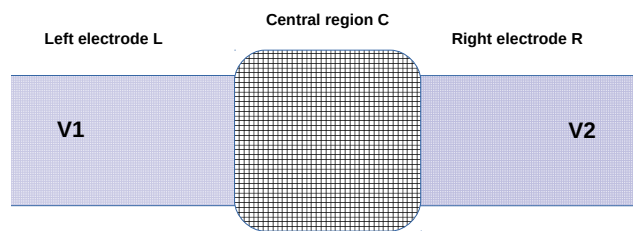


Figure 6.1: Schematic representation of a transport device.

scattering region, through which the electric current has to be found. This general setup is depicted in fig. (6.1).

What we want to quantify at the end, is the amount of electrons passing through the sample, and relate it to the potential gradient (bias) present in the system. We define the electronic current I as [50]

$$I = \frac{e}{h} \int T(E)[f_L(E) - f_R(E)]dE, \quad (6.1)$$

where $f_{L/R}$ is the Fermi-Dirac distribution for the left/right electrode fixing the chemical potential on each side of the device. This is the Landauer formula for the current [48].

In this expression $T(E)$ is the so-called transmission function, which is defined as the probability for a particle to tunnel across the scattering region from one electrode to the other [51]. This is the entity to calculate in order to find the transport features in the system. To compute $T(E)$, we will define some operator that serves as a general and powerful tool to find the transmission and other quantities of interest, the well-known Green's functions.

In a very formal way, a Green's function (GF) G is defined as the inverse for the operator $[EI - H]$, that is $[EI - H]G = \mathbf{1}$, where $\mathbf{1}$ is the identity operator [49]. As such, GFs comprise information of the energy spectra of a system and have the advantage that can give response of the system to external perturbations in a very direct way [52].

The starting point to calculate the transmission function, will be to find the GF for the previously presented device in fig. (6.1). For this we need the Hamiltonian of the complete system which is given by [53]

$$H = \begin{pmatrix} H_L & V_{LC} & 0 \\ V_{CL} & H_C & V_{CR} \\ 0 & V_{RC} & H_R \end{pmatrix}, \quad (6.2)$$

where H_L , H_C and H_R are the matrix Hamiltonians of the left electrode, the central region and the right electrode respectively. Off-diagonal terms V_{CL} and V_{RC} (and conjugates) represent the coupling of the scattering zone to the electrodes which hold

$$V_{CL} = V_{LC}^\dagger, V_{CR} = V_{RC}^\dagger. \quad (6.3)$$

Now applying the GF definition

$$[EI - H]G = I, \quad (6.4)$$

to the matrix Hamiltonian in eq. (6.2) we obtain

$$\begin{pmatrix} E - H_L & -V_{LC} & 0 \\ -V_{LC}^\dagger & E - H_C & -V_{RC}^\dagger \\ 0 & -V_{RC} & E - H_R \end{pmatrix} \begin{pmatrix} G_L & G_{LC} & 0 \\ G_{CL} & G_C & G_{CR} \\ 0 & G_{RC} & G_R \end{pmatrix} = I. \quad (6.5)$$

The GF of interest is G_C where the spectral information of the central region is contained. We form the system of equations

$$\begin{aligned} (E - H_L)G_{LC} - V_{LC}G_C &= 0, \\ -V_{LC}^\dagger G_{LC} + (E - H_C)G_C - V_{RC}^\dagger G_{RC} &= I, \\ -V_{RC}G_C + (E - H_R)G_{RC} &= 0. \end{aligned} \quad (6.6)$$

Solving for G_C we obtain

$$(E - H_C - \Sigma)G_C = I,$$

where

$$\Sigma = V_{LC}^\dagger (E - H_L)^{-1} V_{LC} + V_{RC}^\dagger (E - H_R)^{-1} V_{RC}, \quad (6.7)$$

is defined as the electrode self-energy [53]. Therefore

$$G_C = [E - H_C - \Sigma]^{-1}. \quad (6.8)$$

It is necessary to define a function, called a level width function Γ as [49]

$$\Gamma = i(\Sigma^R - \Sigma^A). \quad (6.9)$$

Here Σ^R, Σ^A are the causal and anti-causal self-energies, called *retarded* and *advanced* self-energies [48]. In these cases E is replaced by $E \rightarrow (E \pm i\eta)$, where the plus sign is for the retarded case and the minus sign for the advanced case.

In terms of these functions we can define the transmission $\tau(E)$ for the central region in the form (see [49] for a derivation of this formula)

$$\tau(E) = Tr(\Gamma_L G_C^A \Gamma_R G_C^R), \quad (6.10)$$

where G^A and G^R are the *advanced* and *retarded* GFs defined in the same form as the advanced and retarded self-energies (E is replaced by $E \rightarrow (E \pm i\eta)$). This expression allows to find the transmission function in terms of GF and self-energies of the system. In actual systems the central issue is to calculate the central GFs in a computationally affordable manner [51]. This can be accomplished by a discretization procedure combined with a recursive method, in order to construct step by step the whole GF and self energies. This method will be explained in appendix II.B and is based on refs. [54, 55, 53].

6.1 Thermoelectric transport

One of the manifestations of electronic transport is the production of an electric current due to a temperature gradient present along the system. We name this response as a thermal current I_T and define it in within the Landauer formalism as [56]

$$I_T = \int (E - \mu + \Delta V) \tau(E) (f_L(E) - f_R(E)) dE. \quad (6.11)$$

Here μ is the chemical potential and ΔV is the potential bias.

This thermal current is related to diverse magnitudes that quantify how well a material is converting a thermal gradient into an electronic current flux. One is the electronic conductance G_e , defined as [57]

$$G_e = \frac{\Delta I}{\Delta V}, \quad (6.12)$$

in the limit $\Delta V \rightarrow 0$. Thermopower (Seebeck coefficient) S is defined as the induced voltage drop by the temperature gradient as the current tends to zero, such that

$$S = -\frac{\Delta V}{\Delta T} \quad \Delta I \rightarrow 0. \quad (6.13)$$

Also the thermal conductance κ_e is defined by

$$\kappa_e = \frac{\Delta I}{\Delta V}, \quad \Delta V \rightarrow 0 \quad (6.14)$$

All the above quantities can be expressed in an explicit form from the thermal current definition in eq. (6.11). Using an integral function defined as [58]

$$\mathfrak{L}_n(\mu, T) = \int_{-\infty}^{\infty} x^n \frac{e^n}{(e^x + 1)^2} \tau(x, \mu, T) dx. \quad (6.15)$$

This function allows to define all previous thermoelectric magnitudes in a compact form given by

$$\begin{aligned} G_e &= \frac{e}{h} \mathfrak{L}_0, \\ S &= -\frac{k_B}{e} \frac{\mathfrak{L}_1}{\mathfrak{L}_0}, \\ \kappa_e &= \frac{k_B^2}{h} T \left[\mathfrak{L}_2 - \frac{(\mathfrak{L}_1)^2}{\mathfrak{L}_0} \right]. \end{aligned} \quad (6.16)$$

Additionally a figure of merit denoted as ZT, can also be defined to study the efficiency of the material as [59]

$$ZT = \frac{G_e S^2 T}{\kappa}, \quad (6.17)$$

where $\kappa = \kappa_e + \kappa_{ph}$ is the total thermal conductance composed of electronic thermal conductance κ_e and the lattice thermal conductance κ_{ph} .

We apply these definitions to study thermoelectric performance of pentagraphene nanostructures, taking into account a particular geometry configuration. We will present in the results section a study of all thermoelectric magnitudes, numerically calculated by the recursive method.

Chapter 7

Topological phases

7.1 Introduction

Topological phases are nowadays the focus of great interest, both from the fundamental and applied point of view due to the new physics that they entail, which is changing paradigms in condensed matter physics. In this sense, the discovery of topologically nontrivial phases have been a widely discussed topic over the last decades, which started with the pioneering work of Thouless *et al.* [60], and the quantum Hall effects -integer and fractional [61, 62, 63], evolving in a robust branch of physics at present time. The research interest got revitalized after the discovery of a new Hall phase, called the *Quantum Spin Hall Effect* (QSHE) in 2005 [64, 65]. This new state of matter put spin-orbit coupling (SOC) and symmetry-protected topological states at the spotlight as a source of robust phenomena related to edge physics.

Hall effects are the most studied examples of non-trivial topology in a solid state system. The first inkling of these states dates from 1980 where a quantum version of the classical Hall effect was first observed by von Klitzing [66]. In this setting, a two-dimensional electron gas was exposed to a strong external magnetic field producing a quantized transverse conductance due to the formation of Landau levels at the sample's bulk [62]. After this experimental breakthrough, materials with intrinsic magnetism, such as ferromagnetism or antiferromagnetism, were found to present a quantum response in transport magnitudes, the so-called *quantum anomalous Hall effect* (QAHE) [67]. On the theoretical side, Haldane in 1988 proposed a related model for a honeycomb lattice where QAHE arises due to a built-in local magnetic flux in the system, yielding no net magnetic flux [68].

After these initial stages, other approaches and states were studied, such as intrinsic and extrinsic contributions to QAHE [69] and fractional quantum Hall effect with composite fermions [61]. However, as previously said, it was QSHE that propelled topology into the realm of mainstream solid state physics, the most conspicuous being the Kane and Mele model for the QSH state for graphene [70]. Subsequent theoretical works, such as Bernevig *et al.* [71]

and Fu *et al.* [72], paved the road to the experimental realization of this new phase at laboratory. This was accomplished in 2007 by Molenkamp's group [73] and afterwards by others [74, 75]. These corroborations attracted the attention of the community and the QSHE became soon a main actor in frontier condensed matter science. As such, a generalization of QSHE to three-dimensional systems and also to arbitrary dimensions was settled [76, 77, 78], giving birth to the concept of topological insulators (TI).

Topological insulators comprise a range of systems, in d dimensions, for which we have an insulating bulk band structure with a full gap, but with a gapless boundary, presenting surface or edge states [79]. These boundary states are very robust against perturbations applied to the system [80], and present a promising stage for exciting applications such as quantum computation [81], and spintronics [82, 83] among others.

At the time of the first stage of exploration, it was believed that a full gap in the energy band structure was a mandatory condition for a material being topologically non-trivial [79]. It did not take long to understand that this condition was too restrictive and indeed, gapless topological phases are also possible and stable *per se*.

Murakami [84] and Volovik [29] were who figured out that at the critical point in a normal-insulator-TI phase transition, non-trivial gapless phases could arise, under some explicit symmetry constraints. After that, some generalizations of this seminal result complemented this vision and gapless topological phases started to be a subject of study on their own [85]. Although gapless phases are well understood in general, the presence of topological boundary states open new lanes to explore how ubiquitous topology is within solid state systems.

These phases are known today as nodal states or topological (semi)-metals, and are the subject of intense research, both theoretically and experimentally [86, 87, 88, 89, 90]. Together with topological insulators topological (semi)-metals span a great group of non-trivial phases of matter. Nevertheless, despite the great amount of synthesized compounds up to now, only a little fraction are known to be topologically non-trivial [91]. It is believed that this percentage is much more significant, and there is a immense current effort in mapping all possible crystal structures and space groups, with the aim to find new topological phases of matter in real materials. On the other hand, there have been many proposals of non-trivial phases in new materials by means of first-principles calculations [92, 93, 94], which guide experimental research and poses new challenges in this field. A set of these new materials, which are composed of functionalized forms of penta-graphene [4] (or other pentagonal lattices [95]), are the so called *pentagonal materials* (or *penta-materials*), and are the subject of this thesis. This new class of materials is attracting attention due to the non-trivial behavior of their space group connectivity, being candidates for many interesting future applications.

7.2 General description of topological phases

7.2.1 Topological insulators

Insulating phases in crystals have varied properties depending on their gap magnitude and local form of conduction and valence bands. Even while a bulk band gap is present in all the systems in this material class, surface physics can be very different from insulator to insulator. In this way a distinctive subclass emerges in which surface states have some robust qualities against external perturbations. Materials with this special boundary physics are named as topological insulators [79].

Topological insulators come in different kinds and a comprehensive description of all of them is beyond our scope. We only describe very broad families of TIs, focusing only on its main properties in order to be identified in the systems we want to study.

As was mentioned above, TIs derive from QSH systems, and as such inherit some of their properties, such as quantized response of conductivity [70, 82]. These phases can be divided according to the symmetries that protect the non-trivial state. Among them it stands time-reversal symmetry (TRS). As $t \rightarrow -t$ some systems stay invariant and others do not. This invariance splits topological phases in two broad classes. If a system is time-reversal invariant, then spin-orbit coupling can play an important role and we can describe it in terms of time-reversal invariant points in momentum space [72]. These TIs mainly present band inversion in their bulk band structure [96] and constitute a direct generalization of the QSH state. A subdivision that arises within this context is the distinction between strong and weak topological insulators [72]. This classification is valid in 3 dimensions and is related to the penetration and features of surface states. No further details will be important for our purposes, since we are only interested in the big class delineated by time reversal symmetry. Both types of TIs are categorized by topological invariants, which are indices that clearly differentiate between phases [64]. Topological invariants will be addressed later on in a descriptive formal context.

On the other side we have systems with time reversal symmetry breaking. In these cases a perturbation, like magnetic field or magnetic doping [96], allows to distinguish between t and $-t$ states. These systems are named *Chern insulators*, since they are a generalization of integer/anomalous quantum Hall state, which is classified by a topological invariant known as the Chern number [76]. Specific characteristics of this topological index will be exposed below.

A somehow related class of TIs, which is not substantially dependent on time reversal but uses it, are crystalline topological insulators, where topological non-trivial states are protected by a combination of antiunitary and lattice symmetries. This class of TI could arise in penta-materials, a work that is in progress at the time of writing this work.

Thus we have three rough classes for the TIs we are trying to find. Within each group, additional divisions exist that can discriminate between the different types of topological protection beyond time reversal symmetry.

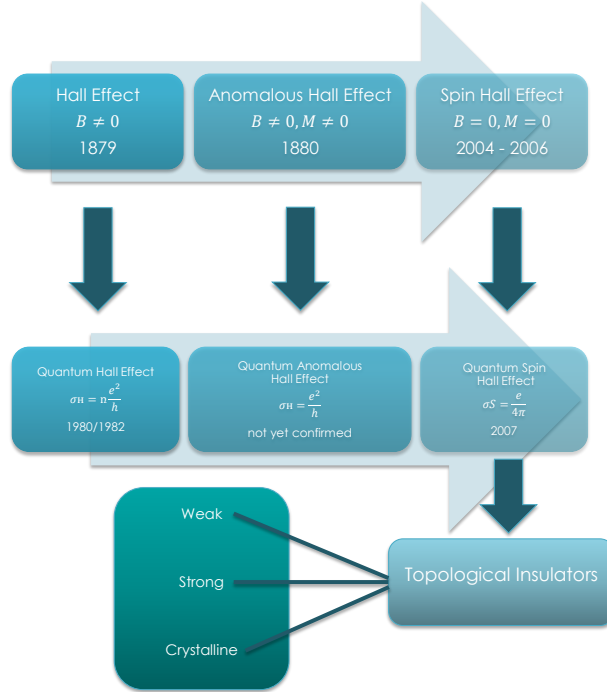


Figure 7.1: Scheme for the evolution of topological non-trivial phases up to TIs.

As a graphical compendium we present a summary chart in fig. (7.1) where we highlight the topological features we use in this work.

7.2.2 Topological (semi)-metals

Topological metals are phases where no full gap is present at the Fermi level, giving a gapless nontrivial phase. We can have compensated electron and hole pockets, which give a semi-metallic state, otherwise we have a nontrivial metallic phase.

In a very qualitative manner, interesting gapless phases present nodal crossings between two or more bands in momentum space, giving rise to a linear energy dispersion at the vicinity of the degeneracy point. The most iconic of these nodal points are Dirac cones, which represent four-fold degenerate crossings, as for example in graphene [97].

In general the most basic setting for the presence of Dirac cones requires

both time-reversal and inversion symmetry. Additional symmetries might be part of the system, in order to further protect the nodal point under perturbations. Dirac points have been found in several materials, both in 2-dimensions [98, 7, 99, 100] and 3-dimensions [85, 86, 87], and host many interesting physical properties, related with its effective relativistic energy dispersion, such as Klein tunneling, high electron mobility, among others [101].

As we explore further some low symmetry scenarios, we come to relax time reversal and/or inversion symmetry. This leads us to violate Kramers requirement for bands to be doubly degenerate throughout the entire Brillouin zone. As this happens, four-fold Dirac point becomes split into two-fold degenerated nodes, known as Weyl points, which represent an effective, low energy version of Weyl massless fermions, first encountered in the field of high energy physics [102]. As we remove this four-fold degeneracy, we have some possible resulting scenarios. If we break time-reversal symmetry without breaking inversion symmetry -as in noncentrosymmetric, nonmagnetic compounds- we end with at least two Weyl nodes. This is the minimum amount possible for any system [103]. On the other hand, relaxing inversion symmetry but keeping time reversal, we end with a minimum of four Weyl points due to time-reversal constraint [104]. If additional spatial symmetries are included in the space group, we can greatly multiply the amount of Weyl points in the BZ. Still, materials with few Weyl points (ideally two) are very desirable, with the aim to precisely isolate the associated physical phenomena. Such physical phenomena are related to the chiral character of Weyl points and in particular to the chiral anomaly effect, first discussed in quantum field theories for chiral particles [105]. In simple terms, the chiral anomaly is the production of an excess of particles with a particular chirality under the application of a combined electric and magnetic field [106]. Derived from the chiral anomaly, some exotic phenomena appear such as the so-called Fermi arcs and drum surface states as well as negative magnetoresistance [107].

Nodal points could be described with the Dirac equation for the low energy regime. Dirac nodes can be described by a Hamiltonian given by [102]

$$H = v\mathbf{p} \cdot \boldsymbol{\gamma} + mv\gamma_0, \quad (7.1)$$

where m is the mass of particles and v is the effective Fermi velocity. $\boldsymbol{\gamma} = (\gamma_0, \boldsymbol{\gamma})$ are Dirac gamma matrices given in terms of Pauli matrices σ_i as

$$\gamma_i = \begin{bmatrix} 0 & \sigma_i \\ \sigma_i & 0 \end{bmatrix}, \quad (7.2)$$

$$\gamma_0 = \begin{bmatrix} \sigma_0 & 0 \\ 0 & \sigma_0 \end{bmatrix}, \quad (7.3)$$

where σ_0 is the 2 by 2 identity matrix.

This Hamiltonian allows for touching points depending on the mass parameter m giving rise to a four-fold degeneracy due to time reversal and inversion symmetry.

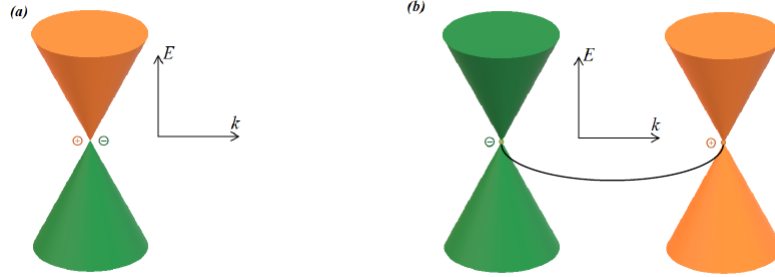


Figure 7.2: Point-like nodal phases. (a) Dirac node, (b) Weyl nodes pair with specified chirality.

Now, if we take m equal to zero we are left with a massless Hamiltonian

$$H = \pm v \mathbf{p} \cdot \boldsymbol{\sigma}. \quad (7.4)$$

We see immediately that this Hamiltonian defines two types of fermions with opposite chirality. Chiral particles have their spin locked to momentum as is observed in eq. (7.4). Thus we are left with two nodes at energy-momentum space that have energy eigenvalues given by $E = \pm vp$ and cross at $p = 0$. These nodes are known as Weyl nodes [108].

Deeper analysis could be done for these nodal systems, characterizing physical properties and related effects, but for our purposes it is sufficient this phenomenological description in order to understand that Dirac nodes need TRS and Weyl nodes lack either TRS or inversion symmetry.

Up to now we have concentrated in point-like nodes in BZ, but it is also possible to have some sets of degeneracies forming one-dimensional curves in momentum space, which are generally denoted as nodal-line systems [109, 110]. The location of degeneracy lines in momentum space depends on the space group symmetries. Also for a nodal line to be constant in energy over all BZ, spatial inversion must be a symmetry of the system [104], otherwise, we have a nodal-line over an energy window which might coexist with electron and hole pockets at the same energy range. The origin of nodal lines could be traced to either symmorphic and nonsymmorphic symmetries and in general are not very robust under symmetry breaking perturbations, as for example spin-orbit coupling [111]. There exist further line-like nodal phases such as nodal-link semi-metals [112], nodal-chain semi-metals [113], nodal-knot semi-metals [114] and hourglass semi-metals among others [115]. For the sake of this work, what we have to keep in mind is that nodal-line band touching happens very often in nonsymmorphic groups, with the addition of TRS. This is called the *stick-together* phenomena, well-known in the solid state literature [27]. This is a common effect in pentagonal materials, due to the space group components as we will explain in detail in upcoming sections.

A graphical depiction of these possible cases is presented in fig. (7.2). We see the change in degeneracy from Dirac nodes to Weyl nodes as well as the spin separation which become very important for chiral effects in Weyl materials.

In looking forward, we want to identify all mentioned topological phases in penta-materials. We scrutinize their symmetry character by group theoretical methods giving hints for the apparition of some insulator and/or gapless phases. Also, band structure calculations allow to identify nodal-like or insulating states more precisely. Then, the topological character of these phases is studied in detail and a global classification is achieved for the whole family of penta-materials. This procedure will be explained in the results section below.

Chapter 8

Theoretical tools to characterize a topological phase

Materials with topological features, TIs in particular, present a bulk structure that seems trivial if no surface information is added. Thus, a method to distinguish trivial phases from non-trivial ones is essential. Topological gapless phases as well need for a proper description of their topological characteristics, in order to differentiate robust edges states beyond the bulk nodal structure. In this section we present some theoretical frameworks that serve to describe and also predict in a unambiguously way if weak interacting materials possess some topologically non-trivial bands. With the aid of Wannier functions analysis, group theoretical methods, \mathbb{Z} invariants, band filling constraints and other tools, we apply several techniques where topological features are identified from the lattice symmetry and electronic band structure.

8.1 Topological Quantum Chemistry

In the task of material characterization and design it is always desirable to have some predictive procedure to discern whether a given band structure has topological attributes or not. In the toolkit of topological characterization most of the gear is designed to classify phases, with the so-called topological invariants [64]. It was not until recent time that a constructive method designed by Bradlyn *et al.* [91], dubbed *topological quantum chemistry* (TQC), came to fill this gap. We present here a detailed description of the line of work and its most prominent and basic fundamentals.

The main idea of this framework is to use the well-known result that there exists a dual map between properties in real space and momentum space. Namely, a global property in one space is related to a local property at the other [22]. As it was recognized, topological properties are global in momentum space, since they are related to band connectivity over the whole BZ. This property is translated to a local orbital description in real space. The impossibility to establish this map, that is to say, if a given group of bands cannot

be modeled by a set of localized Wannier functions, is a clear indicative of non-trivial topology for a subset of these group of bands [116].

The main target of TQC is to classify all the possible bands connectivities for a given double space group. This was done with the aid of graph-theoretical tools to map connectivities in band structures to multipartite graphs that can be analyzed with appropriate reduction algorithms [117]. However, for this thesis the emphasis is located in the subsequent procedure developed once the connectivity information is available. The procedure heavily depends in several concepts that we expose in what follows.

In first place, we need a local description in real space in order to characterize the material. As we already mentioned, Wannier functions are the most useful basis for the local description of the direct lattice. It is worth to mention that this basis could coincide with atomic sites or not, and could be composed of atomic orbitals or not [118]. The important ingredient is that we must be in knowledge of the orbital composition for the bands within the energy range we are interested in. This is important because not all bands in a material have to be analyzed in order to find if a topological property is present or not [91].

In addition, the symmetry operations that leave the crystal structure invariant in real space must be included. The set of these operations form a group structure, the so called space group G of the material. An element $g \in G$ acting in real space in local coordinates as $\mathbf{r} \rightarrow R\mathbf{r} + \mathbf{v}$ is denoted as $\{R|\mathbf{v}\}$. If we now denote \mathbf{q} to be a position in the unit cell, that can be occupied by an atom or not, we have the following (for the rest of this section, we heavily rely on Ref. [119])

Definition (stabilizer group).- The set of symmetry operations $g \in G$ that leave the site \mathbf{q} fixed is called the stabilizer group or site-symmetry group of \mathbf{q} , and is denoted by $G_{\mathbf{q}} = \{g | g\mathbf{q} = \mathbf{q}\} \subset G$. It is worth to mention that a site-symmetry group is always isomorphic to a crystallographic point group.

With this structure at hand we add the next

Definition (Wyckoff position).- Any two sites whose site-symmetry groups are conjugate are said to lie in the same *Wyckoff position*. Given a site in the Wyckoff position, the number of sites in its orbit that lie in a single unit cell defines the multiplicity of the position.

Wyckoff positions (WPs) are very important sites within a unit cell, since they condensate the most symmetric places in a solid. A derived concept from site-symmetry groups and WPs is the following

Definition (maximal site-symmetry group).- A site-symmetry group is non-maximal if there exists a finite group $H \neq G_{\mathbf{q}}$, such that $G_{\mathbf{q}} \subset H \subset G$. A site symmetry group that is not non-maximal is maximal. A WP containing \mathbf{q} is maximal if the stabilizer group $G_{\mathbf{q}}$ is maximal.

Maximal site-symmetry groups play a central role in the mapping to reciprocal space and the labeling of bands, as we will show below.

Now that the needed group theoretical information is defined, we must impose some conditions on Wannier functions. First, suppose we have n_q orbitals on site \mathbf{q} , which belongs to a WP of multiplicity n . The wave functions of these orbitals transform under an n_q -dimensional representation ρ of the site-symmetry group G_q . This representation can be single-valued for spinless electrons or double-valued for spinful systems. Additionally, it can be reducible or irreducible in principle, although only irreducible representations are truly fundamental [25]. Further equivalent sites of \mathbf{q} , namely, the ones in the orbit of \mathbf{q} , transform under the conjugate representation defined by $\rho_\alpha(h) = \rho(g_\alpha^{-1}hg_\alpha)$ for each $h \in G_q$. As we mentioned, orbitals on site \mathbf{q} can be described by a set of Wannier functions (WFs) $W_{i\alpha}(\mathbf{r})$, where $i = 1, \dots, n_q$. These WF's are localized at site \mathbf{q} . For each $g \in G_q$, the functions transform as

$$gW_{i1}(\mathbf{r}) = [\rho(g)]_{ji}W_{j1}(\mathbf{r}). \quad (8.1)$$

WFs localized on \mathbf{q}_α , the orbit of \mathbf{q} within the same unit cell, are defined by $W_{i\alpha}(\mathbf{r}) = g_\alpha W_{i1}(\mathbf{r}) = W_{i1}(g_\alpha^{-1}\mathbf{r})$, where $\alpha = 1, \dots, n$ and n is the multiplicity of the WP.

Now all the ingredients for real space description are set. In what follows we have to translate this information to momentum space. The step to do this is to define the Fourier transformed WF's as

$$a_{i\alpha}(\mathbf{k}, \mathbf{r}) = \sum_{\mu} e^{i\mathbf{k}\cdot\mathbf{t}_\mu} W_{i\alpha}(\mathbf{r} - \mathbf{t}_\mu), \quad (8.2)$$

where \mathbf{t}_μ is a lattice translation.

This transformation exchanges the infinite $n \times n_q \times N$ -dimensional ($N \rightarrow \infty$) basis, for a finite $n \times n_q$ basis for each of the N \mathbf{k} 's in the first BZ, corresponding to $n \times n_q$ energy bands. The natural procedure is to define the representation for the transformation of these $a_{i\alpha}$ functions induced by representation ρ in real space. This can be defined by

Definition (band representation).- The *band representation* ρ_G , induced from the n_q -dimensional representation ρ of the site-symmetry group G_q of a particular point \mathbf{q} whose orbit contains the sites $\{\mathbf{q}_\alpha = g_\alpha\mathbf{q}\}$ in the unit cell, is defined by the action

$$[\rho_G(h)a]_{i\alpha}(\mathbf{k}, \mathbf{r}) = e^{-i(R\mathbf{k})\cdot\mathbf{t}_{\beta\alpha}} \sum_{i'=1}^{n_q} \rho_{i'i}(g_\beta^{-1}\{E|\mathbf{t}_{\beta\alpha}\}hg_\alpha)a_{i'\beta}(R\mathbf{k}, \mathbf{r}), \quad (8.3)$$

for each $h = \{R|\mathbf{v}\} \in G$, where for each choice of α the index β is determined by the unique coset decomposition of G given by

$$G = \bigcup_{\alpha=1}^n g_\alpha(G_q \times \mathbb{Z}^3), \quad (8.4)$$

where \mathbb{Z}^3 is the group of Bravais lattice translations and \ltimes denotes a semi-direct product. This coset decomposition contains hg_α expressed as

$$hg_\alpha = \{E|\mathbf{t}_{\beta\alpha}\}g_\beta g, \quad (8.5)$$

for some $g \in G_q$. g_β is some coset representative and $\mathbf{t}_{\beta\alpha}$ is a lattice vector.

The matrix form of $\rho_G(h)$ consists of infinitely many $(n \cdot n_q) \times (n \cdot n_q)$ blocks. Each block is labeled by a pair $(\mathbf{k}', \mathbf{k})$, where \mathbf{k}' is a row index and \mathbf{k} is a column index. For each $h = \{R|\mathbf{v}\} \in G$ and each set of columns corresponding to $\rho_G(h)$, there is exactly one nonzero block, which corresponds to $\mathbf{k}' = R\mathbf{k}$. We denote this block by $\rho_G^{\mathbf{k}}(h)$, whose matrix elements are given by

$$\rho_G^{\mathbf{k}}(h)_{j\beta, i\alpha} = e^{-i(R\mathbf{k}) \cdot \mathbf{t}_{\beta\alpha}} \rho_{ji}(g_\beta^{-1} \{E|\mathbf{t}_{\beta\alpha}\} hg_\alpha). \quad (8.6)$$

The full set of matrices $\rho_G^{\mathbf{k}}(h)$, for each \mathbf{k} in the first BZ contains all of the nonzero elements of $\rho_G(h)$ and thus *completely determine the band representation*.

As we have induced a momentum space representation for the whole BZ with ρ_G , we can project this representation at special points within the BZ with a subduction procedure [91]. For each \mathbf{k} in the first BZ, the little group of \mathbf{k} , $G_{\mathbf{k}}$, is defined by $G_{\mathbf{k}} = \{h = \{R|\mathbf{v}\} | R\mathbf{k} = \mathbf{k}, h \in G\}$. Now the set $\{\rho_G^{\mathbf{k}}(h) | h \in G_{\mathbf{k}}\}$ furnishes an $(n \cdot n_q) \times (n \cdot n_q)$ representation of $G_{\mathbf{k}}$, whose matrix representation is given by eq. (8.6). This representation is denoted by $\rho_G \downarrow G_{\mathbf{k}}$. The characters of $\rho_G \downarrow G_{\mathbf{k}}$ are given by

$$\chi_G^{\mathbf{k}}(h) = \sum_{\alpha} e^{-i(R\mathbf{k}) \cdot \mathbf{t}_{\alpha\alpha}} \tilde{\chi}[\rho(g_\alpha^{-1} \{E|-\mathbf{t}_{\alpha\alpha}\} hg_\alpha)], \quad (8.7)$$

where $h \in G_{\mathbf{k}}$ and

$$\tilde{\chi}[\rho(g)] = \begin{cases} \chi[\rho(g)] & \text{if } g \in G_q \\ 0 & \text{if } g \notin G_q \end{cases}. \quad (8.8)$$

Thus, energy bands in reciprocal space inherits their properties from the direct-space orbitals on WPs in the unit cell. Induced representations presented before are not restricted in the sense of reducibility. However, there exists a special type of band representation which can be defined by

Definition (elementary band representation).- A band representation is called *composite* if it is equivalent to the direct sum of other band representations. A band representation that is not composite is called *elementary*.

By definition, all elementary band representations (EBRs) admit a description in terms of localized WFs, as they are induced from the representation of some site-symmetry group G_q . Two important remarks follow, noting that

$$(\rho_1 \oplus \rho_2) \uparrow G = (\rho_1 \uparrow G) \oplus (\rho_2 \uparrow G). \quad (8.9)$$

From this it can be deduced that

1. reducible representations of G_q induce composite band representations and
2. all EBRs can be induced from irreducible representations of the maximal site-symmetry groups.

This implies that maximal WPs are the principal source of EBRs [120].

There are some exceptions to this rule, that is to say, cases where an irreducible representation (irrep) of the site-symmetry group of a maximal WP induces a composite band representation. This can happen because the decomposition of an infinite dimensional representation into elementary representations is not necessarily unique [121]. A list of exceptions is presented in tables III and IV in [119].

So far, all the analysis has been reduced to the computation of EBRs induced from maximal site-symmetry groups. These EBRs allow to define a criterion for a set of bands to be topological. This can be expressed as the following

Definition (topological bands).- A set of bands is in the *atomic limit* of a space group if they can be induced from localized Wannier functions consistent with the crystalline symmetry of that space group. Otherwise they are *topological*.

In other words, *topological bands* correspond to a set of bands that *do not transform as a band representation*, even respecting all crystal symmetries in momentum space.

This central result can be complemented taking into account some general group theoretical aspects of momentum space. Namely, it is known that at each point in BZ, Bloch functions transform as a sum of irreps of the little group corresponding to that particular point. If we take different points or lines, specially high symmetry points and lines, their irreps are not independently defined. Lines emanating from high symmetry points are constrained to host irreps that form a subgroup of the little group for the high symmetry point [121]. Thus, there is a subduction procedure that limits the set of irreps for a set of bands and fixes all symmetry labels through the entire BZ. These limitations in connectivity are the so-called *compatibility relations* [25]. By construction, every band representation gives a solution to a compatibility relation. The important thing is that there can be solutions to compatibility relations that are not band representations. These relations are associated to the topological bands mentioned before. It is worth to mention that this is a band property, that is independent of the location of the Fermi level [119].

An exceptional case can occur in some instances. There exists a class of weak topological phases that in two and three dimensions inherit their topology from one-dimensional systems. This implies the possibility to describe those phases with a WF atomic limit [122]. The main difference is that this description in terms of localized orbitals does not reside on the atomic sites and thereby, it cannot be connected to any atomic-like limit without breaking a

symmetry or closing a gap. These phases are said to have an *obstructed atomic limit* [91].

Time reversal symmetry (TRS) is an important ingredient for the description of topological phases, as for example in topological insulators [123]. In general terms, TRS imposes some additional constraints in the form of allowed irreps of groups in real and momentum space. It is necessary to classify irreps invariance under TRS using the Frobenius-Schur indicator [26]. This could result in a irrep being real, quaternionic or complex. If the irrep is real and single-valued or quaternionic and double-valued, then it is time-reversal invariant. Otherwise it is not TR invariant on its own, and has to be combined with its conjugate partner to restore time reversal symmetry [119]. Thus, if we find an irrep that is not time-reversal invariant, we have to pair it with its complex conjugate. This new direct sum will become the allowed irreducible representation in the TRS case. All of these real, quaternionic or paired complex conjugates irreps are called *physical irreducible representations* [120]. As a straightforward implication of this last result, if TRS is present, EBRs will have to be physical EBR (pEBR) [91].

This exhausts the general formal framework of TQC. A more detailed description is available in the original papers [124, 119, 91, 117].

The EBRs characterization task has been accomplished recently [125] for double space groups, giving the access to the set of all EBRs for a given space group. This information is compiled at the Bilbao crystallographic server [28].

Now, as all possible EBRs for any space group can be obtained, it remains to find materials for which a group of bands cannot be described by this EBRs or pEBRs sitting near the Fermi level of the system.

Below we explain in more practical words the procedure to analyze if a given material may have a set of topologically nontrivial bands.

- First, is it desirable to have some electronic band structure calculation for the material of interest. This can be obtained as the output of an ab-initio code based on DFT.
- When the ab-initio bands are available, an orbital decomposition for the bands near the Fermi level is carried out, in order to set a low energy model. This last point is done by identifying which atoms in the unit cell contributes a given orbital.
- Once the contributions are available, the corresponding WPs for every atom in the low energy model must be identified.
- Find the site-symmetry group associated with every group of WPs in the model, either maximal and nonmaximal.
- For the orbitals in the model, find the corresponding irrep under which this group of orbitals transforms.
- Using this irrep in real space, induce the band representation in momentum space for the bands associated with the atomic limit. Classify it as

composite or elementary. If composite, find its elementary components. Take care of exceptions as listed in [119].

- Try the different possibilities of double groups with or without TRS.
- Identify whether some of the band representations are *decomposable* (disconnected). If this is the case, calculate the possible solutions for the compatibility relations through high symmetry lines and points in the BZ.
- Classify all the solutions in the last step as being (p)EBRs or not. If some of these solutions cannot be matched to a EBR or pEBR for the space group, then the associated group of bands is *topologically non trivial*.
- Classify all possible non-trivial phases in the model.

This straightforward process includes the usage of the Bilbao crystallographic server information as it will be explained in detail in the results section.

We can draw a flow diagram to depict in a more visual way the workflow to find topological phases within the TQC approach.

To conclude this TQC summary, we mention that it is also possible to work in a different manner. Namely, if a DFT calculation is given, it is possible to obtain the symmetry labeling for the bands of interest at high symmetry points and lines in the BZ. Armed with this information, compatibility relations are solved and can be directly compared to (p)EBRs for the space group of the material to identify their topological character. Both ways are complementary and necessary to achieve a fruitful design of topological materials.

8.2 Other methods to classify topological phases

TQC is a relatively recent method to discriminate topological phases based on energy band structure, although it is based on older results obtained by Zak [120, 121]. Here we briefly discuss other methods to classify topological phases.

In its most general form, the description of topological phases is carried by definition of topological invariants. A topological invariant is an index that naturally arises from a conjugation class decomposition of the configuration space for a given physical system [126]. Specifically, for a given Hamiltonian, the parameter space could be partitioned in disjoint classes for some physical property that allows to classify different phases. In condensed matter, we study the energy-momentum space with the aim to analyze its band connectivity. This band connectivity can be classified under some invariants depending on the symmetries that are present in the system [79].

8.2.1 Ten-fold way (K-theory)

The most universal classification framework for topological phases is based in K-theory [80]. The fundamentals of this theory are outside the scope of this

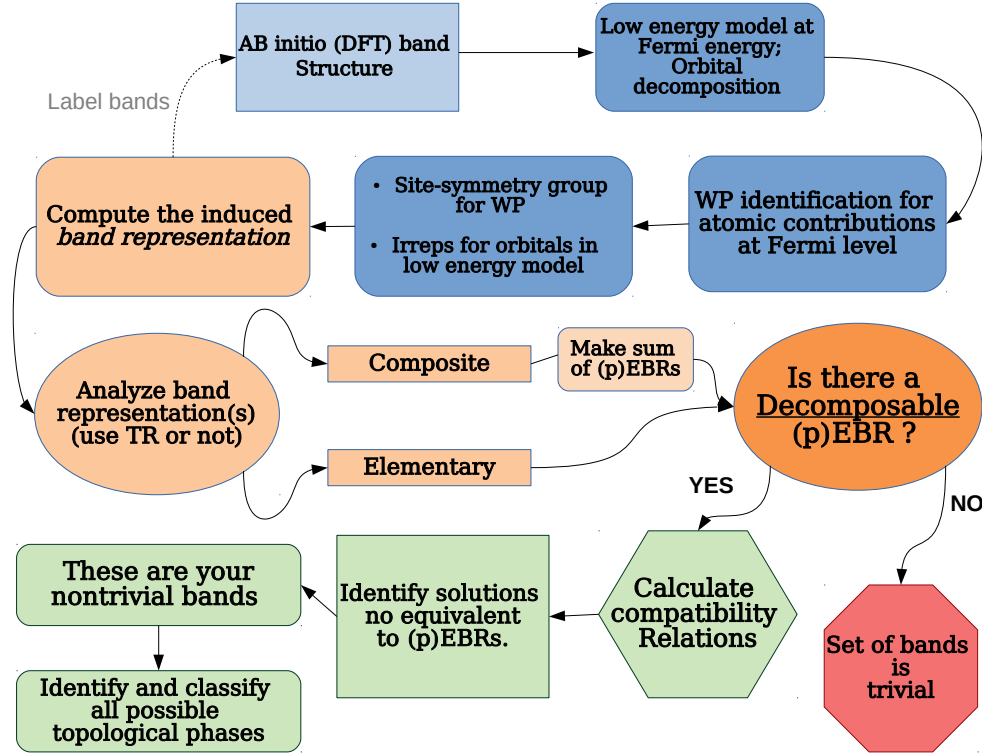


Figure 8.1: Topological quantum chemistry workflow diagram. The starting point is the ab initio calculation at the top.

thesis (interested readers can consult [127, 128, 129, 130]), thus we only go through a *how to use* description of symmetry classifications.

We start by pointing out that fermionic systems are distinguished based on three antiunitary symmetries: Time-reversal symmetry T , particle-hole symmetry C and chiral symmetry S which have the following properties (all this section is based in [1])

$$\begin{aligned}
 THT^{-1} &= H, & T &= U_T K, & U_T U_T^* &= \pm 1, \\
 C^{-1}HC &= -H, & C &= U_C K, & U_C U_C^* &= \pm 1, \\
 S^{-1}HS &= -H, & S &= U_s, & U_T^2 &= 1.
 \end{aligned} \tag{8.10}$$

Chiral symmetry is defined as a composed symmetry, $U_S = U_T U_C$. This set of symmetries exhausts all possible nonunitary symmetries for a fermionic system (unitary symmetries only separate Hamiltonians in block diagonal form and do not enter in principle in this universal classification). Next ingredient to perform the classification is the dimension of real space d . Dimension is important because some topological invariants depend on the parity of d [128].

| Class | T | C | S | $\delta = 0$ | 1 | 2 | 3 | 4 | 5 | 6 | 7 |
|-------|---|---|---|----------------|----------------|----------------|----------------|----------------|----------------|----------------|----------------|
| A | 0 | 0 | 0 | \mathbb{Z} | 0 | \mathbb{Z} | 0 | \mathbb{Z} | 0 | \mathbb{Z} | 0 |
| AIII | 0 | 0 | 1 | 0 | \mathbb{Z} | 0 | \mathbb{Z} | 0 | \mathbb{Z} | 0 | \mathbb{Z} |
| AI | + | 0 | 0 | \mathbb{Z} | 0 | 0 | 0 | $2\mathbb{Z}$ | 0 | \mathbb{Z}_2 | \mathbb{Z}_2 |
| BDI | + | + | 1 | \mathbb{Z}_2 | \mathbb{Z} | 0 | 0 | 0 | $2\mathbb{Z}$ | 0 | \mathbb{Z}_2 |
| D | 0 | + | 0 | \mathbb{Z}_2 | \mathbb{Z}_2 | \mathbb{Z} | 0 | 0 | 0 | $2\mathbb{Z}$ | 0 |
| DIII | - | + | 1 | 0 | \mathbb{Z}_2 | \mathbb{Z}_2 | \mathbb{Z} | 0 | 0 | 0 | $2\mathbb{Z}$ |
| AII | - | 0 | 0 | $2\mathbb{Z}$ | 0 | \mathbb{Z}_2 | \mathbb{Z}_2 | \mathbb{Z} | 0 | 0 | 0 |
| CII | - | - | 1 | 0 | $2\mathbb{Z}$ | 0 | \mathbb{Z}_2 | \mathbb{Z}_2 | \mathbb{Z} | 0 | 0 |
| C | 0 | - | 0 | 0 | 0 | $2\mathbb{Z}$ | 0 | \mathbb{Z}_2 | \mathbb{Z}_2 | \mathbb{Z} | 0 |
| CI | + | - | 1 | 0 | 0 | 0 | $2\mathbb{Z}$ | 0 | \mathbb{Z}_2 | \mathbb{Z}_2 | \mathbb{Z} |

Table 8.1: Periodic table for strong topological insulators and topological superconductors. Adapted from [1].

The group of three symmetries presented can generate ten possible combinations, using triplets (t, c, s) , where t and c can have values $0, \pm 1$ and $s = 0, 1$. These are the strong symmetry classes for gapped fermion systems. Therefore, at exploring systems in different dimensions, K-theory answers whether it is possible to have a nontrivial phase in each case. In this way it yields the topological index that describes the topological states. This information is condensed in a *periodic table* for gapped systems, which includes topological insulators and also topological superconductors [128]. We present an adapted form in table (8.1).

First, take into account that there exists periodicity in the dimension d and repetition of the information of the table arises after $d = 8$ [1].

Note also that if a topological nontrivial phase does not exist, zero is placed in the corresponding box. Otherwise an index is given. We briefly explain what those nonzero labels mean.

- \mathbb{Z} : This index represent an integer number. It is related to the Chern number (see appendix III.A for the properties of the Chern and related quantities).
- $2\mathbb{Z}$: This index indicates that only even integers are possible values.
- \mathbb{Z}_2 : This index states that only two integer values are needed to characterize different phases.

It is worth to mention that this classification is only for strong topological phases, which means that no lattice symmetry is considered in the process. Still, the classification of weak or crystalline topological phases is in principle based on this framework.

Following this successful description of gapped systems in terms of antiunitary symmetries, some years later an analogous description was developed for gapless fermionic systems. This classification was accomplished, by noting

| | | | | | | | | |
|----------|----------------|----------------|----------------|----------------|----------------|----------------|----------------|----------------|
| FS1 $p=$ | 8 | 1 | 2 | 3 | 4 | 5 | 6 | 7 |
| FS2 $p=$ | 2 | 3 | 4 | 5 | 6 | 7 | 8 | 1 |
| A | 0 | \mathbb{Z} | 0 | \mathbb{Z} | 0 | \mathbb{Z} | 0 | \mathbb{Z} |
| AIII | \mathbb{Z} | 0 | \mathbb{Z} | 0 | \mathbb{Z} | 0 | \mathbb{Z} | 0 |
| AI | 0 | 0 | 0 | $2\mathbb{Z}$ | 0 | \mathbb{Z}_2 | \mathbb{Z}_2 | \mathbb{Z} |
| BDI | \mathbb{Z} | 0 | 0 | 0 | $2\mathbb{Z}$ | 0 | \mathbb{Z}_2 | \mathbb{Z}_2 |
| D | \mathbb{Z}_2 | \mathbb{Z} | 0 | 0 | 0 | $2\mathbb{Z}$ | 0 | \mathbb{Z}_2 |
| DIII | \mathbb{Z}_2 | \mathbb{Z}_2 | \mathbb{Z} | 0 | 0 | 0 | $2\mathbb{Z}$ | 0 |
| AII | 0 | \mathbb{Z}_2 | \mathbb{Z}_2 | \mathbb{Z} | 0 | 0 | 0 | $2\mathbb{Z}$ |
| CII | $2\mathbb{Z}$ | 0 | \mathbb{Z}_2 | \mathbb{Z}_2 | \mathbb{Z} | 0 | 0 | 0 |
| C | 0 | $2\mathbb{Z}$ | 0 | \mathbb{Z}_2 | \mathbb{Z}_2 | \mathbb{Z} | 0 | 0 |
| CI | 0 | 0 | $2\mathbb{Z}$ | 0 | \mathbb{Z}_2 | \mathbb{Z}_2 | \mathbb{Z} | 0 |

Table 8.2: Periodic table for topological semimetals. $p = d - d_{FS}$ is the Fermi surface codimension where d_{FS} is the FS dimension. FS1 takes p at HSP and FS2 is for p out of HSP.

that in gapless systems an important role is played by the dimension of the Fermi surface in addition to the mentioned ingredients for the gapped case [131]. Inclusion of Fermi level information thus allowed for the construction of a periodic table for gapless fermionic systems, which closely parallels that of gapped systems. An adapted version is presented in table (8.2).

Topological invariants appearing in this table have the same meaning that those presented in the previous gapped case.

Other types of tables can be assembled by considering additional symmetries for the system. Including some kind of crystalline symmetry an extended periodic table is achieved. For example, in [132, 133] reflection symmetry is included.

This general classification will be used later to describe the materials under study to elucidate if some variant of the nontrivial phases can exist in these systems. We mix this with TQC results to achieve a better picture for the possible topological phases.

8.2.2 Band filling constraints and symmetry indicators

A related method, with less predictive power but still useful, is based on band filling and eigenvalues symmetry at high-symmetry points in the BZ [134]. The method establishes a relation between symmetry-enforced gapless phases and electron filling that deviates from particular values, that depends of the space group and time reversal symmetry and interactions [135]. Ref. [134] presents a complete table of the forms that have the insulator band fillings for each of the 230 space groups. This result imposes a necessary condition for a material to be gapless. However, this is not sufficient to achieve well-defined materials since additional stability information is needed, mainly extracted from experimental studies or in its defect, from first-principles calculations [136, 135].

Examining the table one can identify the possible values of band fillings (average number of electrons per primitive unit cell) that yield a band insulator structure. The unbalance of this relation opens the possibility to intentionally design nodal phases changing some elements in the material. As we will explain later, we use this result as a guideline to construct a family of materials based on a pentagonal lattice with non-insulating band filling.

8.3 Calculating topological invariants: Wannier charge centers

Up to now, we have described TQC as the central topic for topological phase prediction. We also have presented definitions of the most used topological invariants that allow a clear classification of different phases. In what follows, we will present a method to actually calculate some topological invariants that it is of high practical use, due to its low computational cost and simple implementation [122]. We are talking about *Wannier charge centers* and its associated evolution in momentum space, which gives information of the topological invariants in a system by graphical inspection [137, 138].

Wannier charge centers are based on the general concept of hybrid Wannier functions (HWF) [118]. HWF can be defined as a mixture between a Bloch function in momentum space and a real space Wannier function. As it is well-known, one-dimensional systems always admit a localized WF representation in real space, independently of its topological phase, a result that cannot be generalized to higher dimensions [116]. This idea induces to transform a general crystal wavefunction in terms of Bloch states, such that now, one of the degrees of freedom passes to real space as a coordinate variable. To fix the concept, consider a Bloch state in three dimensions $|\psi_{n\mathbf{k}}\rangle$ with its cell-periodic version expressed as $|u_{n\mathbf{k}}\rangle = e^{-i\mathbf{k}\cdot(\mathbf{r}-\mathbf{R})} |\psi_{n\mathbf{k}}\rangle$. Then, choosing z direction for the *wannierization* in three dimensions, the result is [122]

$$|W_{nl_z}(k_x, k_y)\rangle = \frac{1}{2\pi} \int dk_z e^{-i\mathbf{k}\cdot(\mathbf{r}-l_z c \hat{z})} |u_{n\mathbf{k}}\rangle, \quad (8.11)$$

where l_z is a layer index and c is the lattice constant along the \hat{z} direction. Equation (8.11) define hybrid Wannier functions in three dimensions. It is straightforward to define these functions in other dimensions.

Once HWF are settled, we define the central concept that reflects the topology of materials, i.e., Wannier charge centers (WCCs). For a given direction in real space they are defined as the expectation value of the position operator along that direction with respect to HWF at home unit cell $\mathbf{R} = 0$. Using the same direction as above, we express the WCC for z direction as [138]

$$\bar{z}(k_x, k_y) = \langle W_{n0} | z | W_{n0} \rangle \quad (8.12)$$

This WCC will form surfaces on the two-dimensional BZ (k_x, k_y) which are known as Wannier center sheets [122] (or lines in two-dimensional hybrid space).

Construction of WCCs can be carried by a parallel-transport procedure [116, 137]. This process is readily implemented in some computational codes [138, 139] and it is not the focus of our work.

We choose this approach of WCC analysis because it is based on purely bulk properties (Bloch and Wannier states) and is not very expensive computationally speaking. Also WCCs reflect same symmetries and topological features that a surface energy structure, respecting degeneracies and connectivities [118]. Thus WCCs allow for the calculation of topological invariants as Chern numbers and \mathbb{Z} invariants for a wide class of TIs and topological semimetals [122, 138].

We will illustrate the use of WCCs and its application to penta-materials in the results section and in a respective appendix (III.D), where an example of code input will be displayed.

Part II

Electronic, optical and transport properties of penta-graphene

Chapter 9

Results

9.1 Penta-graphene lattice geometry

As described by Zhang *et al.* [4], penta-graphene has a buckled lattice structure composed by non-planar carbon pentagons, shown in Fig. (9.1). The space group of this crystal lattice is $P_{42_1}m$ (#113) [25, 28], which is nonsymmorphic. The unit cell has six carbon atoms, highlighted with a black box in Fig. (9.1) (a). The buckled lattice structure of PG can also be described as composed of three layers, see Fig. (9.1) (b). Notice that two of the atoms in the unit cell, labeled C1, have coordination 4. They belong to the central layer, whereas the other four C2 atoms have coordination 3 and form the outer layers of PG. The difference in coordination number is obviously related to a different hybridization: C1 atoms have a sp^3 character, whereas C2 atoms are more sp^2 -like. This double hybridization is rooted in the buckled structure. The non-planarity has important effects in the mechanical properties [11] as with phononic transport as well and possibly interfere on spin-orbit effects.

Another important consequence of this lattice structure is its nonsymmorphic character, which provides important restrictions to degeneracies along high symmetry points and lines. In particular the symmetries that compose this space group are the following ¹

- C_2^z : a π rotation about a perpendicular axis with respect to the structure plane.
- S_4^+ : an improper rotation through $2\pi/n$ where in this case $n = 4$, which consists of a proper rotation by the former angle followed by a reflection in a horizontal plane of the system ($x - y$ plane in PG case).
- S_4^- : inverse improper rotation of the former operation.

¹Symmetry operations are presented in the standard notation $\{R|\mathbf{v}\}$ where R denotes a fixed point operation and \mathbf{v} stems for a translation, which could be a lattice vector translation or a fractional translation [25].

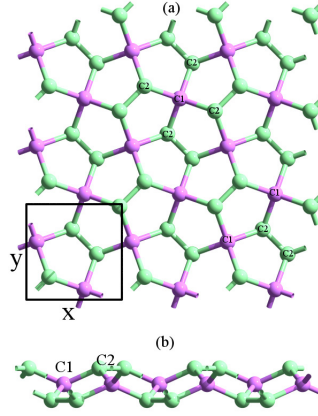


Figure 9.1: a) Top and (b) side views of the PG lattice. The unit cell comprising 6 carbon atoms is enclosed in a black square. Atoms with coordination number 4 are labeled as C1, those with coordination number 3 are labeled C2.

- $(C_2^x | \frac{1}{2} \frac{1}{2} 0)$: a π rotation about the x axis of the lattice along with a translation by the fractional vector $\mathbf{t} = (1/2a, 1/2a, 0)$, where a is the lattice structure constant.
- $(C_2^y | \frac{1}{2} \frac{1}{2} 0)$: a π rotation about the y axis of the lattice along with a translation by the fractional vector $\mathbf{t} = (1/2a, 1/2a, 0)$, where a is the lattice structure constant.
- $(m_{x-y} | \frac{1}{2} \frac{1}{2} 0)$: a mirror reflection with respect to a plane that bisects the positive x and y axes along with a translation by the fractional vector $\mathbf{t} = (1/2a, 1/2a, 0)$.
- $(m_{x-\bar{y}} | \frac{1}{2} \frac{1}{2} 0)$: a mirror reflection with respect to a plane that bisects the positive x axis and negative y axis along with a translation by the fractional vector $\mathbf{t} = (1/2a, 1/2a, 0)$.

Adding the identity operation I , these symmetry operations compose the space group of penta-graphene and of *buckled pentagonal materials* in general. Non-symmorphic operations comprise half of the total amount of operations, and thus will have great influence in the degeneracy panorama of these systems. Conjugation classes for this space group are given by

$$\left\{ (I), (C_2^z), (S_4^+, S_4^-), ((C_2^x | \frac{1}{2} \frac{1}{2} 0), (C_2^y | \frac{1}{2} \frac{1}{2} 0)), ((m_{x-y} | \frac{1}{2} \frac{1}{2} 0), (m_{x-\bar{y}} | \frac{1}{2} \frac{1}{2} 0)) \right\}$$

and are labeled by one of the elements of the class or by a representative tag to represent character tables (see appendix III.B).

These symmetry operations have to be enlarged for the inclusion of spin-orbit coupling, becoming double space groups (see Part III). For PG this effect

is rather weak and can be neglected, however spin-orbit coupling will be important later and double groups will be used in the general treatment of pentagonal materials. For the purpose of this part we will be using this lattice structure as the basis input for the TB model.

9.2 First-principles calculations

We employ the Density Functional Theory (DFT) approach, using the SIESTA ab-initio code [38], to calculate the opto-electronic properties of monolayer PG and penta-graphene nanoribbons (PGNR). In particular, we use for the exchange-correlation functional the generalized gradient approximation (GGA) of Perdew-Burke-Ernzerhof [140] instead of more expensive hybrid functionals [4], because the observed general trends in the electronic structure remain almost unaltered in both schemes, and only the magnitude of the band gap is changed [4, 16]. We use a double- ζ plus polarization basis set and norm-conserving pseudopotentials. The mesh cutoff was set to 150 Ry and the energy shift to 0.07 eV. The Brillouin zone was sampled with a $15 \times 15 \times 1$ Monkhorst-Pack grid for PG and a $10 \times 1 \times 1$ Monkhorst-Pack grid for PGNRs. A conjugate gradient self-consistent procedure was used to relax all structures with a maximal force tolerance per atom of 0.04 eV/Å. These sets of parameters assured a good energy convergence. In the case of PGNR, edges were passivated with hydrogen in order to saturate the dangling bonds.

For the optical absorption described below, we use a $201 \times 201 \times 1$ k -point grid for PG and a $201 \times 1 \times 1$ k -point grid for the PGNRs, with a 0.06 eV broadening for both structures. We also assume that the electromagnetic radiation is incident perpendicularly to the PG sheet, i.e., with the electric field \mathbf{E} polarization fixed in the xy plane.

9.3 Tight-binding model

We follow the Slater-Koster approach [41] for orthogonal tight-binding calculations with the aim of providing the simplest model with a good description of the electronic and optical properties. Our first concern is the orbital basis choice. Penta-graphene only has carbon atoms, so we take the usual basis selection of one s orbital and three p orbitals per atom. There are 6 atoms in the unit cell of PG; thus our basis for the S-K Hamiltonian has 24 orbitals. Note that previous parameterizations with fewer orbitals present a poor agreement with DFT bands; only consideration of the full sp^3 basis provides a reasonable accord [16]. Our goal is to find a set of parameters which gives not only a good depiction of the band structure, but also of the optical properties, so nanostructures based in PG, such as nanoribbons and nanotubes could be described within this approach in a computationally affordable manner.

Since we follow the Slater-Koster scheme we have to assign to the orbital integrals the corresponding parameters. For PG it is already known that a simple scaling of a graphene-based parameterization yields a qualitative agree-

ment, and a fit to DFT bands is needed to improve this description [16]. With this purpose we analyze the bonding structure and geometry of PG. As discussed in the previous section, in the 6-atom unit cell of PG there are two carbon atoms with coordination 4 and sp^3 hybridization, i.e., with four bonds each, labeled C1, and four carbon atoms with three bonds each, labeled C2, with sp^2 character. This partition leads us to treat each group of atoms separately with respect to the S-K parameterization. The basic idea is that these two groups of atoms not only have different nearest-neighbor (NN) distances, but also different hybridizations. From Fig. (9.1) we see that the first NNs for C1 atoms are four C2 atoms. In turn, the C2 atoms only have one NN, a C2 atom which is in the same layer. Therefore, we can assign a group of first NN parameters for each group. We parameterize the C1-C2 interaction with the S-K integrals $V_{ss\sigma}^{C1C2}, V_{sp\sigma}^{C1C2}, V_{pp\sigma}^{C1C2}, V_{pp\pi}^{C1C2}$, and the C2-C2 interaction with integrals $V_{ss\sigma}^{C2C2}, V_{sp\sigma}^{C2C2}, V_{pp\sigma}^{C2C2}, V_{pp\pi}^{C2C2}$. On the other hand, for the C2 atoms we already have included up to second NNs. We consider also the hopping between a C2 carbon atom in one of the external planes and another C2 atom from the opposite one, which we have labeled as C2' to distinguish it from the first NN C2-C2 pair. This interaction is indeed a third NN interaction, and we can assign to it the corresponding SK integrals $V_{ss\sigma}^{C2C2'}, V_{sp\sigma}^{C2C2'}, V_{pp\sigma}^{C2C2'}, V_{pp\pi}^{C2C2'}$.

This exhausts the basic interactions for our model. We have checked that considering the next NN for the C1 atoms, i.e., another C1-C2 coupling, does not improve appreciably our results, so in fact we have a geometrical cutoff that includes interactions up to distances equal or smaller than the 3rd NN interactions between C2 atoms.

In summary, we have twelve S-K hopping parameters with contributions up to first NN for the C1 atoms and up to third NN for the C2. Finally, we consider the onsite energies associated with each atom and orbital. Specifically, we assign four onsite energies, $E_s^{C1}, E_p^{C1}, E_s^{C2}, E_p^{C2}$ corresponding to s orbitals and p orbitals for each group of atoms respectively. This amounts to a total of sixteen S-K parameters in our model.

The bands are usually fitted at the high symmetry points and special lines, which are in principle the main contributions to the optical absorption. Such fitting is done with respect to the bands obtained within the DFT approach. However, we have verified that the four bands closer to the gap may have a very good agreement with the DFT bands, but without achieving a similarly acceptable description of the optical absorption.

We have found that there are local maxima and minima in the dispersion relations, especially in the valence band, which cannot be fitted with this reduced set of parameters. We have explored several parameterizations along these special lines, and despite obtaining very good fits to the conduction bands, all fail to give the shape of the valence bands, which are relevant to the fit of the optical spectrum. Since the optical properties depend on all the states over the Brillouin zone (BZ), not only over the special lines, we decided to perform a fit to the energy dispersion relation over the entire 2D BZ, with 8000 k points. However, this did not improve the optical absorption results obtained

by our initial method. Therefore, it is necessary to further correct the parameter set considering the optical absorption in order to describe optimally both, the electronic structure and the optical response. Details of our computational procedure are described in the additional parameterizations section below. The final values for the TB parameters are presented in Table 9.1.

| E_s^{C1} | | E_p^{C1} | | E_s^{C2} | | E_p^{C2} | |
|------------------------|-----------------------|------------------------|------------------------|------------------------|-----------------------|------------|--|
| -6.433 | | -4.311 | | -2.081 | | 6.506 | |
| $V_{ss\sigma}^{C1C2}$ | $V_{sp\sigma}^{C1C2}$ | $V_{pp\sigma}^{C1C2}$ | $V_{pp\pi}^{C1C2}$ | $V_{ss\sigma}^{C2C2}$ | $V_{sp\sigma}^{C2C2}$ | | |
| -3.555 | 2.246 | 3.903 | -0.262 | -11.731 | -10.017 | | |
| $V_{pp\sigma}^{C'2C2}$ | $V_{pp\pi}^{C'2C2}$ | $V_{ss\sigma}^{C'2C2}$ | $V_{sp\sigma}^{C'2C2}$ | $V_{pp\sigma}^{C'2C2}$ | $V_{pp\pi}^{C'2C2}$ | | |
| 15.490 | -1.762 | -2.504 | 1.080 | -3.247 | -0.921 | | |

Table 9.1: Slater-Koster tight-binding parameters (in eV) for PG.

9.4 Electronic properties of PG

In the left panel of fig. 9.2 we present the TB band structure obtained with the parameters given in table 9.1 along with the bands calculated using the SIESTA code for PG. It can be seen that there is a very good overall agreement between them. We have been able to reproduce the conduction band minimum along the Σ line, among other features.

As mentioned before, it is feasible to obtain an excellent fit to the four bands of interest, especially the conduction bands, with the same number of parameters, but failing to reproduce other valence bands at lower energy. In particular, the maxima and minima of the valence bands in the Σ direction cannot be reproduced with this model. This *wiggling* of the valence bands also appears in other low-symmetry points of the BZ inside the 2D region enclosed by the special symmetry lines. We have found that the appearance of local maxima and minima in the DFT calculation, specially in the valence bands, is the reason why the optical spectrum is not even qualitatively correct. We opted for a compromise solution, maintaining the overall agreement of the bands but without losing the description of the optical properties while keeping the same number of parameters.

Our election of tight-binding parameters can be supported with the orbital decomposition of the density of states (DOS) for monolayer PG, shown in the right panel of fig. 9.2. The DOS calculation was performed with SIESTA with a dedicated $251 \times 251 \times 1$ k-point grid for this particular calculation along with an energy broadening of 0.010 eV. The figure also shows the orbital decomposition of the DOS in s and p orbitals. As expected [16], these four bands mainly have a p character, more specifically p_z , albeit with a non-negligible contribution of the p_x and p_y orbitals, which are equivalent. In addition, we have identified

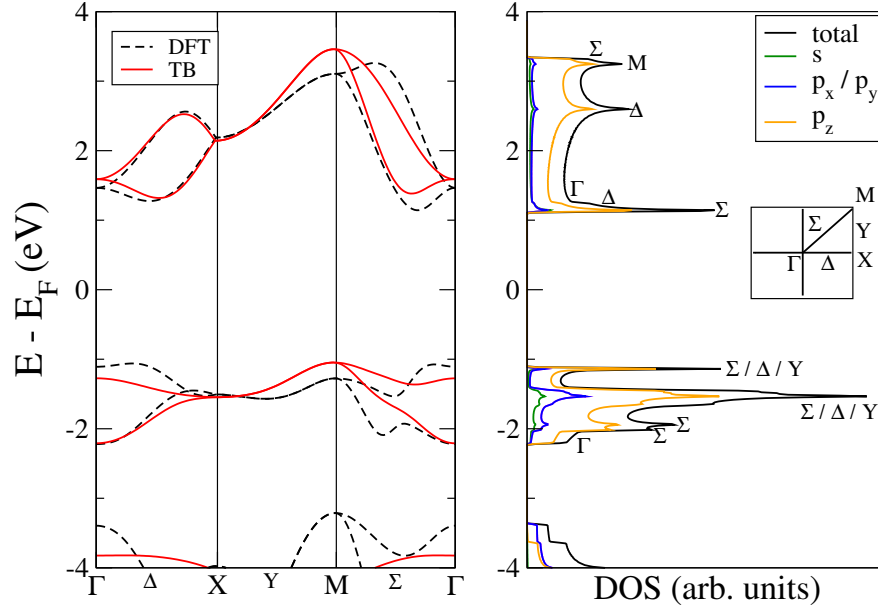


Figure 9.2: Left panel: PG energy band structures near the Fermi level calculated with DFT (black dotted lines) and tight-binding (red solid lines). Right panel: DFT-calculated penta-graphene total DOS (black solid line), and its decomposition in s -orbital (green), p_x/p_y -orbitals (blue) and p_z orbital (orange) projected DOS

the DOS peaks corresponding to high symmetry points and lines within the BZ, shown in the inset of the figure, with the aim to elucidate the symmetry of the BZ points with a high density of states. This can serve as a guide to understand the optical features of the material.

9.5 Optical properties of monolayer PG

As in the case of the electronic band structure, we compare the optical absorption coefficient computed within the DFT approach with that calculated with the tight-binding approximation. In this case we use the same k -space grid and broadening energy in both calculations, TB and DFT. The results are shown in fig. 9.4. There are three marked peaks in the low energy region of

the DFT optical spectrum. We have labeled them according to the symmetry of the relevant states, as in the DOS plot. The lowest peak (~ 2.45 eV), is due to transitions near the band gap; it is dominated by contributions from a region around the Δ line, where the conduction and valence band states have an energy difference ~ 2.5 eV. The next peak (~ 3 eV) has contributions from the Σ line across the BZ, where many transitions are allowed due to the low symmetry. The last and higher peak in this energy window (~ 3.8 eV), can be related to the Δ line, where we have several allowed transitions due to the low symmetry present in this line, similar to those from the Σ direction and the peak near 3 eV. Additionally, we have checked that the Γ point does not have a major weight in this peak; its height is due to other low-symmetry points involving the local maxima and minima of the valence bands. Additional symmetry analysis gives us another interesting property related to the optical response of PG. Due to the group of the wave vector at the high symmetry points X and M of the BZ, we obtain a selection rule that forbids transitions from the valence to the conduction band at these two points. This is because of the different parities of the irreducible representations that are coupled by the momentum operator, giving a direct product that does not contain the invariant irreducible representation of the group [27]. Moving away from these points, the restriction is relaxed; the shoulder at ~ 4 eV has contributions from the Σ and Y lines around M and neighboring low-symmetry points.

The TB parameterization reproduces the main features in the optical absorption spectrum, as shown in Fig. (9.4). The two higher energy peaks, at 3 and 3.8 eV, appear at the same energy; the lower peak is blue-shifted around 0.3 eV. However, the intensities are not well described by the TB model. The lower and higher energy peaks show an appreciable difference in intensity compared to the DFT result. The central peak does match the DFT intensity. The dip between ~ 2.5 eV and ~ 3 eV peak is substantially reduced. This is due to the fact that these two peaks stem from transitions involving the local maxima and minima of the valence bands, difficult to fit with this TB basis set. We would like to emphasize that our parameterization of the energy band structure, which uses the optical absorption as a criterion for its validity, manages to provide a remarkably good description of both features.

9.6 Additional parameterizations

As mentioned above, we have performed a systematic search for parameterizations that describe well the electronic structure near Fermi level for PG. This was accomplished by the model presented before and by some additional procedures that we explain here.

We started by performing a fit of the bands along the high symmetry lines. No constraints are imposed on the parameters and 8 bands are fitted by a least squares method. This yields a parameter set that we call TB1, given in Table

9.2. The corresponding bands are shown in fig. 9.3 in blue, along with the DFT bands, plotted as a reference. With this set we start a new fit of the parameters, now in a two-dimensional (2D) grid over the entire Brillouin zone. This is done incrementally: first we take a 2000 k -point grid to adjust the bands, and we increase successively to 4000 and 8000 k -points, which were enough to achieve convergence to the energy dispersion relations; see fig. 9.3 in magenta. With this set, that we call TB2 we start a manual correction procedure with the aim of describing the optical properties. With this purpose, we use the total DOS as a guide to elucidate the main contributions to the optical spectra.

It can be seen that both sets of parameters allow to obtain a good description of the four bands closer to the gap. In fact, the conduction bands are specially well described, presenting the minima along the ΓX and ΓM directions, as in SIESTA results. However, the valence bands are not so well described, particularly below -3 eV. Even the two highest valence bands are not well reproduced. Wiggling of the DFT valence bands produce contributions to the optical spectra that cannot be reproduced with these TB parameterizations, as it can be observed in fig. 9.4, where we present the absorption coefficient calculated with the sets TB1 and TB2, as well as with the SIESTA code. As discussed in the past section, we find that the optimal procedure is to correct the parameter set in order to attain the best agreement to the optical spectrum.

| E_s^{C1} | | E_p^{C1} | | E_s^{C2} | | E_p^{C2} | |
|-----------------------|-----------------------|------------------------|------------------------|------------------------|-----------------------|------------|--|
| -19.99 | | -6.423 | | -5.316 | | 7.223 | |
| $V_{ss\sigma}^{C1C2}$ | $V_{sp\sigma}^{C1C2}$ | $V_{pp\sigma}^{C1C2}$ | $V_{pp\pi}^{C1C2}$ | $V_{ss\sigma}^{C2C2}$ | $V_{sp\sigma}^{C2C2}$ | | |
| -8.143 | 4.593 | 3.924 | -0.162 | -11.787 | -7.348 | | |
| $V_{pp\sigma}^{C2C2}$ | $V_{pp\pi}^{C2C2}$ | $V_{ss\sigma}^{C'2C2}$ | $V_{sp\sigma}^{C'2C2}$ | $V_{pp\sigma}^{C'2C2}$ | $V_{pp\pi}^{C'2C2}$ | | |
| 11.207 | -2.832 | -2.478 | -0.037 | -4.058 | -0.722 | | |

Table 9.2: Set TB1 of Slater-Koster tight-binding parameters (in eV) for PG.

| E_s^{C1} | | E_p^{C1} | | E_s^{C2} | | E_p^{C2} | |
|-----------------------|-----------------------|------------------------|------------------------|------------------------|-----------------------|------------|--|
| -6.433 | | -4.311 | | -2.081 | | 7.006 | |
| $V_{ss\sigma}^{C1C2}$ | $V_{sp\sigma}^{C1C2}$ | $V_{pp\sigma}^{C1C2}$ | $V_{pp\pi}^{C1C2}$ | $V_{ss\sigma}^{C2C2}$ | $V_{sp\sigma}^{C2C2}$ | | |
| 16.589 | -1.862 | -2.504 | -1.080 | -3.447 | 0.921 | | |
| $V_{pp\sigma}^{C2C2}$ | $V_{pp\pi}^{C2C2}$ | $V_{ss\sigma}^{C'2C2}$ | $V_{sp\sigma}^{C'2C2}$ | $V_{pp\sigma}^{C'2C2}$ | $V_{pp\pi}^{C'2C2}$ | | |
| -3.555 | 2.246 | 3.903 | -0.262 | -11.731 | -10.017 | | |

Table 9.3: Set TB2 of Slater-Koster tight-binding parameters (in eV) for PG.

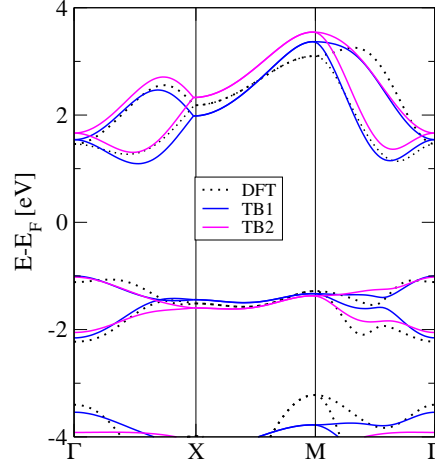


Figure 9.3: PG energy band structure near the Fermi level calculated with DFT (black dotted lines), and the two TB parameters sets, TB1 (blue lines) and TB2 (magenta lines).

9.7 Penta-graphene nanoribbons

In this section we present the band structures and optical absorption spectra of a particular type of penta-graphene nanoribbons (PGNRs) as a means to test our model in nanostructured systems. In particular, we choose PGNRs with sawtooth-like edges [141], shown in fig.9.5. The reason for this choice is that PGNRs with such edges are not magnetic [142, 143], so we can concentrate in the validity of the tight-binding parameterization focusing on size effects. PGNRs are labeled with the number of longitudinal chains across its width. For example, fig. 9.5 depicts a 11-PGNR. Obviously, the symmetry of PGNRs is reduced with respect to PG. Since nanoribbons have translation symmetry in only one direction, we have to resort to the so called rod groups to describe their symmetry. The PGNRs studied in this work belong to the rod group labeled $P112_1$ [144]. It has the identity transformation plus a C_2 rotation around the periodic axis of the ribbon combined with a glide plane translation by $1/2a$, where a is the lattice constant vector in the direction with translation symmetry.

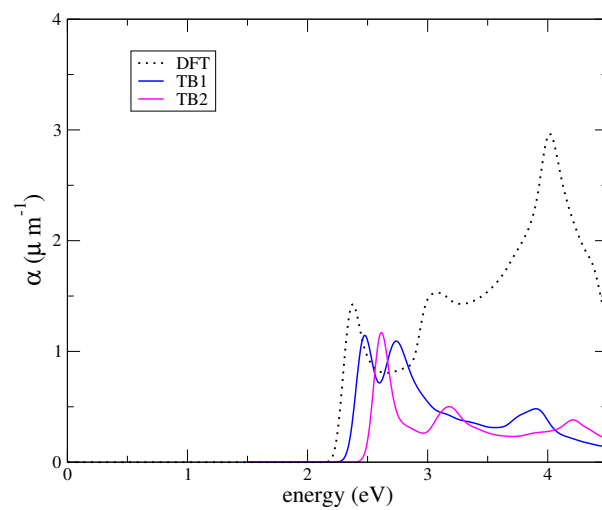


Figure 9.4: Optical absorption for PG calculated with DFT (black dotted lines) and with the two tight-binding parameterizations TB1 (blue lines) and TB2 (magenta lines).

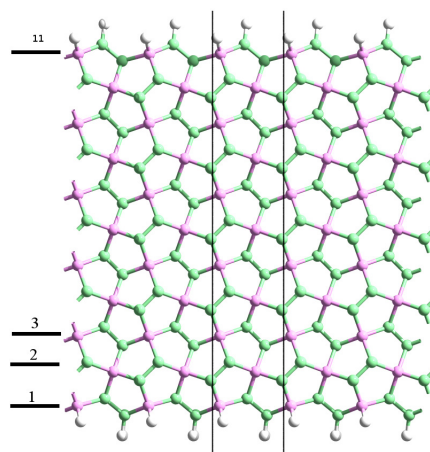


Figure 9.5: 11-PGNR lattice structure. The translational unit cell is marked between two black lines. The labeling based in longitudinal chains is herein illustrated.

9.7.1 Band structure of PGNRs

Ultra-narrow nanoribbons present strong lattice relaxation effects, so we focus on wider ribbons, for which such effects are not so important and can be described with a small modification of the hopping parameters at the edges. The translational unit cell employed for the calculations is marked with two black lines in fig. 9.5. We use the TB parameterization of monolayer PG and a hard wall boundary condition for the edges, which means that the dangling bonds of the edge atoms are modeled by hopping matrix elements set to zero. In fact, this is analogous to the inclusion of hydrogen atoms at the edges, but more economical from the computational viewpoint. Since these unsaturated orbitals produce deformations at the edge bonds, we change the corresponding hoppings, increasing their value in 10 % in order to mimic such geometrical changes.

Figure 9.6 shows the band structures calculated with SIESTA and TB for two particular nanoribbons, namely, 17-PGNR and 23-PGNR, respectively. The band structures obtained by both, the ab-initio and the TB method, show a good agreement. Most remarkably, the low-energy conduction subbands show the indirect minima appearing in the ΓX line. Valence subbands lack some of the fine details concerning some accidental degeneracies that occur along the aforementioned ΓX line. These differences can be easily understood, since the band structure of bulk PG did not reproduce accurately the valence bands of the DFT calculation. On the other hand, since the ribbons have a lower symmetry with respect to the bulk structure, we expect some decrease in the degeneracy at high symmetry points in the Brillouin zone. This can be seen at Γ and X , where subbands tend to avoid degeneracy in contrast to the case of the bulk. This is observed in both calculations, DFT and TB.

9.7.2 Optical absorption of PGNRs

We have additionally computed the optical absorption for nanoribbons with different widths, namely, 17-PGNR to 23-PGNR. In this case we consider that the electric field of the EM radiation oscillates along the nanoribbon axis. In order to make a comparison between both approaches and test the TB parameterization, we have also employed a first-principles method. The optical absorption is also computed employing eq. (5.13) using the same external electric field configuration, k -space grid and energy broadening in the TB calculation as in the DFT. The included nanoribbon subbands are those stemming from the bulk bands considered for the monolayer optical absorption.

Results for optical absorption spectra in both approaches are presented in fig. 9.7. For the sake of comparison, we restrict the spectra up to 4 eV, given that the DFT peak at this energy is not well reproduced in the TB calculation.

There is a very good overall agreement in the visible and near ultraviolet photon energy range in both, TB and DFT spectra, quantum size effects can be observed as smooth ripples in the spectra. In fact, as the width of the ribbon

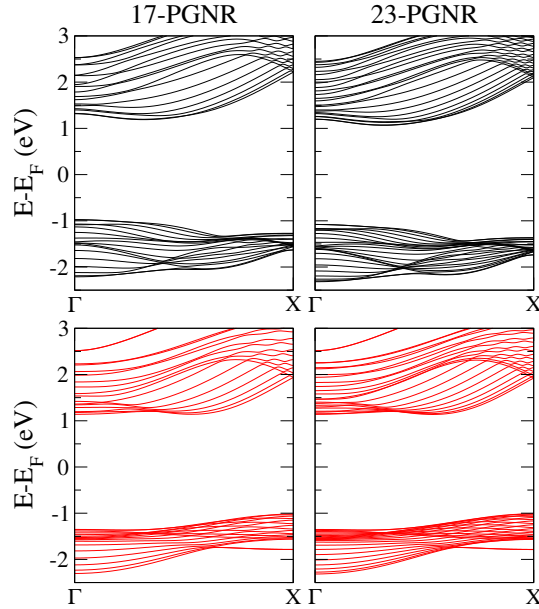


Figure 9.6: Energy band structures for 17-PGNR and 23-PGNR. Top panels (black lines) are computed with SIESTA; bottom panels (red lines) are the TB results.

increases, the features corresponding to the 2D peak at 3 eV emerge more clearly. In view of the validity of the TB parameterization, the description of the optical properties is quite good. In particular, the evolution of the low-energy peak with the width of the nanoribbon is correctly described.

□In summary, we have developed a tight-binding parameterization for pentagraphene that provides a very good description of the opto-electronics properties of this material, as it can be seen by comparing the tight-binding calculated magnitudes to the first-principles results. Our choice of parameters was guided by the existence of two types of hybridization in PG: we assigned different parameters to atoms with different hybridization, and set a geometric cutoff corresponding to third-nearest neighbor interactions for the C2 atoms. The validity of the basis and parameterization was substantiated by the orbital-resolved DFT calculated density of states of PG and by the agreement of the energy bands and optical spectrum calculated within the TB and the DFT approaches, respectively. This parameterization was also employed to model PG nanoribbons with non-magnetic edges, achieving a good description of the quantum-size effects and the recovery of bulk features with increasing widths. We additionally performed a symmetry analysis of the bands, identifying the space group structure of PG and elucidating the contributions of

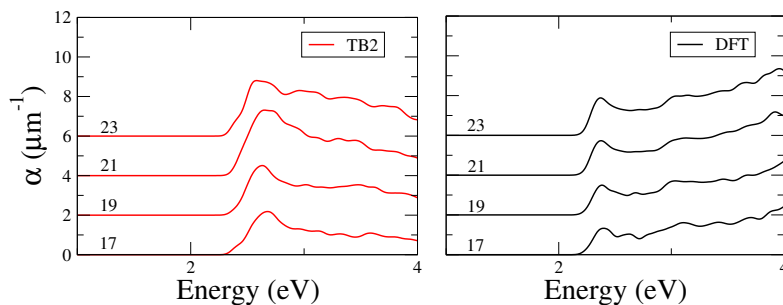


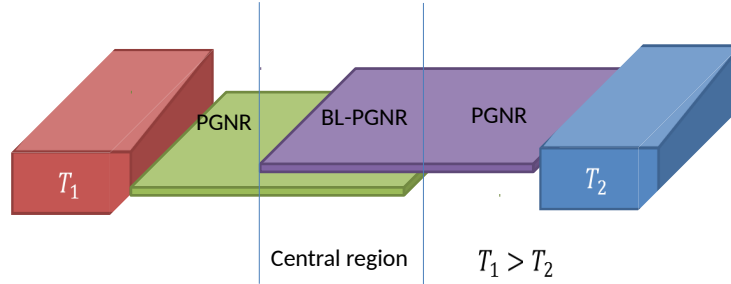
Figure 9.7: Optical absorption for 17- to 23-PGNRs calculated with (a) TB2; and (b) DFT (SIESTA). For the sake of clarity each curve is shifted a fixed amount.

different states to the prominent peaks of the optical spectra. Our parameterization can be of interest to model further physical properties of penta-graphene based nanostructures, for which a first-principles approach is computationally unaffordable. \square

9.8 Thermoelectric properties of penta-graphene

Thermoelectric physics is nowadays a very broad field with intense research efforts due to the implications it can have in energetic applications [59]. Discovering new materials with good thermal to electrical conversion ratio becomes thus highly desirable and useful for energy harvesting [145].

In this context, and following the growing interest for this type of thermoelectric materials, we analyzed the response of PGNR under a particularly convenient device configuration. The geometric disposition of the system is presented in the following diagram



The device consists of two electrodes composed in this case of penta-graphene nanoribbons, with temperature reservoirs kept at two different temperatures T_1 and T_2 respectively. This generates the temperature gradient across the central region where induced thermal current goes through. This central region is composed of a bilayer penta-graphene ribbon with the electrodes attaching only to one of the layers (irrespective of which one in principle).

The selection criterion for this particular setting was guided by the general principle that, in order to have a good thermoelectric material, the phononic contribution to thermal conductivity has to be minimized, while maintaining an acceptable electronic conductivity [56]. Thus, to reduce this conductivity within the central region, a physical cutoff barrier was designed in the form of a bilayer flake. This has demonstrated to decrease substantially the lattice thermal conductivity κ_{ph} in nanodevices [58].

For the thermoelectric analysis we have to calculate transport properties within the recursive GF approach outlined in the theoretical fundamentals part and in appendix II.B. This method uses a tight-binding model for the transport region and electrodes in order to compute the transmission function for the system [53].

We have already presented the results for monolayer PG nanoribbons in

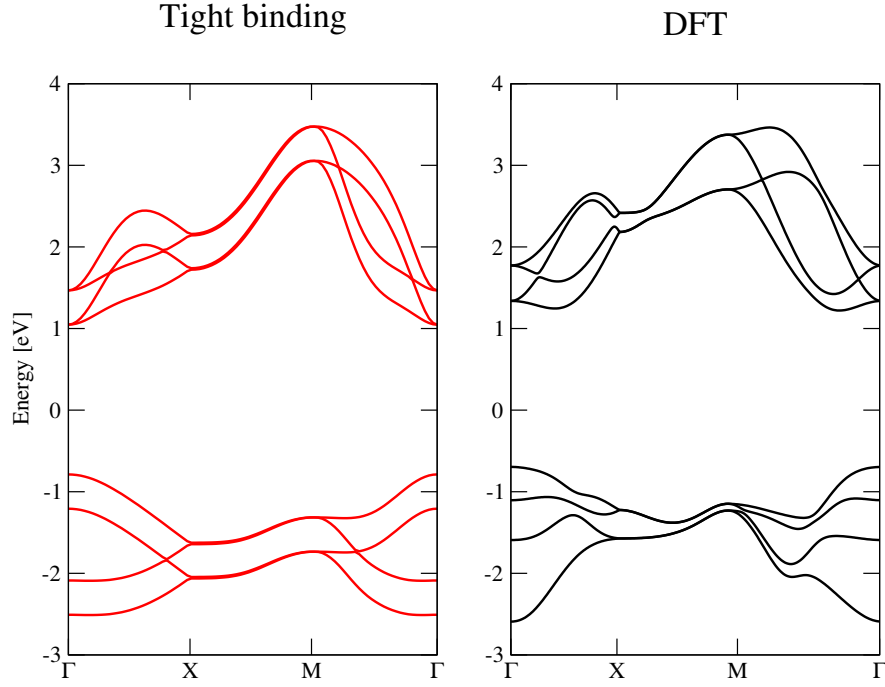


Figure 9.8: Band structure for bilayer penta-graphene in tight binding and DFT.

previous sections. So we will use this model for the electrode zones, where both electrodes are considered as equivalent. It is still needed a parameterization for the bilayer-PG NR at the central zone. We do this extending the tight-binding model for monolayer PG in the most straightforward way: by adding hopping parameters to represent the coupling between the two layers. We choose to add two new S-K parameters V_{B1} and V_{B2} , which denote the hopping between C1 to C1 atoms and C2 to C2 atoms at different layers, respectively.

We have adjusted these two free parameters to a DFT calculation of an infinite bilayer of PG. We present the band structure results for both DFT and TB in fig. 9.8.

The obtained S-K additional parameters for bilayer PG are presented in the table below

| $V_{B1}(eV)$ | $V_{B2}(eV)$ |
|--------------|--------------|
| 0.24 | -0.11 |

The rest of TB parameters, corresponding to intralayer hopping are the

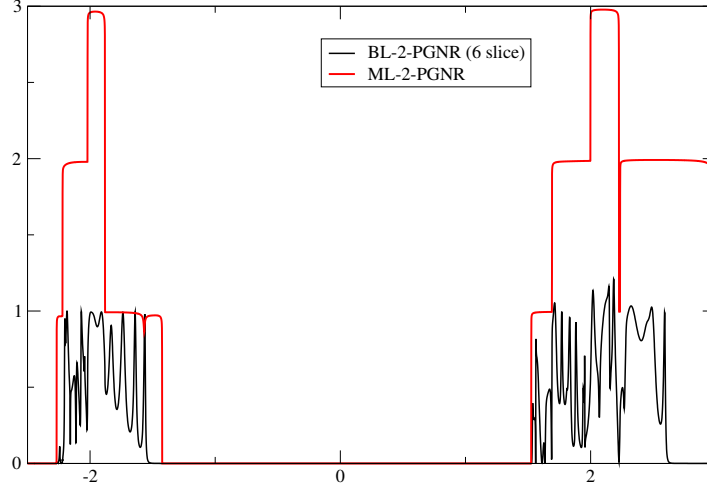


Figure 9.9: Transmission function for monolayer PGNR and a bilayer-PGNR with 6-slices in the central region.

same as in the monolayer case. We now construct a Hamiltonian for both electrodes as monolayers PGNR and subsequently a finite bilayer flake Hamiltonian with a determined length and width as inputs for the numerical routine [146].

In a first stage we have calculated the transmission as a function of energy for this setting as it is presented in fig. 9.9. Here we can observe two transmissions, the red line represents the monolayer transmission and black line depicts the bilayer transmission in the configuration mentioned above. In the monolayer case a quantized response with respect to energy can be appreciated. This is due to the opening and closing of conduction channels as we sweep the energy range. For the bilayer case, we appreciate that the quantized response is less definite, and several resonances arise due to a more complicated channel distribution in the bilayer system.

Once the electronic transmission is available, we can compute the thermoelectric coefficients. This is a straightforward task, since all quantities are expressed in terms of one integral (see equation 6.15) as was presented in the theoretical preliminaries section (see equations 6.16).

We obtained, for a particular length and width of the central region, the results presented in fig. 9.10.

We can observe that although PG is not a good electrical conductor (it is an

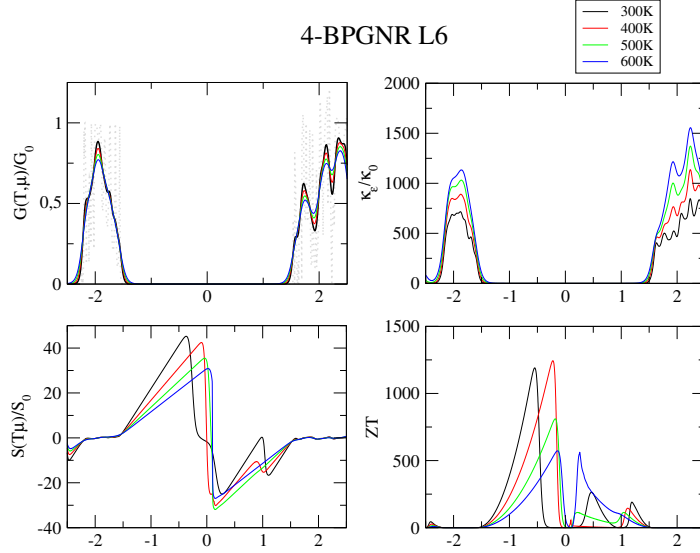


Figure 9.10: Thermoelectric coefficients for a 6-slice bilayer PGNR.

insulator indeed), thermoelectric performance is enhanced due to the electronic thermal conductivity reduction. A good Seebeck coefficient is obtained for the thermopower production of this configuration, in comparison with, for example, an analog geometrical setting based on graphene [58].

An important thing to mention at this point is related to the the ZT results. The magnitudes of this figure of merit are unreal, since the lattice thermal conductivity is not considered, only the electronic thermal conductivity is included. This is mainly due to the lack of a phononic band structure calculation similar to the electronic case. This phonon contribution can be computed by first-principles methods [57] or tight-binding models [56], but at this time is out of the scope of this work. However, we can give a rough estimation for this thermal conductivity in the PG case, by looking at the graphene case. Following [58] we found that the phononic contribution for κ in a graphene based system, is of the order of $\kappa_{ph} \approx (0.15 \text{ to } 0.28 \text{ nW/K})$. This can be taken as an upper bound for the PG case since in this case we expect greater anisotropy in the thermal conductivity due in part to different bond length and hybridizations [147].

Taking into account this contribution, we estimate that the figure of merit ZT will be at least of the order of unity, which is an acceptable starting value [59, 145]. Overall, this are promising results for the thermoelectric performance of PG. Also this could be improved by the use of other kinds of pentagonal materials.

Part III

Topological properties of penta-materials

Chapter 10

Results

10.1 Symmetry analysis

Following the guidelines of the TQC approach, the fundamental starting point for the analysis of penta-materials is the knowledge of their symmetry group. The only formal requisite we impose to this class of materials is that their space group ($P\bar{4}2_1mm$ /no. 113) remains unaltered. Specifically, this space group is nonsymmorphic; it includes a glide plane with a fractional translation vector given by $\mathbf{t} = (a/2, a/2, 0)$, where a is the lattice constant of the material (see section 10.1 for a description of the symmetry operations). In table (10.1) we present a summary of the space group data. The nonsymmorphic character has direct consequences on the energy band structure in momentum space, as we will see below.

The topological nontrivial character of a material is directly related to the behavior of high-symmetry points (HSP) and high-symmetry lines (HSL). If a reciprocal wavevector \mathbf{k} is a HSP or belongs to a HSL, there are certain operations of the space symmetry group G (modulo a reciprocal wavevector) that leaves it invariant. This set of operations form the so-called little group of \mathbf{k} , $G_{\mathbf{k}}$, which is a subgroup of G [25]. The two-dimensional BZ belonging to the space group no. 113 is presented in fig. 10.1. The most relevant set of k

| | C_1 | C_2 | C_3 | C_4 | C_5 | C_6 | C_7 |
|-------------|-------|-------|-------------|-------|-------|-------|------------|
| A_1 | 1 | 1 | 1 | 1 | 1 | 1 | 1 |
| B_1 | 1 | 1 | -1 | 1 | -1 | 1 | -1 |
| B_2 | 1 | 1 | -1 | -1 | 1 | 1 | -1 |
| A_2 | 1 | 1 | 1 | -1 | -1 | 1 | 1 |
| E | 2 | -2 | 0 | 0 | 0 | 2 | 0 |
| \bar{E}_2 | 2 | 0 | $-\sqrt{2}$ | 0 | 0 | -2 | $\sqrt{2}$ |
| E_1 | 2 | 0 | $-\sqrt{2}$ | 0 | 0 | -2 | $\sqrt{2}$ |

Table 10.1: Character table for point group isomorphic to space group no. 113

| | C_1 | C_2 | C_3 | C_4 | C_5 |
|-------|-------|-------|-------|-------|-------|
| M_1 | 1 | 1 | 1 | i | -i |
| M_2 | 1 | -1 | -1 | -i | i |
| M_3 | 1 | -1 | 1 | i | -i |
| M_4 | 1 | 1 | -1 | -i | i |
| M_5 | 2 | 0 | 0 | 0 | 0 |

Table 10.2: Character table for group G_M .

| | C_1 | C_2 |
|-------|-------|------------|
| Y_1 | 1 | ω |
| Y_2 | 1 | ω^* |

Table 10.3: Character table for group G_Y . $\omega = e^{i\mathbf{k}_Y \cdot \mathbf{t}}$.

points in this group for the subsequent analysis are Γ , X , M , and the Y -line.

Let us begin with Γ . All the transformations of the space group leave this point invariant, so its little group is isomorphic to the space group of the system (table 1). With respect to X , the symmetry transformations that leave the point invariant are I , C_{2z} , $(C_2^x | \frac{1}{2} \frac{1}{2} 0)$, $(C_2^y | \frac{1}{2} \frac{1}{2} 0)$. Therefore, there are three equivalence classes for G_X , and in principle the same number of irreps. However, using the $\sum h_l^2 = n$ constraint [27], where h_l is the dimension of the l -th irrep and $n = 4$ is the order of the group, we obtain that only a two-dimensional irrep can exist. This irrep is labeled as X_1 . For the M point, the invariant operations are I , C_{2z} , S_4^- , S_4^+ , $(C_2^x | \frac{1}{2} \frac{1}{2} 0)$, $(C_2^y | \frac{1}{2} \frac{1}{2} 0)$, $\{m_{x-y} | \frac{1}{2} \frac{1}{2} 0\}$, $\{m_{x-y} | \frac{1}{2} \frac{1}{2} 0\}$. Thus, M is invariant under the complete space group G , so $G_M \cong G$. However, as $k \neq 0$, we have a phase of $e^{i\mathbf{k}_M \cdot \mathbf{t}}$ that is present in the wavefunction at momentum space. As $\sum h_l^2 = 8$ it follows that $h_1 = h_2 = h_3 = h_4 = 1$ and $h_5 = 2$. The character table for this little group is given in table (10.2), that includes some complex characters due to the nonsymmorphic nature of the group. Finally, the symmetry transformations for the Y line are I , $(C_2^y | \frac{1}{2} \frac{1}{2} 0)$. Since we have two classes with only one element each, there are two irreps. The corresponding character table is shown in table (10.3), which also shows some complex characters.

The former data for the little groups allows for the description of degeneracies at these HSPs and HSLs. We thus analyze all points listed above. The Γ point has one- and two-dimensional real representations and then no TRS constraint is necessary. At X there is only one irrep with dimension two; therefore, this point always has a two-fold degeneracy for a spinless system. The M point has four complex-valued representations and one real-valued representation. TRS forces us to combine these four irreps in two pairs of conjugate physical irreps. This process yields pairs $M_1 + M_4$, $M_2 + M_3$ and real M_5 . All three physical irreps are two-dimensional. Thus, as long as TRS holds and the space group is nonsymmorphic, the energy bands at this point will be two-fold

degenerate. Finally, imposing TRS at the Y line we are left with only one possible physical irrep, $Y_1 + Y_2$, which is also two-dimensional. Therefore, every point located at Y has a two-fold degeneracy. It is worth to notice that the Y line, along with the X and M points, comprise all the nonequivalent points at the BZ boundary. As there is a two-fold degeneracy in each case, it occurs a two-fold band touching over the entire BZ perimeter. This phenomenon is known as a nodal-line degeneracy [148].

If the spin degree of freedom is taken into account, the first trivial consequence is the doubling of the spinless original degeneracy. In this case, the trivial addition of spin yields a four-fold degeneracy along the nodal line. A more interesting scenario arises when SOC is included. Symmetry considerations must be extended to include double groups [25, 27]. Consequently, the analysis for the little groups should be performed again, and the bands should be relabeled according to the new spinorial irreps.

Let us proceed with the analysis. The little group of the Γ point, G_Γ , is enlarged to embrace two new spinorial irreps labeled by $\bar{\Gamma}_6$ and $\bar{\Gamma}_7$; see Appendix III.B for the character tables of all the double groups used in this work, and Table III.B.1 for this particular group. As we can see, these two irreps are two-dimensional, which implies that the maximal degeneracy at this point is two. As we saw above, the X point is described by a unique two-dimensional irrep without spin; the inclusion of SOC enlarges the character table. This can be easily seen using the basic relation $\sum h_i^2 = 6$, where the solution is given by $h_1 = 2$ and $h_2 = h_3 = h_4 = h_5 = 1$. Thus, four new one-dimensional complex representations are added with respect to the spinless case. The character table for this group is presented in Table III.B.2. If TRS holds, these irreps are joined in conjugate pairs, giving two possible physical irreps, namely, $\bar{X}_2 + \bar{X}_4$ and $\bar{X}_3 + \bar{X}_5$, both two-dimensional. This last result implies that degeneracy is lifted, as in the Γ point, splitting the group of four bands into two pairs of bands. For the M point, the double group includes now two new spinorial irreps \bar{M}_6 and \bar{M}_7 , both two-dimensional. The character table for G_M is presented in table III.B.3. Again we have complex valued irreps. Under TRS these two irreps have to be paired in a single physical irrep, denoted as $\bar{M}_6 + \bar{M}_7$. This irrep is four-dimensional; being the only option for the spinful case, we conclude that the M point is unaffected by the inclusion of SOC, maintaining the four-fold degeneracy for the energy bands. Finally, the double group for Y line has two more irreps, \bar{Y}_3 and \bar{Y}_4 , as presented in the character table III.B.4. These two irreps are complex and one-dimensional. As in the previous cases, TRS implies the pairing of both irreps in the physical irrep $\bar{Y}_3 + \bar{Y}_4$, forming a two-dimensional irrep. Therefore, as in Γ and X , the possible four-fold degeneracy is lifted, yielding two stick-together, two-fold degenerate bands, along the whole line.

In summary, we have shown, based only on symmetry grounds, that the boundary nodal line disappears under SOC, leaving only a point-like degeneracy at M . The nodal character of this point will be later analyzed.

We finish the exploration of symmetries in penta-materials by relaxing time-reversal invariance. If TRS is broken, single complex irreps can be physical

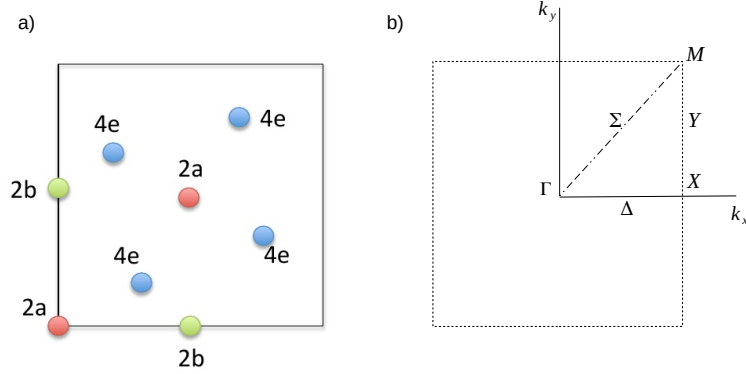


Figure 10.1: a) 2D projection of Wyckoff positions and b) 2D Brillouin zone for space group no. 113

representations without the need of coupling them in conjugate pairs. This has straightforward implications in the degeneracy landscape of the energy bands, with or without SOC. If TRS is absent and no SOC is considered, the following consequences can be deduced: (i) The Γ point is still four-fold degenerated; (ii) The X point becomes non-degenerate; (iii) M changes its degeneracy from four-fold to two-fold; and finally, (iv) at the Y line we find non-degenerate bands, implying the disappearance of the nodal line for this case.

Additionally, in the SOC plus TRS breaking case we can deduce the following: (i) at Γ nothing happens, since all irreps are already real; however, (ii) the conjugate pairs formed at X under TRS break apart in the single complex one-dimensional irreps $\bar{X}_2, \bar{X}_4, \bar{X}_3, \bar{X}_5$. Therefore, all bands are non-degenerate at this point. The M point, which had a protected four-fold degeneracy due to TR and nonsymmorphic symmetries, ends up with a pair of two-fold degenerated bands. Finally, the degeneracy of the Y line is lifted, leaving four non-degenerate bands for each group of the eight bands occurring in the spinful model.

| | I | C_2^z | \bar{I} | \bar{C}_2^z |
|-------|-----|---------|-----------|---------------|
| A | 1 | 1 | 1 | 1 |
| A' | 1 | -1 | 1 | -1 |
| E_1 | 1 | -i | -1 | i |
| E_2 | 1 | i | -1 | -i |

Table 10.4: Character table for the 4e WP site-symmetry group.

10.2 Topological analysis

To apply the topological analysis based on the symmetry description given in the previous section, we need to establish a model for the relevant energy range, namely, the vicinity of the Fermi level. All the penta-materials presented here have the pentagonal lattice of PG as a basic structure (fig. 9.1), which has six carbon atoms in its unit cell, four of them with coordination 3 and the other two with coordination 4. In terms of Wyckoff positions (WPs), the atoms with coordination 3 are located at a nonmaximal 4e WP, and those with coordination 4 are allocated in a maximal 2a WP. Figure 10.1 presents a graphical description of WPs for this particular space group.

With the WPs of the atoms identified, the real space description is completed enumerating the orbital components for each atomic site. The most important contribution for the considered penta-materials comes from the p_z orbitals, and in particular from atoms at the 4e WP. We present a minimal model for the topological analysis based on the four p_z orbitals at the 4e WP. Extensions to this model, including additional atoms, either adsorbed or as substitutions, can also be important and may involve other combinations of atomic orbitals. However, in terms of the essential topological behavior the main results are not modified, so we rely on this minimal model and discuss the necessary additions when be appropriate.

Once the real space model is complete, it has to be translated to momentum space, with the aim to compute its induced band representation and the subsequent topological characteristics. To calculate the corresponding band representation, the site-symmetry group (SSG) related to the 4e WP [119] should be identified. This group is composed of two operations, I , and $\{m_{x-y}|\frac{1}{2}\frac{1}{2}0\}$. Its character table is given in table (10.4) where we are only considering the first two columns and rows for the single-valued SSG. In a first stage we ignore spin-orbit coupling (SOC) and assume that TRS holds, which implies the use of physical irreducible representations [91]. The p_z orbitals transform as the A' irrep of this SSG. This information allows to define an induced band representation which gives as a result the symmetry (irrep labels) of the four bands throughout the entire BZ, as shown in table (10.5). Here we only show explicitly the TR symmetric points Γ , X and M .

A straightforward observation is that this band representation is composite [91]. This is to be expected, since our model is based on p_z orbitals located at non-maximal WP. Nevertheless, we can express this band representation as a

| BZ point | $A' \uparrow G$ |
|----------|-----------------------------------------------------|
| Γ | $\Gamma_1(1) \oplus \Gamma_3(1) \oplus \Gamma_5(2)$ |
| X | $2X_1(2)$ |
| M | $M_1(1)M_3(1) \oplus M_5(2)$ |

Table 10.5: Band representation for 4e WP with TR and no SOC.

| BZ point | $E_1 + E_2 \uparrow G$ |
|----------|------------------------------------|
| Γ | $2\Gamma_6(2) \oplus 2\Gamma_7(2)$ |
| X | $2X_2X_5(2) \oplus 2X_3X_4(2)$ |
| M | $2M_6M_7(4)$ |

Table 10.6: Band representation for 4e WP, with SOC and TR.

| BZ point | $2E_1 \uparrow G$ |
|----------|----------------------------------------------------|
| Γ | $2\Gamma_6(2) \oplus 2\Gamma_7(2)$ |
| X | $X_2(1) \oplus X_3(1) \oplus X_4(1) \oplus X_5(1)$ |
| M | $2M_6(2) \oplus 2M_7(2)$ |

Table 10.7: Band representation for 4e WP with SOC and no TR

sum of EBRs coming from maximal WP: $A' \uparrow G = (2a) \uparrow G \oplus (2c) \uparrow G$ (see [28] for the complete list of EBRs for the group). The most important conclusion for this model is that all sets of bands are two-connected, and therefore all bands are topologically trivial. Particular examples of this phase show some variations of the electronic character of the material, depending on the specific band filling. The inclusion of SOC can lead to the appearance of additional phases in these materials. This implies the use of a double group (double SSG) description, as mentioned before. The character table for the corresponding double group is given in table (10.4). Due to TRS, we apply the conjugate pair procedure and join the \bar{E}_1 and \bar{E}_2 irreps in a single $\bar{E}_1 + \bar{E}_2$ physical irrep for the spinful orbitals. This two-dimensional irrep induces a band representation in reciprocal space shown in table (10.6).

The above band representation takes into account eight bands arising from the spin degree of freedom. Additionally, by exploring the character of all the EBRs with TRS for this double group, it can be verified that all sets of bands are connected, with a maximum of 4-connected bands (see [28]). Thus, all bands are trivial in this case. Still, we have some SOC-induced transitions at the HSP and HSL that modify the degeneracy order as mentioned in the above symmetry analysis, this has consequences on the electronic properties of particular penta-materials (see next Section).

Finally, we consider TRS breaking, so complex valued irreps are allowed. With the same induction procedure employed above, we found the band representation shown in table 10.7.

| HSP path | Character |
|-------------------------------------------------------|-------------|
| $\Gamma_6 \rightarrow X_2 \oplus X_4 \rightarrow M_6$ | trivial |
| $\Gamma_7 \rightarrow X_3 \oplus X_5 \rightarrow M_7$ | topological |
| $\Gamma_6 \rightarrow X_3 \oplus X_5 \rightarrow M_6$ | topological |
| $\Gamma_7 \rightarrow X_2 \oplus X_4 \rightarrow M_7$ | trivial |
| $\Gamma_7 \rightarrow X_2 \oplus X_4 \rightarrow M_6$ | topological |
| $\Gamma_6 \rightarrow X_3 \oplus X_5 \rightarrow M_7$ | trivial |
| $\Gamma_7 \rightarrow X_3 \oplus X_5 \rightarrow M_6$ | trivial |
| $\Gamma_6 \rightarrow X_2 \oplus X_4 \rightarrow M_7$ | topological |

Table 10.8: Topological phases

This is a composite band representation formed by two groups of four bands. We study only one group, since the other one has exactly the same structure.

As it is well-known, degeneracy is lowered by TRS breaking. This is reflected in the band representation which becomes decomposable, a signal for the presence of a topological set of bands [91, 119, 124]. If an EBR is decomposable, then different connectivity paths can appear among the high-symmetry points and lines through the BZ, which implies different topological phases in the material. The different topological realizations of the band representation correspond to all possible solutions of the compatibility relations between HSP and HSL over the BZ. We have carried out this process for a two-dimensional BZ of the space group of penta-materials, finding the connectivity solutions presented in table (10.8).

These sets of bands have to be compared with the EBRs that the space group induces in the momentum space. As a general rule, if a band representation can be expressed as the combination of some EBRs, then the set of bands is trivial [119]. Comparing the results for the band representations above with all possible ERBs, it can be seen that some sets cannot be expressed in terms of EBRs; in conclusion, such bands are topological. The labeling presented in the former table (10.8) depicts this situation.

There are four different possible connectivities that depend on the particular characteristics and band filling of the material. We can build a toy model to grasp the general behavior of these phases by fixing the energy ordering of bands (irreps) to some particular sequence at HSP and HSL. The possible outcomes are depicted graphically in fig. 10.2. There are three phases presenting nodal degeneracy and one phase with gapped character. The knowledge of the specific band filling is necessary in order to classify this topological behavior as semi-metallic or insulating. This is strongly material-dependent, making it necessary to analyze the specific cases. In particular, for penta-materials studied in this work, there is an interplay of semi-metallic phases with or without nodes, along with electron or hole pockets near the Fermi energy, an scenario that has been found for other systems [109].

In summary, if TRS is preserved and no SOC is included, penta-materials

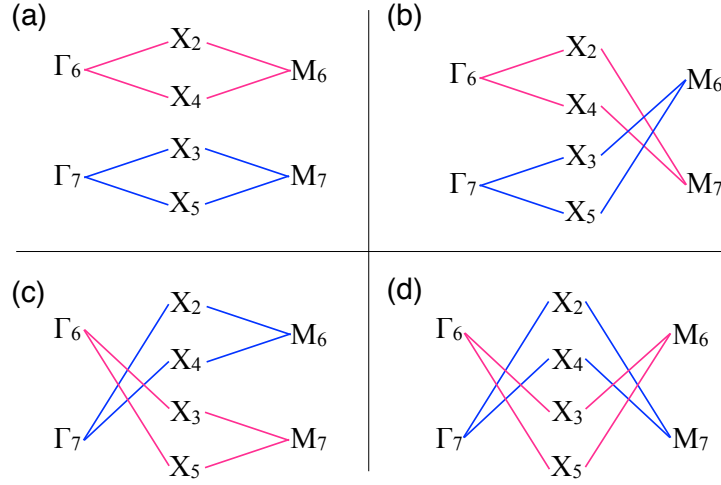


Figure 10.2: Scheme of the energy ordering of bands (irreps) to some particular sequence at HSP and HSL.

possess a general band structure with trivial bands in all its energy range, displaying a perimeter nodal line. The inclusion of SOC while maintaining TRS yields also trivial bands, but some degeneracies are lifted in the BZ, changing the character of the electronic properties. Breaking TRS with SOC produces a decomposable band representation that gives rise to four different topological phases, according to the distinct possibilities for the band connectivity.

This exhausts our study of the electronic band structure for penta-materials within a general group theory framework. Naturally, other perturbations could be included in order to modify the symmetry character of the underlying lattice with the possible induction of more topological phases.

In the following section we apply this general group-theoretical description to some specific penta-materials. This is done with the aid of first-principles calculations and effective models.

10.3 Examples of penta-materials

Penta-materials comprehend a family of materials with a pentagonal lattice structure, which in its two dimensional projection resembles to the Cairo tiling (see Fig. 9.1). The basic definition for these materials is that all have the same space group, that is no. 113 space group. There exist other types of pentagonal materials which have a Cairo tiling lattice, but with a planar space

group. We leave this subclass out from our definition of penta-materials since we are interested in the particular space group mentioned above.

The first instance of this family of materials is penta-graphene. It has an all-carbon lattice structure and an insulating character. Two conduction bands and two valence bands are the main contributors to the low-energy range [4]. Applying the TQC analysis we obtain that only (p)EBRs occur in the band structure of PG. Thus it can be concluded that, since carbon has a weak SOC and TRS holds, PG is a trivial (band) insulator. However, as mentioned before, we can explore additional configurations by functionalization, adsorption or doping of penta-graphene without altering its original symmetry. We will study materials with substitutional doping and metallic adsorption in selective lattice sites (replacing atoms in different WPs). These new configurations enhance the spin-orbit coupling of the system and can also induce time-reversal symmetry breaking, which allows the exploration of all the phases described in the symmetry and topological analysis.

This proposition can be reinforced by an electron filling analysis as presented in [134]. For the PG space group (No. 113) the band insulator filling is dictated by a $4n$ relation, where n is a positive integer. For PG this yields a band filling of 36, which results in a band insulator state. If we substitute some carbon atoms we deviate from the $4n$ -band filling, accomplishing a condition for the filling-enforced formation of a nodal (semi)-metal. This has to be additionally cross-checked with a chemical stability study of the material [135].

We present first-principles calculations for some penta-materials based on PG, with an emphasis in both, global and local features of their energy bands. We explain the modifications performed in PG to achieve the penta-material and the particular phase realizations with respect to our previous symmetry and topological analysis.

10.3.1 Symmetry-protected metallic phases

In order to access the metallic phases, i.e., to shift the conduction or valence bands, other elements rather than carbon should be added to PG. We first functionalize PG with adsorption of metallic atoms at 4e WP. This case has been previously explored for various elements, showing metallization of PG [12, 2]. An example of a relaxed lattice structure with adsorbed Li is presented in fig. 10.3. Also, electronic band structure calculations are shown for this case of Li-adsorbed PG (Li-PG) as well as Na-adsorbed PG (Na-PG) in fig. 10.4.

Another possibility is the substitutional doping of PG. Particularly interesting for this work is the 2a WP doping, forming a penta- XC_2 configuration [149, 3, 17], where $\text{X}=\{\text{B}, \text{N}, \text{P}, \text{Si}, \text{G}\}$. The lattice structure of these materials is exactly the same as PG, with modifications in the relative bond magnitudes and lattice constant. We show the band structure calculations for $\text{X}=\text{B}, \text{N}, \text{P}$ in fig. 10.5.

As these theoretical materials preserve the PG space group $P\bar{4}2_1mm$, they show a similar trend in the electronic band structure. However, now there is

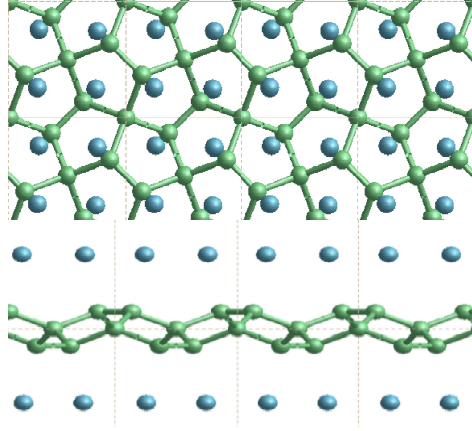


Figure 10.3: Li-PG relaxed lattice.

a fractional filling of the conduction (valence) band, which can be described in this trivial phase (no SOC + TRS) by a single EBR. As stated by Bradlyn *et al.* [91], if the Fermi level sits on a single EBR with fractional filling, the corresponding material is necessarily a protected (semi)-metal. Thus, all these metal-PG and penta- XC_2 materials are symmetry-protected metals.

We have some remarks about this result. The above-mentioned symmetry protection is of crystalline character; since the space group is nonsymmorphic and TRS symmetry is preserved, it implies the well-known "stick-together" phenomenon for energy bands [27] along the Y line. This effect can be seen in the band structures of all penta-materials in this regime. It is remarkable that the sticky bands occur along all the BZ boundary. This implies that there is a trivial crystalline nodal line for these penta-materials. The nodal line presents a certain dispersion, i.e., it is not at constant energy in momentum space. This effect is mainly induced by the lack of inversion symmetry which moves the nodal states to different energies, a fact that has been demonstrated in general in previous works [109, 148].

For PG-adsorbed or substituted materials, although the nodal line is energy-dependent, it crosses the Fermi energy, producing a single nodal point plus pockets of electrons or holes. This can be clearly seen in the band structures shown in figs. 10.4 and 10.5. Looking closer to the local low-energy behavior of the nodal line at the vicinity of the Y line, we observe that bands have a linear dependence on k_x along k_y -constant lines, so these carriers behave as massless fermions. This can be observed in a momentum space cut presented in fig. 10.6. The massless fermion low-energy dispersion becomes more relevant if the Fermi level actually sits on a state of the nodal line. This crucially depends on the band filling fraction, being realizable in some of the materials studied.

Notice that, although we have a trivial phase in these materials, we still can have protected edge states. This can be explained in terms of the ten-fold way

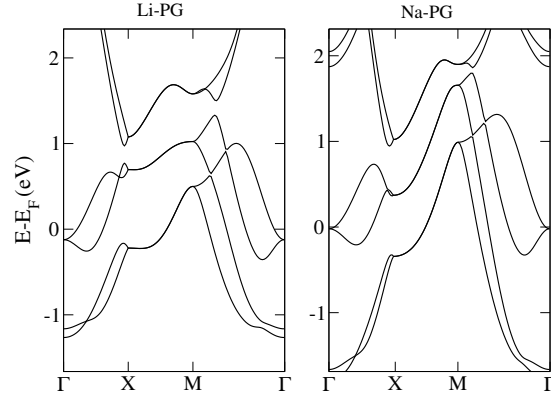


Figure 10.4: Li-PG and Na-PG band structure.

classification of the Fermi surface [131]. As the considered materials belong to the AIII (chiral unitary) class, for spatial dimension $d = 2$ a trivial phase arises, as expected. But due to an inherited non-triviality from another related AI (orthogonal) class, robust edge states that present linear or dispersionless characteristics might appear [1].

Next, the inclusion of SOC is explored by means of first-principles calculations. To this end, we use as an example penta- PC_2 . Its band structure is presented in fig. 10.7. As we are dealing with light elements the effect of SOC is rather weak; therefore, all these materials will behave as nodal line semi-metals at room temperature. Notwithstanding, the results derived by the symmetry analysis are confirmed. Namely, degeneracies at Γ and X points and along the Y line are lifted. Likewise, the robustness of the M point four-fold degeneracy is confirmed by these calculations, which allow us to classify this as a new metallic phase [110]. The symmetry that protects the "stick-together" effect along the Y line is broken, and the degeneracy of the above-mentioned high-symmetry points is also modified, implying the disappearance of the nodal line. Therefore, for these penta-materials, SOC plus TRS enforces a transition from a nodal-line metallic state to a spin-orbit Dirac-node metal with nodal points located at M [150, 111], both phases being topologically trivial.

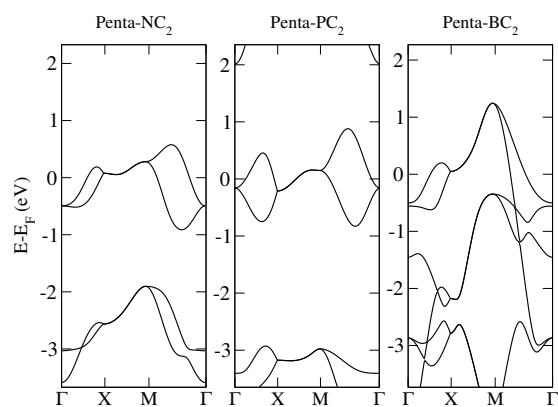


Figure 10.5: Band structures for doped PG penta-materials.

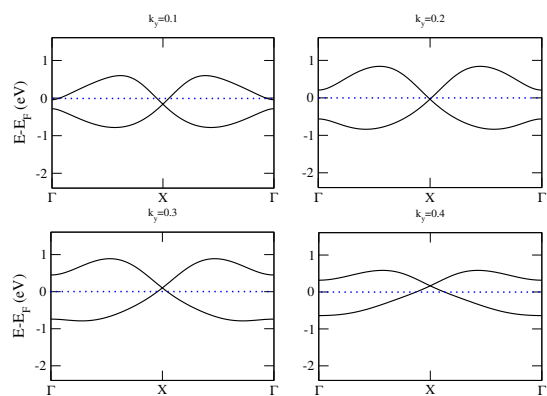
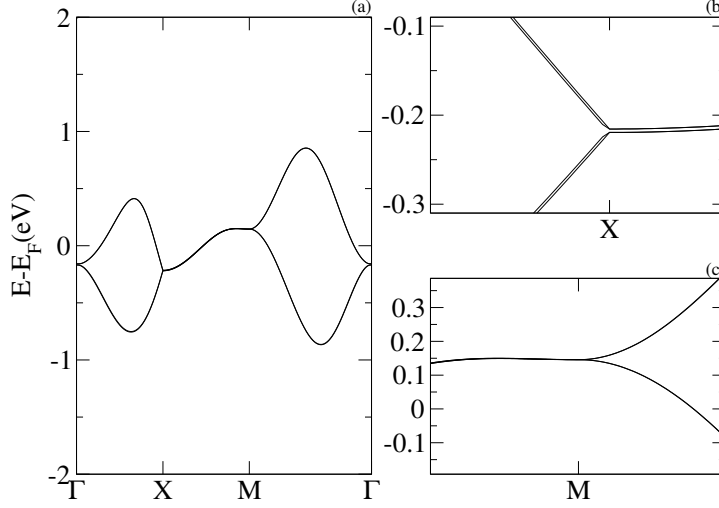


Figure 10.6: BZ cuts for the band structure of penta-NC₂.

Figure 10.7: Band structure for penta-PC₂ with SOC.

10.3.2 Topological phase: breaking TRS

A final stage in the topological phase analysis of penta-materials, consists in the application of a TRS breaking perturbation. To do this it is necessary to make use of a magnetic field-related perturbation, such as an external applied field or a substitution by magnetic atoms [109]. In first-principles calculations, the only practical way to introduce some magnetic field perturbation is by introduction of magnetic atoms [151]. Accordingly, we present a magnetic substitution for penta-materials, using a transition metal element, with considerable spin-orbit coupling contribution.

In particular, manganese-doped PG was selected to analyze this topological phase. Manganese substitutes carbon atoms at 2a WP (see lattice in fig. 9.1). As we have seen from the TQC study, topological nontrivial character arises in bands where p orbitals have contribution. The type of topological bands, depends on the specific energetic ordering of the material. To characterize this topological phase we will use WFs and Wannier charge centers analysis to compute some topological invariant for the particular system at hand [137].

The initial step is to compute the band structure for this material. We make use Quantum Espresso package including SOC and fully relativistic pseudopotentials from ONVC code [152]. Additionally, an antiferromagnetic initial state is set for the Mn atoms in the primitive unit cell, fixing one Mn atom (cell ori-

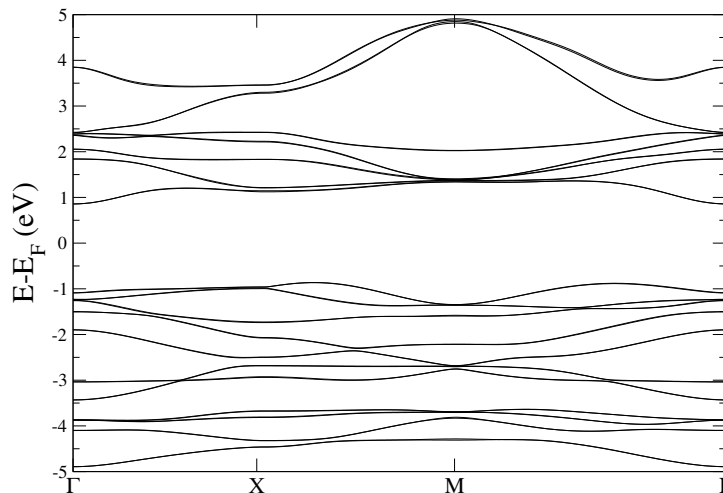


Figure 10.8: DFT band structure calculation for Mn-PG.

gin) in a spin up state and the other (cell center) in a down spin state.¹ This allows to explore TRS breaking from manganese magnetism plus a SOC contribution intrinsic to this element. The resulting band structure is presented in fig. 10.8. It can be seen that this penta-material is an insulator in bulk, with an indirect band gap of ~ 1.75 eV.

Once the band structure calculation is available, a Wannier charge center calculation must be performed. For this, it is necessary to build an effective model based on WFs. This last model is done by projecting from the first-principles energy bands and eigenstates to a Wannier function basis selected from an initial atomic set. The Wannierization is carried with the Wannier90 code [153], which takes as an input the DFT energy bands and fits a low energy model for the Fermi level bands (see appendix III.C for more details on the code use). We have obtained Wannier bands for this Mn-PG with SOC contribution. The result for this WFs model is depicted in fig. 10.9. We see that the vicinity of the Fermi level is well represented in this wannierization being able to be used as the starting point for the WCC study.

The WCC calculation was performed using another post-processing code called WannierTools [139]. This package takes the wannier90 Hamiltonian in a tight-binding format and calculates the associated Wannier charge centers with the translation method of Soluyanov *et al.* [116, 137]. As we have seen in the theoretical section, Wannier charge centers are defined as the expectation value for the position operator of some previously chosen spatial direction (see eq. 8.12). In this particular case, The Brillouin zone is two-dimensional and thus there are only two ways for the hybridization procedure required. We

¹The other equivalent phase with opposite ordering, was also analyzed giving the same results.

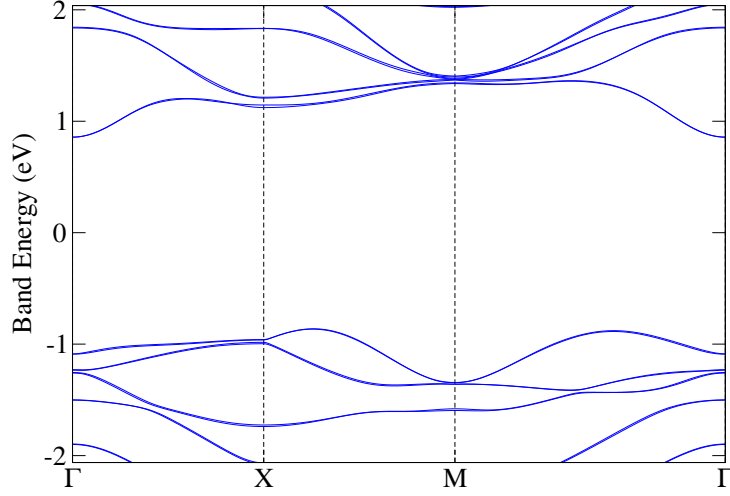


Figure 10.9: Mn-PG bands from the Wannier90 code.

can choose to calculate the \bar{y} direction WCC or the \bar{x} direction WCC. Both directions must be respectively computed in order to see how strong is the non-trivial phase in this material [122]. More in detail, we fix the integration k -vector and the spatial direction (x or y) for WCC calculation, and the evolution of the WCCs is analyzed along the k -line [139](see appendix III.D for more details of the WCC input).

The WCC analysis can be done, by the calculation of accumulative quantities from individual WCCs. These correspond to the total sum of the WCCs at each point in the k -line and to the larger gap $\Delta\bar{x}_i$ between two WCCs, also at one particular k -point [116]. The evolution of these two functions all over the the entire k -path gives clear hints of the topological character of the highest occupied band that we have chosen [138]. In particular

$$\sum \bar{x}_i \rightarrow \text{Chern number}, \quad (10.1)$$

$$\sum \text{wcc between } \Delta\bar{x}_i \rightarrow \mathbb{Z}_2 \text{ invariant}.$$

These two values can be extracted directly from the WCC calculation; \mathbb{Z}_2 invariant can be calculated by counting the total number of WCCs that are covered by all the discontinuous jumps of $\Delta\bar{x}_i$ along the k -line. The number of bands pierced by jumps will give the indication of an even or odd \mathbb{Z}_2 which serves to identify TR invariant phases as trivial or non-trivial [138]. The Chern number can be calculated as the total winding number in the spatial direction (vertical axis) as the $\sum \bar{x}_i$ evolves in k -path [137, 118, 122].

We calculate the Chern number for the Mn-PG penta-material for the two primitive directions in real space, x and y . In particular, the occupation is fixed

at the gap as the Fermi level location. This occupation will tell us if the gap has a nontrivial character. The calculation of the WCCs and the associated Chern number are presented for both directions in Figs 10.10 and 10.11 respectively. This computation was carried with the Z2Pack code [138].

In addition we have to study the edge states of the material to see if we have a bulk boundary correspondence. To analyze this, the edge band structure for the WF model has been calculated in order to observe boundary states. This calculation was with WannierTools, and the obtained band structure for a 10-slab structure along different spatial directions is presented in figs. 10.12, 10.13 and 10.14. It can be appreciated that some edge states appear at the bulk gap. The topological nature of this state has to be further analyzed.

Thus we have a Chern insulator phase for this Mn-PG. Other phases can be explored for this same penta-material by controlling the inversion symmetry breaking, with the possible presence of Weyl nodes in the bulk band structure [104, 1].

□ In summary a whole family of materials, pentagonal materials, were presented. Its symmetry and topological properties were studied based on group theoretical and TQC grounds, which results in a complete classification of the trivial and nontrivial band character. This general framework was applied to particular penta-materials, were both (semi)-metallic and insulating phases were analyzed, including SOC and TRS breaking by magnetic atomic substitution. We have found that most of these materials are trivial in the TRS case, even with SOC inclusion, yielding nodal-line or Dirac-node metallic phases. The nontrivial phase arises with in the TRS breaking regime, were a magnetic penta-material was presented, showing a two dimensional Chern insulator character. All these phases and others not explored here give these pentagonal materials great value as examples of two-dimensional symmetry-enforced metallic and topological phases, which deserve to be more amply studied in the future. □

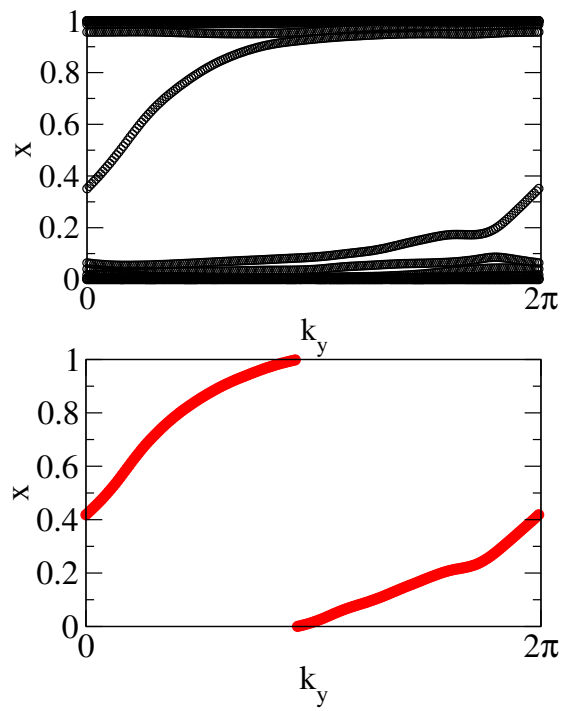


Figure 10.10: Top: WCC evolution. Bottom: sum of WCC for the x direction.

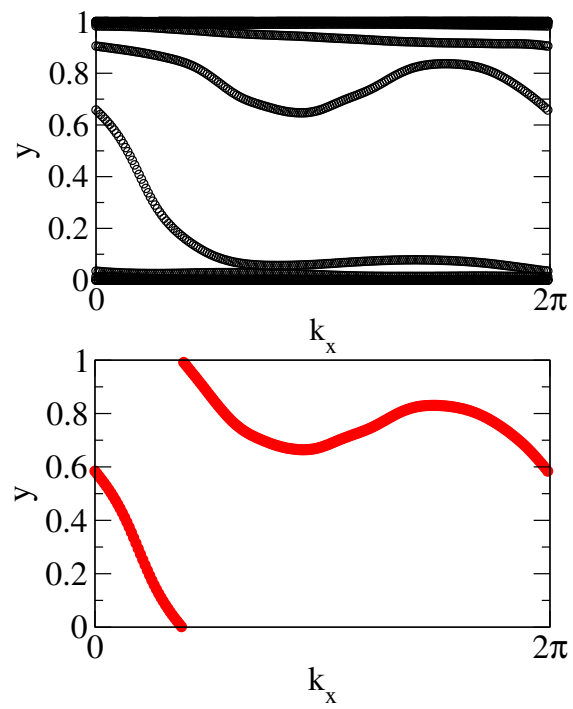


Figure 10.11: Top: WCC evolution. Bottom: sum of WCC for the x direction.

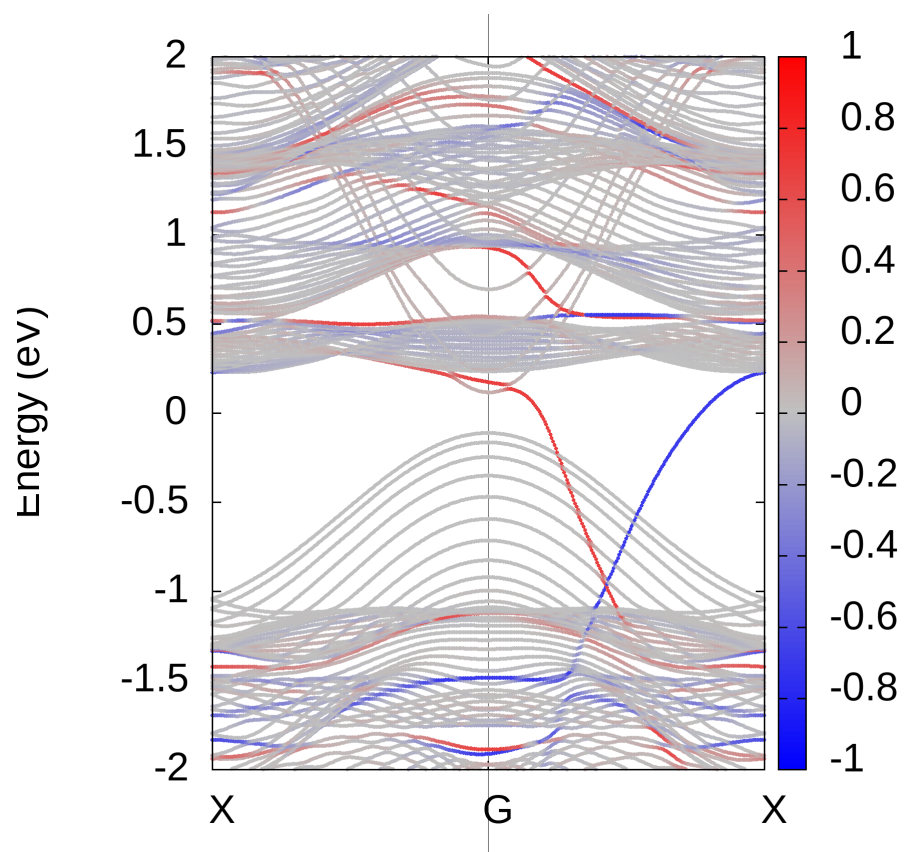


Figure 10.12: (100) band structure for a 10-slab along $X\Gamma X$ BZ path. Color scale indicates surface weight, with +1 for right edge and -1 for left edge.

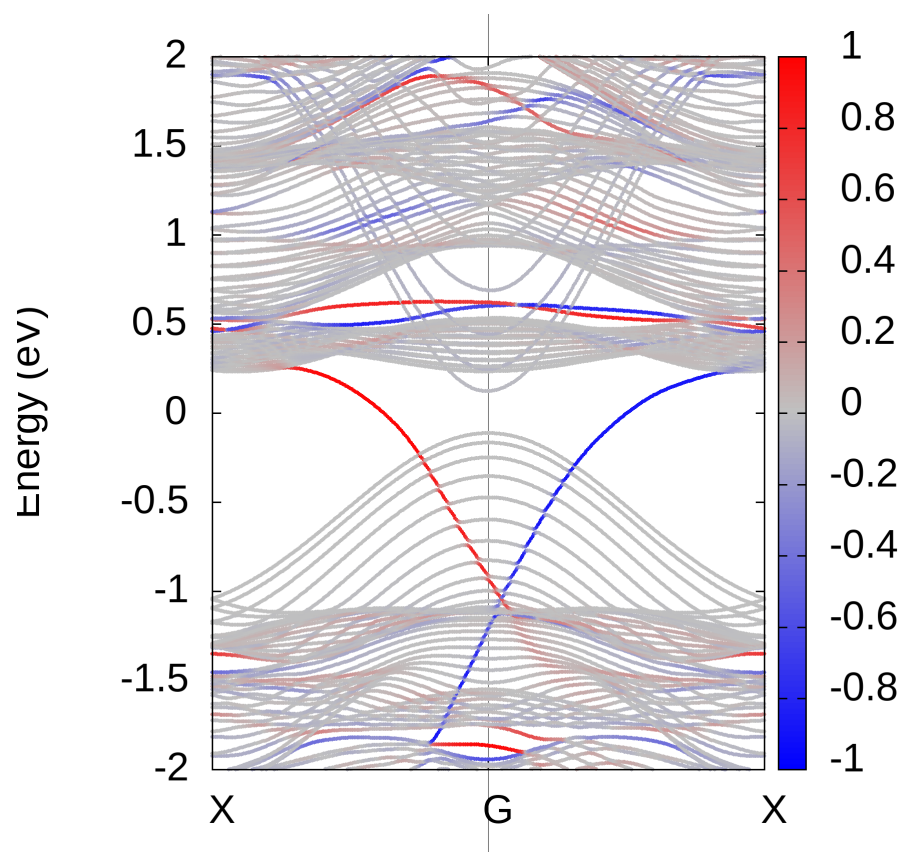


Figure 10.13: (010) band structure for a 10-slab along $X\Gamma X$ BZ path. Color scale indicates surface weight, with +1 for right edge and -1 for left edge.

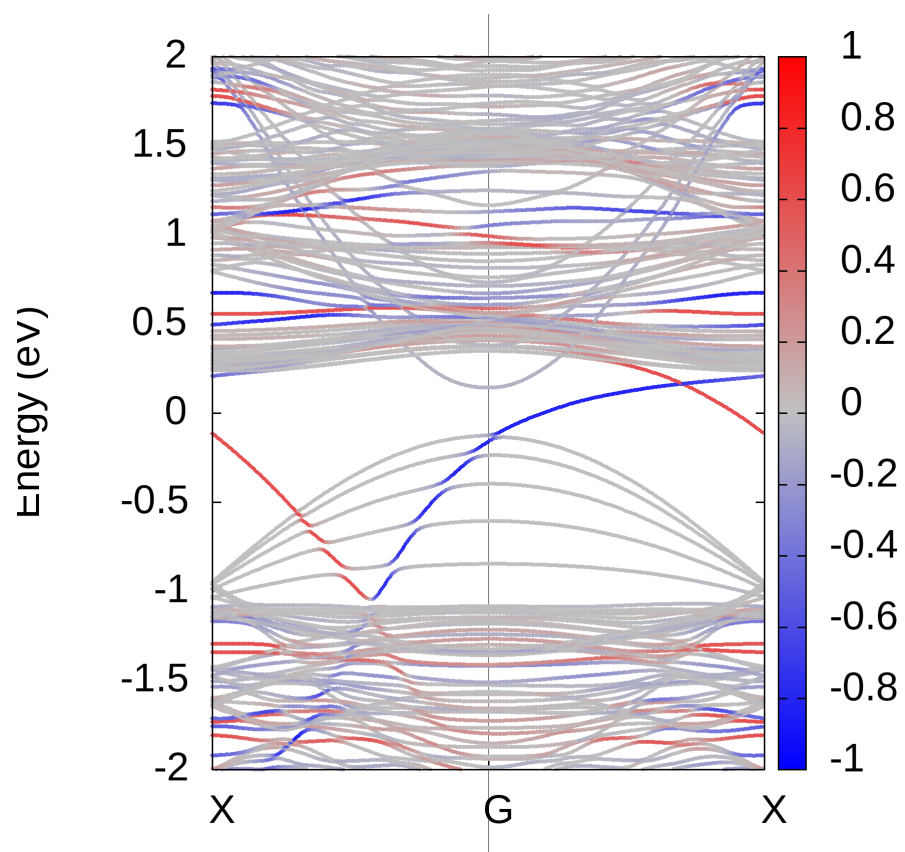


Figure 10.14: (110) band structure for a 10-slab along $X\Gamma X$ BZ path. Color scale indicates surface weight, with +1 for right edge and -1 for left edge.

Chapter 11

Conclusions

In this thesis we have presented the study of pentagonal materials based on penta-graphene through the analysis of different physical phenomena. This subgroup of the family of penta-materials presents remarkable properties under atom substitution and adsorption.

In first place, penta-graphene was found to be a wide band gap material with an optical response that may have applications in opto-electronic devices. Also, penta-graphene nanoribbons showed the same tendency in the optical absorption within the developed Slater-Koster tight-binding model. Other interesting result is related to the thermoelectric performance of penta-graphene, where this material yields a good thermopower Seebeck coefficient. This and other thermoelectric coefficients are comparable with known efficient thermoelectric materials. This was in part by the clever design of the transport device, which has a spatial mismatch of two ribbons that goes in direct detriment of the lattice thermal conductivity enhancing the figure of merit ZT.

Going beyond penta-graphene by doping and adsorption, it was found that breaking the insulator band filling of penta-graphene entails a symmetry-enforced metallic transition. This is a very important effect, since the main characteristic of these materials is their nodal line along the perimeter of the Brillouin zone. Thus with these new pentagonal systems we can have access to the nodal fermions at Fermi level. This novel character of penta-materials was overlooked or briefly mentioned in previous works.

In order to explore more deeply the implications of this particular band structure, spin-orbit coupling was introduced by means of an adequate doping. We obtained that SOC destroys the nodal line by splitting the energy bands with exception of the M-point. This point becomes a Dirac-node point, with a four-fold degeneracy and the peculiarity of being protected against SOC due to the nonsymmorphic character of the space group. This kind of nodal points is of great interest nowadays because of their robustness against perturbations.

Additionally, magnetic substitution allows us to break time-reversal symmetry in a direct way, giving the possibility to explore a topologically non-trivial phase. This phase was characterized with the aid of topological quantum chem-

istry as being non-trivial with the presence of a disconnected band representation. This gives rise to a Chern insulator phase according to the periodic table of topological insulators and superconductors. The used material was Mn-PG, which was studied by means of the Wannier charge center evolution method showing a non-zero Chern number. We can mention that other functionalizations of PG could yield a non-trivial metallic electronic structure, with presence of nodal points in the band structure of the bulk.

Therefore, after this comprehensive study of PG-derived pentagonal materials, it turns out that this family has very promising features both, in the area of fundamental physics and as a candidate for the implementation of new technologies based on low-dimensional systems.

Part IV

Appendices

Chapter 12

Part II appendices

12.1 Appendix: Tight-binding code description

We briefly describe the tight-binding code we use for the Slater-Koster (S-K) parameterization. This code was written in Python language, having the following characteristics

- The input for the program consists of the atomic positions for the primitive unit cell of the material and some list of k points in a standard Quantum Espresso format [39]. Also, an initial guess for the S-K parameters must be given in order to use the *fitting* procedure.
- Next, the code establishes nearest neighbors with the common definition of translation vectors $\mathbf{a} = n\mathbf{a}_1 + m\mathbf{a}_2 + l\mathbf{a}_3$ where n , m and l are integers [22]. This is necessary for the matrix element definition.
- An orbital sub-matrix is defined in a module with corresponding S-K decomposition as expressed in [41]. In our case we include s and p orbitals.
- The Hamiltonian matrix is defined in the usual TB form

$$H_{\alpha\beta}(\mathbf{k}) = \sum_{\mathbf{R}_{ij}} e^{i\mathbf{k}\cdot\mathbf{R}_{ij}} t_{\alpha\beta}(\mathbf{R}_{ij}).$$

Diagonalization of this matrix is carried with the 'scipy.linalg' Python package using the 'eigh' routine, obtaining eigenvalues and eigenvectors.

- This is the main loop of the process. This can be used for
 - *Fitting procedure*: In this case we use the 'scipy.optimize' Python package with *minimize* routine to find the best fit from the initial guess of the S-K parameters. Here a DFT band structure calculation must be provide to the subroutine fitting.
 - *Band structure calculation*: Here only eigenvalues are calculated over a predefined k -path and then plotted. This procedure assumes

that a correct set of S-K must be provided to give a good band structure graph.

- *Optical absorption calculation:* A routine in an external FORTRAN module is defined to accelerate the numerical calculation. A dense k-point grid must be provided in order to obtain good convergence (external input). Using eq. (5.13) directly coded in the FORTRAN script, optical absorption is calculated over an energy range given by the user.
- *Ribbon calculation:* band structure and optical response can be also calculated for ribbons. The Hamiltonian is built in a block form based on the finite cell dimension given externally by the user as an integer N. Thus N Hamiltonian copies are defined taking into account intracell interactions in the off-diagonal elements and terminations of the ribbon. After the obtention of the Hamiltonian, same band structure and optical absorption modules are used as in the bulk case.

This procedure was successfully implemented for PG and PG ribbons. It can be also be used to parameterize any pentagonal material that we have presented in this work with the corresponding change in the lattice parameters.

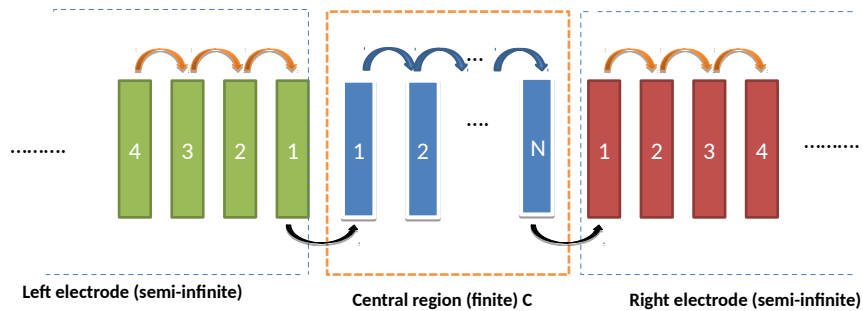


Figure 12.1: Layer decomposition of a transport system.

12.2 Appendix: Recursive Green's function method

In order to compute the physical response of nanostructured systems a reliable, fast and automatizable procedure is mandatory. A candidate for this task is based in the implementation of a well-known recursive algorithm presented decades ago in [54, 55]. This routine is combined with standard formulas for transport quantities expressed in terms of Green's functions (see transport section).

The particular form of the algorithm, suitable for numerical calculations, requires a discrete formulation of the device. This is achieved by a tight-binding representation of the system, in terms of intralayer and interlayer terms. Layer dimension in the translation direction is chosen by the condition that only nearest-neighbors layers have a non-negligible contribution [53]. Thus for each layer a Hamiltonian matrix must be defined. Coupling between layers is taken into account with hopping matrices with only non diagonal terms. A graphical depiction of this abstract subdivision is presented in fig. 12.1.

The target of the computation is to calculate the surface GF G_{11} for a semi-infinite chain and also for a finite chain, where the complete chain GF can be obtained after in the process.

With this setting, the surface GF of the system is calculated by the following algorithm [54, 55, 146]

- Consider a three-site initial system labeled with $n = 1, 2, 3$ respectively. Then using Dyson's equation [51], we can formulate an interaction surface GF for the site 1, G_{11} , as

$$G_{11} = g_1 + g_1 t G_{21}, \quad (12.1)$$

$$G_{21} = g_2 t G_{31} + g_2 t^* G_{11}. \quad (12.2)$$

Where $g_i = (\omega - \epsilon_0 + i\eta)^{-1}$ is the non-interacting GF for site i , and t is the hopping term.

- Solving for G_{11} in the above system we find

$$(1 - g_1 t g_2 t^*) G_{11} = g_1 + g_1 t g_2 t G_{31}. \quad (12.3)$$

- The non-diagonal term G_{21} can be generalized for a n-site system such as G_{n1} which is given by

$$G_{n1} = g_n t G_{n+1,1} + g_n t^* G_{n-1,1}. \quad (12.4)$$

- If we write $G_{n+1,1}$ and $G_{n-1,1}$, which are both non-diagonal also, in terms of recursive formula (12.4) then we obtain

$$G_{n+1,1} = g_{n+1} t G_{n+2,1} + g_{n+1} t^* G_{n,1},$$

$$G_{n-1,1} = g_{n-1} t G_{n,1} + g_{n-1} t^* G_{n-2,1}.$$

- Replacing in eq (12.4) and solving for $G_{n,1}$

$$G_{n,1} = \frac{g_n t g_{n+1} t G_{n+2,1} + g_n t^* g_{n-1} t^* G_{n-2,1}}{1 - g_n t g_{n+1} t^* - g_n t^* g_{n-1} t}. \quad (12.5)$$

- Defining new variables as

$$\alpha_1 = t g t, \quad (12.6)$$

$$\beta_1 = t^* g t^*,$$

$$\tilde{\epsilon}_1 = \epsilon + t g t^*,$$

$$\epsilon_1 = \tilde{\epsilon}_1 + t^* g t,$$

it is possible to express G_{n1} in the form

$$(\omega - \epsilon_1 + i\eta) G_{n1} = \alpha_1 G_{n+2,1} + \beta_1 G_{n-2,1}. \quad (12.7)$$

- This formula generates a recursion relation which only involves second nearest neighbors. Nearest-neighbor couplings are now part of the new coupling definition in term of α_1 and β_1 . This is a renormalization technique for the layers.
- The structure of eq. (12.7) is similar to eq. (12.4), and thereby we can repeat the renormalization process done before, this time starting from $G_{n+2,1}$ and $G_{n-2,1}$. This new decimation process after x iterations gives as a result

$$\begin{aligned}
(\omega - \epsilon_x^S + i\eta) G_{11} &= \alpha_x G_{31} + 1, \\
(\omega - \epsilon_x + i\eta) G_{2^x 1+1,1} &= \alpha_1 G_{2^x 2-1,1} + \beta_1 G_{2^x 0-1,1}, \\
&\vdots \\
(\omega - \epsilon_x + i\eta) G_{2^x n+1,1} &= \alpha_x G_{2^x (n+1)-1,1} + \beta_x G_{2^x (n-1)+1,1}.
\end{aligned}$$

Where

$$\begin{aligned}
\alpha_x &= \alpha_{x-1} g_{x-1} \alpha_{x-1}, \\
\beta_x &= \beta_{x-1} g_{x-1} \beta_{x-1}, \\
\epsilon_x^S &= \epsilon_{x-1} + \alpha_{x-1} g_{x-1} \beta_{x-1}, \\
\epsilon_x &= \epsilon_x^S + \beta_{x-1} g_{x-1} \alpha_{x-1}, \\
g_x &= (\omega - \epsilon_{x-1} + i\eta)^{-1},
\end{aligned} \tag{12.8}$$

are the renormalized coupling terms.

- After this process, we have a decimation of 2^x sites, where hopping parameters are getting smaller after each step. This procedure will stop after a criteria for the magnitude of α_x and β_x is fulfilled. This implies that α_x and $\beta_x \sim 0$, thus $\epsilon_x \approx \epsilon_{x-1}$ and $\epsilon_x^S \approx \epsilon_{x-1}^S$, such that

$$(\omega - \epsilon_x^S + i\eta) G_{11} \approx 1$$

or

$$G_{11} \approx \frac{1}{(\omega - \epsilon_x^S + i\eta)}. \tag{12.9}$$

This is the final result for the surface GF that we need. This procedure can be readily implemented in numerical form as it has been done in our calculation of thermoelectric phenomena or in [58, 146].

Chapter 13

Part III appendices

13.1 Appendix: Chern number and Berry phase

A brief description of \mathbb{Z} topological invariant is given only for referential use with respect to the WCC calculation of the Chern number.

In a general quantum system with adiabatic evolution we can define the Berry phase as the integral [96]

$$\gamma = \oint_C d\mathbf{R} \cdot \mathbf{A}_n(\mathbf{R}), \quad (13.1.1)$$

where \mathbf{R} represents coordinates in some parameter space and

$$\mathbf{A}_n = i \langle u_n(\mathbf{R}) | \nabla_{\mathbf{R}} | u_n(\mathbf{R}) \rangle$$

is known as the Berry connection [102]. Using Stokes theorem the previous integral could be expressed as a surface integral

$$\gamma = \oint_C d\mathbf{S} \cdot \boldsymbol{\Omega}^n(\mathbf{R}), \quad (13.1.2)$$

here $\boldsymbol{\Omega}(\mathbf{R})$ is called the Berry connection. Taking momentum space as the parameter space, the Berry curvature can be expressed by [60]

$$\boldsymbol{\Omega}^n(\mathbf{k}) = \nabla_{\mathbf{k}} \times \mathbf{A}_n(\mathbf{k}) = \nabla_{\mathbf{k}} \times \langle u_n(\mathbf{k}) | i \nabla_{\mathbf{k}} | u_n(\mathbf{k}) \rangle. \quad (13.1.3)$$

This curvature arises as an additional term in the velocity of carriers in momentum space such that [22]

$$V_n(\mathbf{q}) = \frac{1}{\hbar} \nabla_{\mathbf{k}} E_n(\mathbf{k}) - \frac{e}{\hbar} \mathbf{E} \times \boldsymbol{\Omega}^n(\mathbf{k}). \quad (13.1.4)$$

\mathbf{q} is a non-gauge-invariant crystal momentum related to \mathbf{k} as $\mathbf{k} = \mathbf{q} + \frac{e}{\hbar} \mathbf{A}(t)$, where $\mathbf{A}(t)$ is an external electromagnetic field with the electric field \mathbf{E} defined as $\mathbf{E} = \partial_t \mathbf{A}(t)$.

This anomalous velocity induces a density current \mathbf{j} given by [60]

$$\mathbf{j} = -e \sum \int \frac{d\mathbf{k}}{(2\pi)^2} V_n(\mathbf{k}) f(k). \quad (13.1.5)$$

$f(k)$ is the Fermi-Dirac distribution function. If all bands below Fermi level are filled, then the sum over the first term in velocity becomes zero, but second term yields a Hall current [102]

$$\sigma_H = \frac{e^2}{2\pi\hbar} \sum_n \int_{BZ} d\mathbf{k} \Omega_{kx,ky}^n. \quad (13.1.6)$$

Performing the integral over BZ, an integer ν is obtained such that [60]

$$\sigma_H = \nu \frac{e^2}{h}.$$

This integer value is related to the number of edge states available for conduction at the boundary of the system and it is known as the Chern number. As we mentioned in the main text, this Chern number is related to the winding number over the BZ or over the hybrid parameter space for the WCC evolution [138]. This allows to give a direct physical meaning to this number.

13.2 Appendix: Character tables

A summary of double groups character tables of interest for this thesis is presented here. Information was retrieved from Bilbao Crystallographic Server [28, 125].

Table 13.2.1 Γ -point little group character table.

| | I | C_2^z | S_4 | $(C_2^{x/y} \frac{1}{2} \frac{1}{2} 0)$ | $(m_{x-y} \frac{1}{2} \frac{1}{2} 0)$ | \bar{I} | \bar{S}_4 |
|------------------|-----|---------|-------------|-------------------------------------------|-----------------------------------------|-----------|-------------|
| Γ_1 | 1 | 1 | 1 | 1 | 1 | 1 | 1 |
| Γ_2 | 1 | 1 | -1 | 1 | -1 | 1 | -1 |
| Γ_3 | 1 | 1 | -1 | -1 | 1 | 1 | -1 |
| Γ_4 | 1 | 1 | 1 | -1 | -1 | 1 | 1 |
| Γ_5 | 2 | -2 | 0 | 0 | 0 | 2 | 0 |
| $\bar{\Gamma}_6$ | 2 | 0 | $-\sqrt{2}$ | 0 | 0 | -2 | $\sqrt{2}$ |
| $\bar{\Gamma}_7$ | 2 | 0 | $\sqrt{2}$ | 0 | 0 | -2 | $-\sqrt{2}$ |

Table 13.2.2 X -point little group character table.

| | I | C_2^z | $(C_2^y \frac{1}{2}\frac{1}{2}0)$ | $(C_2^x \frac{1}{2}\frac{1}{2}0)$ | \bar{I} | \bar{C}_2^z | $(\bar{C}_2^y \frac{1}{2}\frac{1}{2}0)$ | $(\bar{C}_2^x \frac{1}{2}\frac{1}{2}0)$ |
|-------|-----|---------|-----------------------------------|-----------------------------------|-----------|---------------|-----------------------------------------|-----------------------------------------|
| X_1 | 2 | 0 | 0 | 0 | 2 | 0 | 0 | 0 |
| X_2 | 1 | -i | 1 | -i | -1 | i | -1 | i |
| X_3 | 1 | i | -1 | -i | -1 | -i | 1 | i |
| X_4 | 1 | -i | -1 | i | -1 | i | 1 | -i |
| X_5 | 1 | i | 1 | i | -1 | -i | -1 | -i |

Table 13.2.3 M -point little group character table.

| | I | C_2^z | S_4^+ | S_4^- | $(C_2^y \frac{1}{2}\frac{1}{2}0)$ | $(C_2^x \frac{1}{2}\frac{1}{2}0)$ | $(m_{x-y} \frac{1}{2}\frac{1}{2}0)$ | $(m_{x-\bar{y}} \frac{1}{2}\frac{1}{2}0)$ |
|-------------|-----|---------|--------------|--------------|-----------------------------------|-----------------------------------|-------------------------------------|-------------------------------------------|
| M_1 | 1 | -1 | i | -i | i | -i | 1 | -1 |
| M_2 | 1 | -1 | -i | i | i | -i | -1 | 1 |
| M_3 | 1 | -1 | -i | i | -i | i | 1 | -1 |
| M_4 | 1 | -1 | i | -i | -i | i | -1 | 1 |
| M_5 | 2 | 2 | 0 | 0 | 0 | 0 | 0 | 0 |
| \bar{M}_6 | 2 | 0 | $\sqrt{2}i$ | $-\sqrt{2}i$ | 0 | 0 | 0 | 0 |
| \bar{M}_7 | 2 | 0 | $-\sqrt{2}i$ | $\sqrt{2}i$ | 0 | 0 | 0 | 0 |

continuation

| | \bar{I} | \bar{C}_2^z | \bar{S}_4^+ | \bar{S}_4^- | $(\bar{C}_2^y \frac{1}{2}\frac{1}{2}0)$ | $(\bar{C}_2^x \frac{1}{2}\frac{1}{2}0)$ | $(\bar{m}_{x-y} \frac{1}{2}\frac{1}{2}0)$ | $(\bar{m}_{x-\bar{y}} \frac{1}{2}\frac{1}{2}0)$ |
|-------------|-----------|---------------|---------------|---------------|-----------------------------------------|-----------------------------------------|-------------------------------------------|-------------------------------------------------|
| M_1 | 1 | -1 | i | -i | -i | i | 1 | -1 |
| M_2 | 1 | -1 | -i | i | -i | i | -1 | 1 |
| M_3 | 1 | -1 | -i | i | i | -i | 1 | -1 |
| M_4 | 1 | -1 | i | -i | i | -i | -1 | 1 |
| M_5 | 2 | 2 | 0 | 0 | 0 | 0 | 0 | 0 |
| \bar{M}_6 | -2 | 0 | $-\sqrt{2}i$ | $\sqrt{2}i$ | 0 | 0 | 0 | 0 |
| \bar{M}_7 | -2 | 0 | $\sqrt{2}i$ | $-\sqrt{2}i$ | 0 | 0 | 0 | 0 |

Table 13.2.4 Y -line little group character table.

| | I | C_2^z | \bar{I} | $(C_2^x \frac{1}{2}\frac{1}{2}0)$ |
|-------------|-----|----------------------------|-----------|-----------------------------------|
| Y_1 | 1 | $e^{i\pi u}$ | 1 | $e^{i\pi u}$ |
| Y_2 | 1 | $e^{i\pi(1+u)}$ | 1 | $e^{i\pi(1+u)}$ |
| \bar{Y}_3 | 1 | $e^{-i\pi(\frac{1}{2}-u)}$ | -1 | $e^{i\pi(\frac{1}{2}+u)}$ |
| \bar{Y}_4 | 1 | $e^{i\pi(\frac{1}{2}+u)}$ | -1 | $e^{-i\pi(\frac{1}{2}-u)}$ |

Where $\mathbf{k}_Y = (\frac{1}{2}, u, 0)$ with $u \in (0, \frac{1}{2})$. The definition of each label and its associated symmetry operation is presented in the main text.

13.3 Appendix: Wannier90 input

We present an input file example for wannier90 code [153], in order to make more explicit the form of our calculations for the low energy model in the topological non-trivial case.

In particular

- A Quantum Espresso output from a non self-consistent calculation with SOC included is needed [39].
- The Wannier90 script is executed in pre-processing mode with `wannier.x -pp file_name`. (see below for the complete input).
- The `pw2wannier` utility is used with the following input file

```
&inputpp
outdir = './'
prefix = 'file_name'
seedname = 'file_name'
write_mmn = .true.
write_amn = .true.
write_spn = .true.
write_unk = .false.
/
```

- Once the `pw2wannier` routine is completed, files with extension `.mmn`, `.chk`, `.eig` and `.amn` are created. These are necessary for wannier90 proper working.
- Set Wannier90 execution with `wannier.x file_name`, using the following example input file [153]

```
— num_bands = 56 ! number of WF to be found
— num_wann = 56 ! total number of bands passed to the code in the name.mmn
  file.
— !!! specify lattice vectors
— begin unit_cell_cart
— 4.637613 0.000000 0.000000
— 0.000000 4.637614 0.000000
— 0.000000 0.000000 30.000000
— end unit_cell_cart
— !!! ionic positions within unit cell in fractional coordinates
— begin atoms_cart
— Mn 0.00000742 -0.00000820 0.00000349
— Mn 0.49999178 0.50000742 0.00000349
— C 0.40294873 0.09713598 0.03648161
— C 0.90293460 0.40293458 -0.03647881
```

```
— C 0.59713596 0.90294870 0.03648161
— C 0.09712323 0.59712324 -0.03647557
— end atoms_cart
— ! Monkhorst-Pack grid k point mesh
— mp_grid : 7 7 1
— ! k points explicit list in fractional coordinates
— begin kpoints
— 0.00000000 0.00000000 0.00000000 2.040816e-02
— 0.00000000 0.14285714 0.00000000 2.040816e-02
— 0.00000000 0.28571429 0.00000000 2.040816e-02
— 0.00000000 0.42857143 0.00000000 2.040816e-02
— 0.00000000 0.57142857 0.00000000 2.040816e-02
— 0.00000000 0.71428571 0.00000000 2.040816e-02
— 0.00000000 0.85714286 0.00000000 2.040816e-02
— 0.14285714 0.00000000 0.00000000 2.040816e-02
— 0.14285714 0.14285714 0.00000000 2.040816e-02
— 0.14285714 0.28571429 0.00000000 2.040816e-02
— 0.14285714 0.42857143 0.00000000 2.040816e-02
— 0.14285714 0.57142857 0.00000000 2.040816e-02
— 0.14285714 0.71428571 0.00000000 2.040816e-02
— 0.14285714 0.85714286 0.00000000 2.040816e-02
— 0.28571429 0.00000000 0.00000000 2.040816e-02
— 0.28571429 0.14285714 0.00000000 2.040816e-02
— 0.28571429 0.28571429 0.00000000 2.040816e-02
— 0.28571429 0.42857143 0.00000000 2.040816e-02
— 0.28571429 0.57142857 0.00000000 2.040816e-02
— 0.28571429 0.71428571 0.00000000 2.040816e-02
— 0.28571429 0.85714286 0.00000000 2.040816e-02
— 0.42857143 0.00000000 0.00000000 2.040816e-02
— 0.42857143 0.14285714 0.00000000 2.040816e-02
— 0.42857143 0.28571429 0.00000000 2.040816e-02
— 0.42857143 0.42857143 0.00000000 2.040816e-02
— 0.42857143 0.57142857 0.00000000 2.040816e-02
— 0.42857143 0.71428571 0.00000000 2.040816e-02
— 0.42857143 0.85714286 0.00000000 2.040816e-02
— 0.57142857 0.00000000 0.00000000 2.040816e-02
— 0.57142857 0.14285714 0.00000000 2.040816e-02
— 0.57142857 0.28571429 0.00000000 2.040816e-02
— 0.57142857 0.42857143 0.00000000 2.040816e-02
— 0.57142857 0.57142857 0.00000000 2.040816e-02
— 0.57142857 0.71428571 0.00000000 2.040816e-02
— 0.57142857 0.85714286 0.00000000 2.040816e-02
```

```

- 0.71428571 0.00000000 0.00000000 2.040816e-02
- 0.71428571 0.14285714 0.00000000 2.040816e-02
- 0.71428571 0.28571429 0.00000000 2.040816e-02
- 0.71428571 0.42857143 0.00000000 2.040816e-02
- 0.71428571 0.57142857 0.00000000 2.040816e-02
- 0.71428571 0.71428571 0.00000000 2.040816e-02
- 0.71428571 0.85714286 0.00000000 2.040816e-02
- 0.85714286 0.00000000 0.00000000 2.040816e-02
- 0.85714286 0.14285714 0.00000000 2.040816e-02
- 0.85714286 0.28571429 0.00000000 2.040816e-02
- 0.85714286 0.42857143 0.00000000 2.040816e-02
- 0.85714286 0.57142857 0.00000000 2.040816e-02
- 0.85714286 0.71428571 0.00000000 2.040816e-02
- 0.85714286 0.85714286 0.00000000 2.040816e-02
- end kpoints
- spinors = T ! if set true WF correspond to singularly occupied spinor states.
- ! projection block define a set of localized functions used to generate
! an initial guess for the unitary transformations. used to generate
nnkp file.
- begin projections
- Mn : l=2;l=0 C : sp3
- end projections
- !guiding centres = F ! in set true projections centres are used as the
guiding centres in Wsation
- iprint = 2 ! verbosity level
- optimisation = 3
- exclude_bands : 1,2,3,4 ! a kpoint independent list of states to eclude
from calc.
- restart : default !!!default wannierize plot transport.
- !spin : up
- translate_home_cell : F
- write_xyz : T
- !disentanglement, for degenerate bands activated if num_wann < num_bands
- ! window energy specification.
- fermi_energy = -4.1378
- dis_froz_min = -8.
- dis_froz_max = 0.
- !dis_win_min =
- !dis_win_max =
- dis_num_iter = 900 ! iterations to extract the most connected subspace.
- dis_mix_ratio = 0.5 ! 0 to 1. mixing par for convengence
- dis_conv_window = 2
- dis_conv_tol = 1.0e-7

```

```

- !!!! wannierisation control
- num_iter = 300
- !!! Post processing
- wannier_plot = F
- !wannier_plot_supercell = 2 2 1
- bands_plot = F
- begin kpoint_path
- G 0.00000 0.00000 0.00000 X 0.50000 0.00000 0.00000 X 0.50000 0.00000 0.00000
  M 0.50000 0.50000 0.00000 M 0.50000 0.50000 0.00000 G 0.00000 0.00000 0.00000
- end kpoint_path
- bands_num_points = 200
- bands_plot_format = gnuplot xmgrace
- !bands_plot_project ! list of WF to project over entire k point path.
- dist_cutoff_mode : two_dim !! dimension for the distance calculation
- one_dim_axis : z
- dist_cutoff = 500.0
- hr_cutoff = 0.0
- bands_plot_mode : s-k !! or cut
- bands_plot_dim = 2
- write_hr = T

```

- This process yields a 'file_name_hr.dat' which contains the tight-binding Hamiltonian in the WF basis. This is the input needed for the WannierTools code.

13.4 Appendix: WannierTools input

This post processing tool allows for WCC calculation and slab band structure computation for a given WF tight-binding Hamiltonian.

- Necessary files for execution are a 'file_name_hr.dat' file coming from a wannier90 calculation and an inner input file name as 'wt.in'.
- An example file is given below [139]

```

- &TB_FILE Hrfile = 'file_name_hr.dat'
- Package = 'QE' ! obtained from VASP, it could be 'VASP', 'QE', 'Wien2k',
  'OpenMx' /
- &CONTROL
- BulkBand_calc = F
- DOS_calc = F
- BulkFS_calc = F
- BulkGap_cube_calc = F
- BulkGap_plane_calc = F
- SlabBand_calc = F

```

```

- SlabBand_plane_calc = F
- WireBand_calc = F
- SlabSS_calc = F
- SlabArc_calc = F
- SlabQPI_calc = F
- ArcQPI_calc = F
- Z2_3D_calc = F
- SlabSpintexture_calc = F
- Wanniercenter_calc = T
- /
- &SYSTEM NSLAB = 11 ! for thin film system NSLAB1= 11 ! nanowire system
  NSLAB2= 11 ! nanowire system NumOccupied = 41 ! NumOccupied SOC = 1 !
  soc E_FERMI = -4.1378 ! e-fermi surf_onsite= 0.0 ! surf_onsite
- /
- &PARAMETERS
- Eta_Arc = 0.001 ! infinite small value, like brodening
- E_arc = 0.0 ! energy for calculate Fermi Arc
- OmegaNum = 501 ! omega number
- OmegaMin = -2.0 ! energy interval
- OmegaMax = 2.0 ! energy interval
- Nk1 = 1101 ! number k points odd number would be better
- Nk2 = 1101 ! number k points odd number would be better
- Nk3 = 1101 ! number k points odd number would be better
- NP = 2 ! number of principle layers
- Gap_threshold = 0.001 ! threshold for GapCube output
- /
- LATTICE Angstrom
- 4.637613 0.000000 0.000000
- 0.000000 4.637614 0.000000
- 0.000000 0.000000 30.000000
- ATOM_POSITIONS 6 ! number of atoms for projectors Direct ! Direct or
  Cartisen coordinate
- Mn 0.00000742 -0.00000820 0.00000349
- Mn 0.49999178 0.50000742 0.00000349
- C 0.40294873 0.09713598 0.03648161
- C 0.90293460 0.40293458 -0.03647881
- C 0.59713596 0.90294870 0.03648161
- C 0.09712323 0.59712324 -0.03647557
- PROJECTORS
- 6 6 4 4 4 4 ! number of projectors
- Mn s dz2 dxz dyz dx2-y2 dxy
- Mn s dz2 dxz dyz dx2-y2 dxy

```

```

- C s px py pz
- !MILLER_INDEX
- !1 0 0
- SURFACE ! Specify surface with two vectors, see doc
- 1 0 0
- 0 1 0
- KPATH_BULK ! k point path 3 ! number of k line only for bulk band
- G 0.00000 0.00000 0.0000 X 0.50000 0.00000 0.0000
- X 0.50000 0.00000 0.0000 M 0.50000 0.50000 0.0000
- M 0.50000 0.50000 0.0000 G 0.00000 0.00000 0.0000
- KPATH_SLAB 2 ! number of k line for 2D case X 0.5 0.0 G 0.0 0.0 ! k path
for 2D case G 0.0 0.0 X 0.5 0.0
- !KPLANE_SLAB ! -0.5 -0.5 ! Original point for 2D k plane ! 1.0 0.0 !
The first vector to define 2D k plane ! 0.0 1.0 ! The second vector to
define 2D k plane for arc plots
- KPLANE_BULK 0.50 0.50 0.00 ! Original point for 3D k plane 1.00 0.00 0.00
! The first vector to define 3d k space plane 0.00 1.00 0.00 ! The second
vector to define 3d k space plane
- !KCUBE_BULK ! -0.50 -0.50 -0.50 ! Original point for 3D k plane ! 1.00
0.00 0.00 ! The first vector to define 3d k space plane ! 0.00 1.00 0.00
! The second vector to define 3d k space plane ! 0.00 0.00 1.00 ! The
third vector to define 3d k cube
- !EFFECTIVE_MASS ! optional !2 ! The i'th band to be calculated !0.01 !
k step in unit of (1/Angstrom) !0.0 0.0 0.0 ! k point where the effective
mass calculated.
- !KPOINTS_3D !4 !Direct !0.0 0.0 0.0 !0.5 0.0 0.0 !0.0 0.5 0.0 !0.0 0.0
0.5
- WANNIER_CENTRES ! copy from wannier90.wout
- Cartesian
- -2.20244006 -0.74606813 0.93510877
- -1.89917788 -1.19367513 0.83214786
- -0.01007151 0.00590747 -0.18383644
- -0.10438923 0.11069266 -0.12455080
- -0.22970125 0.00030128 0.08490797
- -0.15360900 -0.07944181 -0.13224412
- 0.01653210 0.03332069 -0.02826385
- 0.11817837 -0.12915681 -0.04930888
- -0.23264818 -0.05533031 -0.02375009
- -0.05378903 -0.19021198 0.01703492
- -0.23400293 -0.08558875 0.02222299
- -0.21338938 -0.11514902 -0.00802827
- -2.44520618 -2.36085497 -0.12876787

```

— -2.11163293 2.36214403 -0.05429857
— 1.13623570 2.78560475 -0.88268161
— 2.12468318 2.16906574 0.06283309
— 2.32805116 0.01295728 1.40766577
— 2.32383756 -0.00131362 1.40562188
— -2.05062117 2.27565926 -0.07368166
— 0.01890337 2.30125457 -1.40888808
— 0.00744030 2.31251526 -1.40609401
— 1.19360653 2.73292283 -0.83164226
— 2.34586230 2.45280444 0.16237229
— 2.39757721 2.35032505 0.13715923
— 0.21962959 0.10026286 0.00141010
— 0.46103121 -1.18019626 -0.87125670
— 0.27179374 0.03075933 -0.03678634
— 1.46439479 0.21304703 0.96309872
— 1.12049353 0.41787310 0.83206734
— 0.18477240 0.21786328 0.04327955
— 0.19801942 -0.00335002 0.15859945
— 0.25128715 -0.03461766 0.11086838
— 2.34670282 0.02711980 0.81168817
— 2.32533861 0.00152416 0.81338028
— 2.23674124 -2.08903127 -0.05174178
— 2.21383307 -2.09373332 -0.00853566
— 1.85915898 1.13662427 0.86549859
— 2.16742467 -2.34387590 -0.18294907
— 2.40055478 2.06663984 -0.05124350
— 2.36242612 2.06300797 -0.08075780
— 2.32417652 2.32212655 0.07665142
— 2.10153923 0.88702998 0.95902455
— 2.25714465 2.55117812 0.18651991
— 2.20168265 2.49796156 0.16359927
— 0.02743480 2.27872744 -0.81078112
— 0.03480859 2.26221151 -0.81005554
— 2.20326035 2.16891091 -0.11862825
— -2.05974648 2.26309794 -0.03567981
— 0.41152395 -1.12079418 -0.81486746
— 0.09404740 0.20672006 0.14251217
— -0.74522264 2.20787075 -0.92692756
— -0.68784386 2.27437024 -0.91959336
— -0.35469207 1.37668860 -0.99418732
— -0.46547086 1.37838428 -1.00541512
— -1.37685658 -0.35008925 0.98235016

— -1.17914029 -0.45405965 0.86672379

- This input can be use to calculate all quantities of interest depending on which one we put in *true mode*. More information about the particular use for each mode is given in the doc section in the distribution's folder [139].

Bibliography

- [1] Ching-Kai Chiu, Jeffrey C.Y. Teo, Andreas P. Schnyder, and Shinsei Ryu. Classification of topological quantum matter with symmetries. *Reviews of Modern Physics*, 88(3):035005, aug 2016.
- [2] John Isaac G. Enriquez and Al Rey C. Villagracia. Hydrogen adsorption on pristine, defected, and 3d-block transition metal-doped penta-graphene. *International Journal of Hydrogen Energy*, 41(28):12157 – 12166, 2016.
- [3] Golibjon R. Berdiyrov and Mohamed El-Amine Madjet. First-principles study of electronic transport and optical properties of penta-graphene, penta-SiC₂ and penta-CN₂. *RSC Adv.*, 6:50867–50873, 2016.
- [4] Shunhong Zhang, Jian Zhou, Qian Wang, Xiaoshuang Chen, Yoshiyuki Kawazoe, and Puru Jena. Penta-graphene: A new carbon allotrope. *Proc. Natl. Acad. Sci. USA*, 112(8):2372–2377, 2015.
- [5] Christopher P. Ewels, Xavier Rocquefelte, Harold W. Kroto, Mark J. Rayson, Patrick R. Briddon, and Malcolm I. Heggie. Predicting experimentally stable allotropes: Instability of penta-graphene. *Proc. Natl. Acad. Sci. USA*, 112(51):15609–15612, 2015.
- [6] Paul Avramov, Victor Demin, Ming Luo, Cheol Ho Choi, Pavel B. Sorokin, Boris Yakobson, and Leonid Chernozatonskii. Translation symmetry breakdown in low-dimensional lattices of pentagonal rings. *The Journal of Physical Chemistry Letters*, 6(22):4525–4531, 2015.
- [7] Qing Hua Wang, Kouros Kalantar-Zadeh, Andras Kis, Jonathan N. Coleman, and Michael S. Strano. Electronics and optoelectronics of two-dimensional transition metal dichalcogenides. *Nature Nanotechnology*, 7(11):699–712, nov 2012.
- [8] Wen Xu, Gang Zhang, and Baowen Li. Thermal conductivity of penta-graphene from molecular dynamics study. *The Journal of Chemical Physics*, 143(15):154703, 2015.
- [9] Huake Liu, Guangzhao Qin, Yuan Lin, and Ming Hu. Disparate strain dependent thermal conductivity of two-dimensional penta-structures. *Nano Letters*, 16(6):3831–3842, 2016.

- [10] Fancy Qian Wang, Jiabing Yu, Qian Wang, Yoshiyuki Kawazoe, and Puru Jena. Lattice thermal conductivity of penta-graphene. *Carbon*, 105:424 – 429, 2016.
- [11] Hao Sun, Sankha Mukherjee, and Chandra Veer Singh. Mechanical properties of monolayer penta-graphene and phagraphene: a first-principles study. *Phys. Chem. Chem. Phys.*, 18:26736–26742, 2016.
- [12] Bo Xiao, Yan-chun Li, Xue-fang Yu, and Jian-bo Cheng. Penta-graphene: A Promising Anode Material as the Li/Na-Ion Battery with Both Extremely High Theoretical Capacity and Fast Charge/Discharge Rate. *ACS Applied Materials & Interfaces*, 8(51):35342–35352, 2016.
- [13] Ranganathan Krishnan, Wan-Sheng Su, and Hsin-Tsung Chen. A new carbon allotrope: Penta-graphene as a metal-free catalyst for CO oxidation. *Carbon*, 114(Supplement C):465 – 472, 2017.
- [14] Mingwei Chen, Haifei Zhan, Yinbo Zhu, Hengan Wu, and Yuantong Gu. Mechanical properties of penta-graphene nanotubes. *The Journal of Physical Chemistry C*, 121(17):9642–9647, 2017.
- [15] Zhi Gen Yu and Yong-Wei Zhang. A comparative density functional study on electrical properties of layered penta-graphene. *Journal of Applied Physics*, 118(16):165706, 2015.
- [16] T. Stauber, J. I. Beltrán, and J. Schliemann. Tight-binding approach to penta-graphene. *Scientific Reports*, 6:22672, 2016.
- [17] Golibjon Berdiyrov, Gopal Dixit, and Mohamed Madjet. Band gap engineering in penta-graphene by substitutional doping: First-principles calculations. *J. Phys. Condens. Matter*, 28:475001, 09 2016.
- [18] Yierpan Aierken, Ortwin Leenaerts, and François M. Peeters. A first-principles study of stable few-layer penta-silicene. *Physical Chemistry Chemical Physics*, 18(27):18486–18492, jul 2016.
- [19] Jun Zhao and Hui Zeng. Chemical Functionalization of Pentagermanene Leads to Stabilization and Tunable Electronic Properties by External Tensile Strain. *ACS Omega*, 2(1):171–180, jan 2017.
- [20] Joe Rosen. *Symmetry in science: an introduction to the general theory*. Springer-Verlag, New York, 1995.
- [21] Giora Hon and Bernard R. Goldstein. From proportion to balance: the background to symmetry in science. *Studies in History and Philosophy of Science Part A*, 36(1):1–21, mar 2005.
- [22] N.W.Ashcroft and N.D.Mermin. In *Solid State Physics*. Saunders College Publishing, New York, 1976.

- [23] Hermann Weyl. *The theory of groups and quantum mechanics*. Dover Publications, New York, 1950.
- [24] K. A. (Konstantin A.) Kikoin, Mikhail. Kiselev, and Yshai. Avishai. *Dynamical symmetries for nanostructures: implicit symmetries in single-electron transport through real and artificial molecules*. Springer Vienna, 2012.
- [25] S. C. Miller and W. H. Love. *Tables of Irreducible Representations of Space Groups and Co-Representations of Magnetic Space Groups*. Pruett Press, Denver, 1967.
- [26] William Fulton and Joe Harris. *Representation theory: a first course*. Springer-Verlag, New York, 1991.
- [27] Mildred S. Dresselhaus, Gene Dresselhaus, and Ado Jorio. *Group Theory - Applications to the Physics of Condensed Matter*. Springer, Berlin, 2008.
- [28] <http://www.cryst.ehu.es/>. (Bilbao Crystallographic Server, University of the Basque Country, Bilbao, Basque Country, Spain).
- [29] G. E. Volovik. Quantum Phase Transitions from Topology in Momentum Space. In *Quantum Analogues: From Phase Transitions to Black Holes and Cosmology*, pages 31–73. Springer Berlin Heidelberg, Berlin, Heidelberg, 2007.
- [30] Giuseppe Grosso and Giuseppe Pastori Parravicini. *Solid state physics*. Academic Press, Oxford, 2000.
- [31] David S. Sholl and Janice A. Steckel. *Density Functional Theory*. John Wiley & Sons, Inc., Hoboken, NJ, USA, mar 2009.
- [32] G.D.Mahan. *Many-Particle Physics.- 3rd ed*. Kluwer Academic, New York, 2000.
- [33] P. Hohenberg and W. Kohn. Inhomogeneous Electron Gas. *Physical Review*, 136(3B):B864–B871, nov 1964.
- [34] W. Kohn and L. J. Sham. Self-Consistent Equations Including Exchange and Correlation Effects. *Physical Review*, 140(4A):A1133–A1138, nov 1965.
- [35] Richard M. Martin. *Electronic Structure*. Cambridge University Press, Cambridge, 2004.
- [36] Robert G. Parr and Weitao. Yang. *Density-functional theory of atoms and molecules*. Oxford University Press, New York, 1989.
- [37] Jorge Kohanoff. *Electronic Structure Calculations for Solids and Molecules*. Cambridge University Press, Cambridge, 2006.

- [38] José M. Soler, Emilio Artacho, Julian D Gale, Alberto García, Javier Junquera, Pablo Ordejón, and Daniel Sánchez-Portal. The siesta method for ab initio order-n materials simulation. *Journal of Physics: Condensed Matter*, 14(11):2745, 2002.
- [39] Paolo Giannozzi, Stefano Baroni, Nicola Bonini, Matteo Calandra, Roberto Car, Carlo Cavazzoni, Davide Ceresoli, Guido L Chiarotti, Matteo Cococcioni, Ismaila Dabo, Andrea Dal Corso, Stefano de Gironcoli, Stefano Fabris, Guido Fratesi, Ralph Gebauer, Uwe Gerstmann, Christos Gougoussis, Anton Kokalj, Michele Lazzeri, Layla Martin-Samos, Nicola Marzari, Francesco Mauri, Riccardo Mazzarello, Stefano Paolini, Alfredo Pasquarello, Lorenzo Paulatto, Carlo Sbraccia, Sandro Scandolo, Gabriele Sclauzero, Ari P Seitsonen, Alexander Smogunov, Paolo Umari, and Renata M Wentzcovitch. QUANTUM ESPRESSO: a modular and open-source software project for quantum simulations of materials. *Journal of Physics: Condensed Matter*, 21(39):395502, sep 2009.
- [40] Efthimios Kaxiras. *Atomic and Electronic Structure of Solids*. Cambridge University Press, Cambridge, 2003.
- [41] J. C. Slater and G. F. Koster. Simplified LCAO Method for the Periodic Potential Problem. *Physical Review*, 94(6):1498–1524, jun 1954.
- [42] L. C. Lew Yan Voon and L. R. Ram-Mohan. Tight-binding representation of the optical matrix elements: Theory and applications. *Phys. Rev. B*, 47:15500–15508, Jun 1993.
- [43] Noriaki Horiuchi. Fabric optoelectronics. *Nature Photonics*, 12(10):573–573, oct 2018.
- [44] G. F. (Giuseppe Franco) Bassani and Giuseppe Pastori Parravicini. *Electronic states and optical transitions in solids*,. Pergamon Press, Oxford, 1975.
- [45] Mark (Anthony Mark) Fox. *Optical properties of solids*. Oxford University Press, 2001.
- [46] Abbas Zarifi and Thomas Garm Pedersen. Universal analytic expression of electric-dipole matrix elements for carbon nanotubes. *Phys. Rev. B*, 80:195422, Nov 2009.
- [47] M. Graf and P. Vogl. Electromagnetic fields and dielectric response in empirical tight-binding theory. *Phys. Rev. B*, 51:4940–4949, Feb 1995.
- [48] Massimiliano Di Ventra. *Electrical Transport in Nanoscale Systems*. Cambridge University Press, Cambridge, 2008.
- [49] Supriyo Datta. *Electronic Transport in Mesoscopic Systems*. Cambridge University Press, Cambridge, 1995.

- [50] Yuli V. Nazarov and Yaroslav M. Blanter. *Quantum Transport*. Cambridge University Press, Cambridge, 2009.
- [51] David K. Ferry. *Semiconductor transport*. Taylor & Francis, Boston, 2000.
- [52] Supriyo Datta. *Quantum Transport: Atom to Transistor*. Cambridge University Press, Cambridge, 2005.
- [53] Dmitry Ryndyk. *Theory of Quantum Transport at Nanoscale*, volume 184 of *Springer Series in Solid-State Sciences*. Springer International Publishing, Cham, 2016.
- [54] M P Lopez Sancho, J M Lopez Sancho, and J Rubio. Quick iterative scheme for the calculation of transfer matrices: application to Mo (100). *Journal of Physics F: Metal Physics*, 14(5):1205–1215, may 1984.
- [55] M P Lopez Sancho, J M Lopez Sancho, J M L Sancho, and J Rubio. Highly convergent schemes for the calculation of bulk and surface Green functions. *Journal of Physics F: Metal Physics*, 15(4):851–858, apr 1985.
- [56] Raseong Kim, Supriyo Datta, and Mark S. Lundstrom. Influence of dimensionality on thermoelectric device performance. *Journal of Applied Physics*, 105(3):034506, 2009.
- [57] Xiaodong Wang and Zhiming M. Wang, editors. *Nanoscale Thermoelectrics*, volume 16 of *Lecture Notes in Nanoscale Science and Technology*. Springer International Publishing, Cham, 2014.
- [58] Leonor Chico, P.A. Orellana, L. Rosales, and M. Pacheco. Spin and Charge Caloritronics in Bilayer Graphene Flakes with Magnetic Contacts. *Physical Review Applied*, 8(5):054029, nov 2017.
- [59] M.S. Dresselhaus, G. Chen, M.Y. Tang, R.G. Yang, H. Lee, D.Z. Wang, Z.F. Ren, J.P. Fleurial, and P. Gogna. New Directions for Low-Dimensional Thermoelectric Materials. *Advanced Materials*, 19(8):1043–1053, apr 2007.
- [60] D. J. Thouless, M. Kohmoto, M. P. Nightingale, and M. den Nijs. Quantized Hall Conductance in a Two-Dimensional Periodic Potential. *Physical Review Letters*, 49(6):405–408, aug 1982.
- [61] J. K. Jain. Composite-fermion approach for the fractional quantum Hall effect. *Physical Review Letters*, 63(2):199–202, jul 1989.
- [62] Richard E. Prange and Steven M. Girvin. *The Quantum Hall Effect*. Springer New York, 1990.
- [63] Yasuhiro Hatsugai. Chern number and edge states in the integer quantum Hall effect. *Physical Review Letters*, 71(22):3697–3700, nov 1993.

- [64] C. L. Kane and E. J. Mele. Z₂ Topological Order and the Quantum Spin Hall Effect. *Physical Review Letters*, 95(14):146802, sep 2005.
- [65] C. L. Kane and E. J. Mele. Quantum Spin Hall Effect in Graphene. *Physical Review Letters*, 95(22):226801, nov 2005.
- [66] Klaus von Klitzing. The quantized Hall effect. *Reviews of Modern Physics*, 58(3):519–531, jul 1986.
- [67] R. B. Laughlin. Anomalous Quantum Hall Effect: An Incompressible Quantum Fluid with Fractionally Charged Excitations. *Physical Review Letters*, 50(18):1395–1398, may 1983.
- [68] F. D. M. Haldane. Model for a Quantum Hall Effect without Landau Levels: Condensed-Matter Realization of the "Parity Anomaly". *Physical Review Letters*, 61(18):2015–2018, oct 1988.
- [69] Jairo Sinova, Dimitrie Culcer, Q. Niu, N. A. Sinitsyn, T. Jungwirth, and A. H. MacDonald. Universal Intrinsic Spin Hall Effect. *Physical Review Letters*, 92(12):126603, mar 2004.
- [70] M. Z. Hasan and C. L. Kane. Colloquium: Topological insulators. *Reviews of Modern Physics*, 82(4):3045–3067, nov 2010.
- [71] B Andrei Bernevig, Taylor L Hughes, and Shou-Cheng Zhang. Quantum spin Hall effect and topological phase transition in HgTe quantum wells. *Science (New York, N.Y.)*, 314(5806):1757–61, dec 2006.
- [72] Liang Fu, C. L. Kane, and E. J. Mele. Topological Insulators in Three Dimensions. *Physical Review Letters*, 98(10):106803, mar 2007.
- [73] Markus König, Steffen Wiedmann, Christoph Brüne, Andreas Roth, Hartmut Buhmann, Laurens W Molenkamp, Xiao-Liang Qi, and Shou-Cheng Zhang. Quantum spin hall insulator state in HgTe quantum wells. *Science (New York, N.Y.)*, 318(5851):766–70, nov 2007.
- [74] Haijun Zhang, Chao-Xing Liu, Xiao-Liang Qi, Xi Dai, Zhong Fang, and Shou-Cheng Zhang. Topological insulators in Bi₂Se₃, Bi₂Te₃ and Sb₂Te₃ with a single Dirac cone on the surface. *Nature Physics*, 5(6):438–442, jun 2009.
- [75] Y L Chen, J G Analytis, J-H Chu, Z K Liu, S-K Mo, X L Qi, H J Zhang, D H Lu, X Dai, Z Fang, S C Zhang, I R Fisher, Z Hussain, and Z-X Shen. Experimental realization of a three-dimensional topological insulator, Bi₂Te₃. *Science (New York, N.Y.)*, 325(5937):178–81, jul 2009.
- [76] Andreas P. Schnyder, Shinsei Ryu, Akira Furusaki, and Andreas W. W. Ludwig. Classification of topological insulators and superconductors in three spatial dimensions. *Physical Review B*, 78(19):195125, nov 2008.

- [77] Hari C. Manoharan. A romance with many dimensions. *Nature Nanotechnology*, 5(7):477–479, jul 2010.
- [78] M. Zahid Hasan and Joel E. Moore. Three-Dimensional Topological Insulators. *Annual Review of Condensed Matter Physics*, 2(1):55–78, mar 2011.
- [79] Joel E. Moore. The birth of topological insulators. *Nature*, 464(7286):194–198, mar 2010.
- [80] Shinsei Ryu, Andreas P Schnyder, Akira Furusaki, and Andreas W W Ludwig. Topological insulators and superconductors: tenfold way and dimensional hierarchy. *New Journal of Physics*, 12(6):065010, jun 2010.
- [81] Rui Yu, Wei Zhang, Hai-Jun Zhang, Shou-Cheng Zhang, Xi Dai, and Zhong Fang. Quantized anomalous Hall effect in magnetic topological insulators. *Science (New York, N.Y.)*, 329(5987):61–4, jul 2010.
- [82] N. Nagaosa, Y. Xia, L. Wray, D. Qian, A. Pal, J. H. Dil, J. Osterwalder, F. Meier, G. Bihlmayer, C. L. Kane, Y. S. Hor, R. J. Cava, and M. Z. Hasan. PHYSICS: A New State of Quantum Matter. *Science*, 318(5851):758–759, nov 2007.
- [83] Dmytro Pesin and Allan H. MacDonald. Spintronics and pseudospintronics in graphene and topological insulators. *Nature Materials*, 11(5):409–416, may 2012.
- [84] Shuichi Murakami. Phase transition between the quantum spin Hall and insulator phases in 3D: emergence of a topological gapless phase. *New Journal of Physics*, 9(9):356–356, sep 2007.
- [85] Xiangang Wan, Ari M. Turner, Ashvin Vishwanath, and Sergey Y. Savrasov. Topological semimetal and Fermi-arc surface states in the electronic structure of pyrochlore iridates. *Physical Review B - Condensed Matter and Materials Physics*, 83(20):205101, may 2011.
- [86] Z. K. Liu, J. Jiang, B. Zhou, Z. J. Wang, Y. Zhang, H. M. Weng, D. Prabhakaran, S. K. Mo, H. Peng, P. Dudin, T. Kim, M. Hoesch, Z. Fang, X. Dai, Z. X. Shen, D. L. Feng, Z. Hussain, and Y. L. Chen. A stable three-dimensional topological Dirac semimetal Cd₃As₂. *Nature Materials*, 13(7):677–681, jul 2014.
- [87] Z. K. Liu, B. Zhou, Y. Zhang, Z. J. Wang, H. M. Weng, D. Prabhakaran, S. K. Mo, Z. X. Shen, Z. Fang, X. Dai, Z. Hussain, and Y. L. Chen. Discovery of a three-dimensional topological Dirac semimetal, Na₃Bi. *Science*, 343(6173):864–867, feb 2014.
- [88] Su Yang Xu, Ilya Belopolski, Nasser Alidoust, Madhab Neupane, Guang Bian, Chenglong Zhang, Raman Sankar, Guoqing Chang, Zhujun Yuan, Chi Cheng Lee, Shin Ming Huang, Hao Zheng, Jie Ma, Daniel S. Sanchez,

- Bao Kai Wang, Arun Bansil, Fangcheng Chou, Pavel P. Shibayev, Hsin Lin, Shuang Jia, and M. Zahid Hasan. Discovery of a Weyl fermion semimetal and topological Fermi arcs. *Science*, 349(6248):613–617, aug 2015.
- [89] Ling Lu, Zhiyu Wang, Dexin Ye, Lixin Ran, Liang Fu, John D. Joannopoulos, and Marin Soljačić. Experimental observation of Weyl points. *Science*, 349(6248):622–624, aug 2015.
- [90] B. Q. Lv, H. M. Weng, B. B. Fu, X. P. Wang, H. Miao, J. Ma, P. Richard, X. C. Huang, L. X. Zhao, G. F. Chen, Z. Fang, X. Dai, T. Qian, and H. Ding. Experimental discovery of Weyl semimetal TaAs. *Physical Review X*, 5(3):031013, jul 2015.
- [91] Barry Bradlyn, L. Elcoro, Jennifer Cano, M. G. Vergniory, Zhijun Wang, C. Felser, M. I. Aroyo, and B. Andrei Bernevig. Topological quantum chemistry. *Nature*, 547:298–305, 2017.
- [92] Gang Xu, Hongming Weng, Zhijun Wang, Xi Dai, and Zhong Fang. Chern Semimetal and the Quantized Anomalous Hall Effect in HgCr₂Se₄. *Physical Review Letters*, 107(18):186806, oct 2011.
- [93] Xiang Hu, Zhicheng Zhong, and Gregory A. Fiete. First Principles Prediction of Topological Phases in Thin Films of Pyrochlore Iridates. *Scientific Reports*, 5(1):11072, sep 2015.
- [94] Hongming Weng, Xi Dai, and Zhong Fang. Topological semimetals predicted from first-principles calculations. *Journal of Physics: Condensed Matter*, 28(30):303001, aug 2016.
- [95] M. Yagmurcukardes, H. Sahin, J. Kang, E. Torun, F. M. Peeters, and R. T. Senger. Pentagonal monolayer crystals of carbon, boron nitride, and silver azide. *Journal of Applied Physics*, 118(10):104303, sep 2015.
- [96] B. Andrei Bernevig and Taylor L. Hughes. *Topological insulators and topological superconductors*. Princeton University Press, New Jersey, 2013.
- [97] A. H. Castro Neto, F. Guinea, N. M. R. Peres, K. S. Novoselov, and A. K. Geim. The electronic properties of graphene. *Reviews of Modern Physics*, 81(1):109–162, jan 2009.
- [98] Cheng-Cheng Liu, Wanxiang Feng, and Yugui Yao. Quantum spin Hall effect in silicene and two-dimensional germanium. *Physical Review Letters*, 107(7):076802, aug 2011.
- [99] Yang Song and Hanan Dery. Transport Theory of Monolayer Transition-Metal Dichalcogenides through Symmetry. *Physical Review Letters*, 111(2):026601, jul 2013.

- [100] M A Cazalilla, H Ochoa, and F Guinea. Quantum spin Hall effect in two-dimensional crystals of transition-metal dichalcogenides. *Physical Review Letters*, 113(7):077201, aug 2014.
- [101] M. I. Katsnelson, K. S. Novoselov, and A. K. Geim. Chiral tunnelling and the Klein paradox in graphene. *Nature Physics*, 2(9):620–625, sep 2006.
- [102] Shun-Qing Shen. *Topological Insulators*, volume 174 of *Springer Series in Solid-State Sciences*. Springer, Berlin, 2012.
- [103] A. A. Zyuzin and A. A. Burkov. Topological response in Weyl semimetals and the chiral anomaly. *Physical Review B*, 86(11):115133, sep 2012.
- [104] A. A. Zyuzin, Si Wu, and A. A. Burkov. Weyl semimetal with broken time reversal and inversion symmetries. *Physical Review B - Condensed Matter and Materials Physics*, 85(16):165110, apr 2012.
- [105] A.A. Burkov. Chiral Anomaly and Diffusive Magnetotransport in Weyl Metals. *Physical Review Letters*, 113(24):247203, dec 2014.
- [106] Leslie M. Schoop, Florian Pielnhofer, and Bettina V. Lotsch. Chemical Principles of Topological Semimetals. *Chemistry of Materials*, 30(10):3155–3176, may 2018.
- [107] Binghai Yan and Claudia Felser. Topological Materials: Weyl Semimetals. *Annual Review of Condensed Matter Physics*, 8(1):337–354, mar 2017.
- [108] A.A. Burkov. Weyl Metals. *Annual Review of Condensed Matter Physics*, 9(1):359–378, mar 2018.
- [109] A. A. Burkov, M. D. Hook, and Leon Balents. Topological nodal semimetals. *Phys. Rev. B*, 84:235126, Dec 2011.
- [110] Andreas Topp, Maia G. Vergniory, Maxim Krivenkov, Andrei Varykhalov, Fanny Rodolakis, Jessica L. McChesney, Bettina V. Lotsch, Christian R. Ast, and Leslie M. Schoop. The effect of spin-orbit coupling on nonsymmorphic square-net compounds. *Journal of Physics and Chemistry of Solids*, (1):55–61, 2017.
- [111] Sebastian Klemenz, Shiming Lei, and Leslie M. Schoop. Topological Semimetals in Square-Net Materials. arXiv1808.06619. aug 2018.
- [112] Zhongbo Yan, Ren Bi, Huitao Shen, Ling Lu, Shou-Cheng Zhang, and Zhong Wang. Nodal-link semimetals. *Physical Review B*, 96(4):041103, jul 2017.
- [113] Tomáš Bzdušek, QuanSheng Wu, Andreas Rüegg, Manfred Sigrist, and Alexey A. Soluyanov. Nodal-chain metals. *Nature*, 538(7623):75–78, aug 2016.

- [114] Ren Bi, Zhongbo Yan, Ling Lu, and Zhong Wang. Nodal-knot semimetals. *Physical Review B*, 96(20):201305, nov 2017.
- [115] Luyang Wang, Shao-Kai Jian, and Hong Yao. Hourglass semimetals with nonsymmorphic symmetries in three dimensions. *Physical Review B*, 96(7):075110, aug 2017.
- [116] Alexey A. Soluyanov and David Vanderbilt. Wannier representation of Z_2 topological insulators. *Physical Review B*, 83(3):035108, jan 2011.
- [117] M. G. Vergniory, L. Elcoro, Zhijun Wang, Jennifer Cano, C. Felser, M. I. Aroyo, B. Andrei Bernevig, and Barry Bradlyn. Graph theory data for topological quantum chemistry. *Phys. Rev. E*, 96:023310, Aug 2017.
- [118] Nicola Marzari, Arash A. Mostofi, Jonathan R. Yates, Ivo Souza, and David Vanderbilt. Maximally localized Wannier functions: Theory and applications. *Reviews of Modern Physics*, 84(4):1419–1475, oct 2012.
- [119] Jennifer Cano, Barry Bradlyn, Zhijun Wang, L. Elcoro, M. G. Vergniory, C. Felser, M. I. Aroyo, and B. Andrei Bernevig. Building blocks of topological quantum chemistry: Elementary band representations. *Phys. Rev. B*, 97:035139, Jan 2018.
- [120] J. Zak. Band representations of space groups. *Phys. Rev. B*, 26:3010–3023, Sep 1982.
- [121] H. Bacry, L. Michel, and J. Zak. Symmetry and classification of energy bands in crystals. In *Group Theoretical Methods in Physics*, pages 289–308. Springer-Verlag, Berlin/Heidelberg.
- [122] Maryam Taherinejad, Kevin F. Garrity, and David Vanderbilt. Wannier center sheets in topological insulators. *Physical Review B*, 89(11):115102, mar 2014.
- [123] N.P. Armitage, E.J. Mele, and Ashvin Vishwanath. Weyl and Dirac semimetals in three-dimensional solids. *Reviews of Modern Physics*, 90(1):015001, jan 2018.
- [124] Barry Bradlyn, L. Elcoro, M. G. Vergniory, Jennifer Cano, Zhijun Wang, C. Felser, M. I. Aroyo, and B. Andrei Bernevig. Band connectivity for topological quantum chemistry: Band structures as a graph theory problem. *Phys. Rev. B*, 97:035138, Jan 2018.
- [125] Luis Elcoro, Barry Bradlyn, Zhijun Wang, Maia G. Vergniory, Jennifer Cano, Claudia Felser, B. Andrei Bernevig, Danel Orobengoa, Gemma de la Flor, Mois I. Aroyo, and IUCr. Double crystallographic groups and their representations on the Bilbao Crystallographic Server. *Journal of Applied Crystallography*, 50(5):1457–1477, oct 2017.
- [126] Mikio Nakahara. *Geometry, topology, and physics*. CRC Press, 2017.

- [127] Edward Witten. D-branes and K-theory. *Journal of High Energy Physics*, 1998(12):019–019, dec 1998.
- [128] Alexei Kitaev, Vladimir Lebedev, and Mikhail Feigel'man. Periodic table for topological insulators and superconductors. In *AIP Conference Proceedings*, volume 1134, pages 22–30. AIP, may 2009.
- [129] Daniel S. Freed and Gregory W. Moore. Twisted Equivariant Matter. *Annales Henri Poincaré*, 14(8):1927–2023, dec 2013.
- [130] Kiyonori Gomi. Freed-Moore K-theory. arXiv:1705.09134. may 2017.
- [131] Shunji Matsuura, Po Yao Chang, Andreas P Schnyder, and Shinsei Ryu. Protected boundary states in gapless topological phases. *New Journal of Physics*, 15(6):065001, jun 2013.
- [132] Ching-Kai Chiu and Andreas P. Schnyder. Classification of reflection-symmetry-protected topological semimetals and nodal superconductors. *Physical Review B*, 90(20):205136, nov 2014.
- [133] Ching-Kai Chiu and Andreas P Schnyder. Classification of crystalline topological semimetals with an application to Na₃Bi. *Journal of Physics: Conference Series*, 603(1):012002, apr 2015.
- [134] Haruki Watanabe, Hoi Chun Po, Michael P. Zaletel, and Ashvin Vishwanath. Filling-Enforced Gaplessness in Band Structures of the 230 Space Groups. *Physical Review Letters*, 117(9):096404, aug 2016.
- [135] Ru Chen, Hoi Chun Po, Jeffrey B. Neaton, and Ashvin Vishwanath. Topological materials discovery using electron filling constraints. *Nature Physics*, 14(1):55–61, oct 2018.
- [136] Hoi Chun Po, Ashvin Vishwanath, and Haruki Watanabe. Symmetry-based indicators of band topology in the 230 space groups. *Nature Communications*, 8(1):50, dec 2017.
- [137] Alexey A. Soluyanov and David Vanderbilt. Computing topological invariants without inversion symmetry. *Physical Review B*, 83(23):235401, jun 2011.
- [138] Dominik Gresch, Gabriel Autès, Oleg V. Yazyev, Matthias Troyer, David Vanderbilt, B. Andrei Bernevig, and Alexey A. Soluyanov. Z2Pack: Numerical implementation of hybrid Wannier centers for identifying topological materials. *Physical Review B*, 95(7):075146, feb 2017.
- [139] QuanSheng Wu, ShengNan Zhang, Hai-Feng Song, Matthias Troyer, and Alexey A. Soluyanov. WannierTools: An open-source software package for novel topological materials. *Computer Physics Communications*, 224:405–416, mar 2018.

- [140] John P. Perdew, Kieron Burke, and Matthias Ernzerhof. Generalized gradient approximation made simple. *Physical Review Letters*, 77(18):3865, 1996.
- [141] Biplab Rajbanshi, Sunandan Sarkar, Bikash Mandal, and Pranab Sarkar. Energetic and electronic structure of penta-graphene nanoribbons. *Carbon*, 100(Supplement C):118 – 125, 2016.
- [142] C. He, X. F. Wang, and W. X. Zhang. Coupling effects of the electric field and bending on the electronic and magnetic properties of penta-graphene nanoribbons. *Phys. Chem. Chem. Phys.*, 19:18426–18433, 2017.
- [143] P. F. Yuan, Z. H. Zhang, Z. Q. Fan, and M. Qiu. Electronic structure and magnetic properties of penta-graphene nanoribbons. *Phys. Chem. Chem. Phys.*, 19:9528–9536, 2017.
- [144] M. Damnjanović and I. Milošević. *Line Groups in Physics*. Springer, Berlin, 2010.
- [145] Mercuri G. Kanatzidis. Nanostructured Thermoelectrics: The New Paradigm? *Chemistry of Materials*, 22(3):648–659, feb 2010.
- [146] L. Chico, L. X. Benedict, S. G. Louie, and M. L. Cohen. Quantum conductance of carbon nanotubes with defects. *Phys. Rev. B*, 54:2600, 1996.
- [147] G. Jeffrey Snyder and Eric S. Toberer. Complex thermoelectric materials. *Nature Materials*, 7(2):105–114, feb 2008.
- [148] Steve M. Young and Charles L. Kane. Dirac semimetals in two dimensions. *Phys. Rev. Lett.*, 115:126803, Sep 2015.
- [149] J. J. Quijano-Briones, H. N. Fernandez-Escamilla, and A. Tlahuice-Flores. Doped penta-graphene and hydrogenation of its related structures: a structural and electronic DFT-D study. *Phys. Chem. Chem. Phys.*, 18:15505–15509, 2016.
- [150] Shan Guan, Ying Liu, Zhi-Ming Yu, Shan-Shan Wang, Yugui Yao, and Shengyuan A. Yang. Two-dimensional Spin-Orbit Dirac Point in Monolayer HfGeTe. *Physical Review Materials*, 1(5):054003, oct 2017.
- [151] M. Mogi, R. Yoshimi, A. Tsukazaki, K. Yasuda, Y. Kozuka, K. S. Takahashi, M. Kawasaki, and Y. Tokura. Magnetic modulation doping in topological insulators toward higher-temperature quantum anomalous Hall effect. *Applied Physics Letters*, 107(18):182401, nov 2015.
- [152] Martin Schlipf and François Gygi. Optimization algorithm for the generation of ONCV pseudopotentials. *Computer Physics Communications*, 196:36–44, nov 2015.

- [153] Arash A. Mostofi, Jonathan R. Yates, Giovanni Pizzi, Young-Su Lee, Ivo Souza, David Vanderbilt, and Nicola Marzari. An updated version of wannier90: A tool for obtaining maximally-localised Wannier functions. *Computer Physics Communications*, 185(8):2309–2310, aug 2014.